

CHARACTERIZATION AND IDENTIFICATION OF CRYSTALLINE STRUCTURES IN
CANNABIS SOLVENT EXTRACTS

By

Otyllia Ruth Abraham

A THESIS

Submitted to
Michigan State University
in partial fulfillment of the requirements
for the degree of

Forensic Science – Master of Science

2021

ABSTRACT

CHARACTERIZATION AND IDENTIFICATION OF CRYSTALLINE STRUCTURES IN CANNABIS SOLVENT EXTRACTS

By

Otyllia Ruth Abraham

Cannabis solvent extracts comprise of a variety of products formed through the isolation and concentration of cannabinoids from either marijuana or hemp using organic solvents.

Marijuana and hemp represent two broad classes of *Cannabis sativa* plants and are distinguished based on the concentration of the psychoactive cannabinoid delta-9-tetrahydrocannabinol (Δ^9 -THC). A common marijuana solvent extract is butane hash oil, which uses butane to extract and concentrate Δ^9 -THC and its naturally occurring acidic form, delta-9-tetrahydrocannabinolic acid (Δ^9 -THCA). Hemp solvent extracts, however, typically isolate cannabidiol (CBD).

This work aimed to comprehensively characterize marijuana and hemp-derived solvent extracts using optical and chemical techniques. Optical analysis *via* polarized light microscopy (PLM) was performed to characterize crystalline materials present in both subsets of extracts and indicated the possibility to differentiate marijuana and hemp extracts based on optical differences. Chemical characterization through infrared spectroscopy and single crystal X-ray diffraction provided the identification of the crystalline component (THCA for marijuana extracts and CBD for hemp extracts) and supported the PLM findings. Additionally, the derivatization procedure (focusing on reaction temperature, reaction time, and solvent ratio) for THCA using a common silylation reagent was optimized using full factorial experimental design to allow for the analysis of the solvent extracts by gas chromatography-mass spectrometry.

ACKNOWLEDGEMENTS

First, I would like to thank my advisor, Dr. Ruth Smith, for her guidance, support, and encouragement to continue exploring microscopy throughout my Master's career. Without her high expectations and reassurance, I would not have grown to be the forensic scientist and microscopist I am today.

I would like to acknowledge the Michigan State Forensic Science Program for funding this work and for support to present this research. Additionally, I would like to extend a huge thank you to the Kalamazoo County Sheriff's Department – especially Sgt. Jim Dunlop – for providing case samples used throughout this work. My time at Kalamazoo was made worthwhile by the kind words from the crime lab, coffee breaks, and endless talks over donuts. Additionally, I would like to thank Dr. Richard Staples and the Center for Crystallographic Research for their assistance with single crystals XRD analysis. Further, I would like to acknowledge my research committee: Dr. Ruth Smith, Dr. Jennifer Cobbina, Dr. Richard Staples, and Sgt. Jim Dunlop for their input, help, and challenging questions that have culminated in this immense accomplishment in my life.

I would like to extend a big thank you to my forensic science colleagues, as well as Dr. Victoria McGuffin, for their critical insight throughout this work. Your questions and comments encouraged me to explore this work more deeply and I have gained a wealth of knowledge from our time together.

I would be nowhere without the unending support of my friends and family. Thank you to my wonderful friends, near and afar, for endless phone calls akin to therapy, good beer, better gin, and laughter-filled distractions from the stress of grad school. A massive, and well deserved,

thank you to Niko (and Dante, of course) – you gave me peace, kept me sane, and constantly reminded me I can accomplish anything as long as I take it one step at a time. Finally thank you to my family, especially my mother, father, and sister Marci, for their love, support, and inspiration.

All glory to God.

TABLE OF CONTENTS

LIST OF TABLES	viii
LIST OF FIGURES	x
1. INTRODUCTION	1
1.1 CANNABIS SATIVA – MARIJUANA AND HEMP	1
1.2 CANNABIS SOLVENT EXTRACTS.....	2
1.3 FORENSIC ANALYSIS OF SEIZED DRUGS	4
1.4 ADDRESSING THE IDENTIFICATION OF CANNABIS EXTRACTS	5
1.5 RESEARCH OBJECTIVES	6
REFERENCES	9
2. OPTICAL CHARACTERIZATION OF CRYSTALLINE STRUCTURES IN CANNABIS SOLVENT EXTRACTS.....	12
2.1 POLARIZED LIGHT MICROSCOPY.....	14
2.1.1 Observations in Plane-Polarized Light	16
2.1.2 Observations in Crossed-Polarized Light	18
2.1.3 Conoscopy and Interference Figures	21
2.1.4 Determining the Principle Refractive Indices using Biaxial Refractometry	27
2.2 MATERIALS AND METHODS	34
2.2.1 Samples.....	34
2.2.2 Sample Preparation Techniques and Macroscopic Observations.....	35
2.2.3 Polarized Light Microscopy	36
2.2.3 Refractive Index Determinations using Biaxial Refractometry	37
2.3 RESULTS OF OPTICAL CHARACTERIZATION BY POLARIZED LIGHT MICROSCOPY.....	39
2.3.1 Kalamazoo County Sheriff’s Department Case Samples	39
2.3.2 Skymint Dispensary BHO Samples.....	47
2.3.3 Cannabidiol Life Dispensary Samples	53
2.4 DISCUSSION AND COMPARISON OF CRYSTALLINE CHARACTERIZATION BY POLARIZED LIGHT MICROSCOPY.....	62
APPENDIX.....	65
REFERENCES	73
3. SPECTROSCOPIC CHARACTERIZATION AND IDENTIFICATION OF CANNABIS SOLVENT EXTRACT COMPONENTS.....	75
3.1 INSTRUMENTAL THEORY.....	77
3.1.1 Micro-Attenuated Total Reflectance-Fourier Transform Infra-Red Spectroscopy	77

3.1.2 X-Ray Diffraction Theory and Instrumentation	80
3.2 MATERIALS AND METHODS	86
3.2.1 Samples.....	86
3.2.2 Micro-Attenuated Total Reflectance-Fourier Transform Infra-Red Spectroscopy – Sample Preparation.....	87
3.2.3 Single-Crystal X-Ray Diffraction – Sample Preparation	88
3.3 FTIR SPECTROSCOPIC ANALYSIS OF CANNABIS SOLVENT EXTRACTS	89
3.3.1 Results of Micro-ATR-FTIR Analysis of Cannabis Solvent Extracts	89
3.3.1.1 Micro-ATR-FTIR Analysis of Optically Similar Crystals - KCSD Case Samples and Skymint Samples.....	89
3.3.1.2 Micro-ATR-FTIR Analysis of Cannabidiol Life Dispensary Samples	95
3.3.2 Discussion of Micro-ATR-FTIR Analysis of Cannabis Solvent Extracts.....	99
3.4 STRUCTURAL ELUCIDATION OF CANNABIS SOLVENT EXTRACT CRYSTALS	105
3.4.1 Results of Single-Crystal XRD Analysis for Structural Elucidation.....	105
3.4.1.1 Single-Crystal XRD Analysis of Optically Similar Samples - KDPS 18-9026 and WB THCA Crystals	105
3.4.1.2 Single-Crystal XRD Analysis of CBD Shatter Crystals.....	108
3.4.2 Discussion of Single-Crystal XRD Analysis for Structural Elucidation.....	111
APPENDIX.....	119
REFERENCES	130
4. OPTIMIZATION OF THCA DERIVATIZATION USING AN EXPERIMENTAL DESIGN APPROACH	133
4.1 THEORY.....	135
4.1.1 Derivatization Methods	135
4.1.2 Experimental Design	138
4.1.2.1 Full Factorial Screening Design.....	140
4.1.3 Gas Chromatography-Mass Spectrometry.....	143
4.2 MATERIALS AND METHODS	145
4.2.1 Reference Materials and Sample Preparation.....	145
4.2.2 Full Factorial Screening Experiments	146
4.2.2.1 Sample Preparation - THCA Concentration Study.....	148
4.2.2.2 Sample Preparation – Cannabis Extract Sample Analysis.....	149
4.2.3 GC-MS Analysis.....	149
4.2.4 Data Processing and Analysis.....	150
4.2.4.1 Full Factorial Analysis	150
4.3 FULL FACTORIAL SCREENING EXPERIMENT RESULTS AND DISCUSSION ...	151

4.3.1 Full Factorial Screening Design Experiments and Optimization	155
4.3.2 Evaluation of Optimized Method Linearity.....	162
4.3.3 Analysis of Cannabis Solvent Extracts by GC-MS Using the Optimized Derivatization Procedure	164
4.4 CONCLUSIONS	173
APPENDIX IV	174
REFERENCES	185
5. CONCLUSIONS AND FUTURE WORK	188
5.1 CONCLUSIONS.....	188
5.2 FUTURE WORK	192
REFERENCES	193

LIST OF TABLES

Table 2.1 Summary of crystal systems and parameters ⁹	15
Table 2.2 Common interference figures for biaxial refractometry	32
Table 2.3 Sample identifications, sources, and year obtained	35
Table 2.4 KCSD BHO case sample wax consistency and crystalline component summaries	39
Table 2.5 Summary of Case Sample Optical Properties by PLM.....	46
Table 2.6 Skymint BHO macroscopic sample summary	47
Table 2.7 Summary of optical characteristics for Skymint dispensary samples.....	53
Table 2.8 Cannabidiol Life CBD sample summary	54
Table 2.9 Summary of optical characteristics for Cannabidiol Life dispensary samples	61
Table 2.10 Summary of optical characteristics from representative samples of each subset	62
Table A2.1 Table of refractive index measurements (n_{α}) for KDPS 18-9026.....	68
Table A2.2 Table of refractive index measurements (n_{β}) for KDPS 18-9026.....	68
Table A2.3 Table of refractive index measurements (n_{γ}) for KDPS 18-9026.....	69
Table A2.4 Table of refractive index measurements for PPO 14-20332-10	69
Table A2.5 Table of refractive index measurements for KCSD 14-10811-28964	70
Table A2.6 Table of refractive index measurements for KCSD 14-10811-28967	70
Table A2.7 Table of refractive index measurements for KCSD 14-10811-28960.....	70
Table A2.8 Table of refractive index measurements for WB THCA Crystals.....	71
Table A2.9 Table of refractive index measurements for PB THCA Wax	71
Table A2.10 Table of refractive index measurements for CBD Wax.....	72
Table A2.11 Table of refractive index measurements for CBD Crystal.....	72

Table 3.1 Summary of crystal systems with geometric unit cell depictions.....	82
Table 3.2 Sample identifications, sources, and year obtained	86
Table 3.3 KCSD and Skymint sample summary	90
Table 3.4. Cannabidiol Life CBD-containing sample summary.....	96
Table 3.5 Crystal data and structure refinement details of KDPS 18-9026 and WB THCA Crystal samples.....	107
Table 3.6 Crystal data and structure refinement details of CBD Shatter Crystal sample.....	110
Table 3.7 Comparison of refined data for crystals analyzed by single-crystal XRD	117
Table 4.1 Summary of Resolution and Confounding Variables	140
Table 4.2 Example of Experimental Order for Full Factorial Design with Three Factors	141
Table 4.3 Full Factorial Levels for Each Factor	147
Table 4.6 Summary of experiment order, levels, averaged THCA-2TMS abundance, and RSD	156
Table 4.7 Optimum derivatization reaction parameters.....	161
Table 4.8 Summary of concentration study normalized THCA-2TMS abundances and RSDs.	163
Table A4.1 Calculations for the degrees of freedom	175
Table A4.2 Calculations for the sum of squares for two-way ANOVA ¹⁹	175
Table A4.3 Calculations for the mean squares	176
Table. A4.4 Summary of reproducibility for pre-screening hold experiments.....	179
Table A4.5 Inter- and intra-vial RSDs for ethyl acetate and pyridine pre-screening experiments	179
Table A4.6 Full ANOVA results from derivatizations using pyridine as support solvent.....	179
Table A4.7 ANOVA results from derivatizations using ethyl acetate as support solvent.....	180

LIST OF FIGURES

Figure 2.1 Labeled diagram of a polarized light microscope	14
Figure 2.2 Example of relief differences relative to refractive index medium; (a) high relief, (b) low relief	17
Figure 2.3 Diagram illustrating the interaction of light with isotropic media (left) and anisotropic media (right).....	19
Figure 2.4 Michel-Lévy Birefringence Chart ¹¹	20
Figure 2.5 Example of a uniaxial interference figure with key features labeled	23
Figure 2.6 Conoscopic images of uniaxial interference figure orientation changes with microscope stage rotation ¹²	24
Figure 2.7 Example of a biaxial interference figure	25
Figure 2.8 Estimation of biaxial 2V angle based on isogyre curvature in an optic axis interference figure ¹⁰	26
Figure 2.9 Uniaxial indicatrix with principle refractive index views (a) optic normal and (b) optic axis	28
Figure 2.10 Biaxial indicatrix with principle refractive index views (a) optic normal and (b) optic axis, and (c) obtuse bisectrix (Bxo)	29
Figure 2.11 Optically positive (A) and optically negative (B) biaxial indicatrices	31
Figure 2.12 (A) Becke line moving out into higher refractive index medium and (B) into a sample crystal with higher refractive index	33
Figure 2.13 Macroscopic view of case sample KDPS 18-9026 in glass vial	40
Figure 2.14 Photomicrograph of KDPS 18-9026 at 100X magnification in PPL	41
Figure 2.15 Photomicrograph of KDPS 18-9026 at 100X magnification in XPL.....	42
Figure 2.16 KCSD 18-9026 with polarizer at (A) 0° orientation and (B) 90° orientation to demonstrate changes in relief.....	42
Figure 2.17 Conoscopic view of a KDPS 18-9026 crystal displaying an optic axis interference figure	44

Figure 2.18 Macroscopic view of PB THCA wax (A) and WB THCA crystals (B) in dispensary glass containers	48
Figure 2.19 Stereoscopic view of PB THCA wax (A) and WB THCA crystals (B) showing the crystal color in reflected light and agglomerated form.....	49
Figure 2.20 PB THCA wax crystals shown in PPL, note the oily, wax component separate from the crystalline component	49
Figure 2.21 PB THCA wax crystals with polarizer at (A) 0° orientation and (B) 90° orientation to demonstrate changes in relief.....	50
Figure 2.22 Small PB THCA wax crystals in XPL displaying moderate retardation (A) and large crystals showing high order white retardation (B).....	51
Figure 2.23 Conoscopic view of a PB THCA wax crystal displaying an optic axis interference figure.....	52
Figure 2.24 Macroscopic view of CBD wax (A) and CBD crystal (B) samples in dispensary containers	55
Figure 2.25 Stereoscopic view of CBD wax (A) and CBD crystals (B) showing the crystal color in reflected light and the difference in wax presence.	55
Figure 2.26 CBD wax crystals shown in PPL, note the oily, wax component separate from the crystalline component	56
Figure 2.27 CBD wax crystals with polarizer at (A) 0° orientation and (B) 90° orientation to demonstrate changes in relief.....	57
Figure 2.28 CBD wax crystalline component in viewed in XPL	58
Figure 2.29 XPL view of CBD Wax crystal with straight edge parallel to the crosshair of the ocular micrometer (red)	59
Figure 2.30 Conoscopic view of the CBD crystal sample displaying a biaxial optic axis interference figure.....	60
Figure A2.1 Macroscopic (A) and microscopic views of KCSD case sample PPO 14-20332-10 in PPL (B) and XPL (C).....	66
Figure A2.2 Macroscopic (A) and microscopic views of KCSD case sample KCSD 14-10811-28964 in PPL (B) and XPL (C).....	66
Figure A2.3 Macroscopic (A) and microscopic views of KCSD case sample KCSD 14-10811-28960 in PPL (B) and XPL (C).....	66

Figure A2.4 Macroscopic (A) and microscopic views of KCSD case sample KCSD 14-10811-28967 in PPL (B) and XPL (C).....	67
Figure A2.5 Microscopic views of Skymint dispensary sample WB THCA crystals in PPL (A) and XPL (B).....	67
Figure A2.6 Microscopic views of Cannabidiol Life dispensary sample CBD crystals in PPL (A) and XPL (B).....	67
Figure 3.1 Smith’s IlluminatIR II Micro-ATR-FTIR instrumental set-up	79
Figure 3.2 Simplified schematic of an ATR microscope objective and infrared spectrometer commonly used for microscopic infrared analysis	80
Figure 3.3 Illustration for the requirements of Bragg’s Law ¹⁶	84
Figure 3.4 KDPS 18-9026 crystal (top) and wax component (bottom) IR spectrum	91
Figure 3.5 Representative Skymint sample - WB THCA Crystal IR spectrum.....	91
Figure 3.6 Stacked FITR spectra for all sample crystalline components	92
Figure 3.7 Stacked FITR spectra for all case sample wax components.....	93
Figure 3.8 Stacked comparison of THCA CRM (bottom) and case sample KDPS 18-9026 crystal (middle) and wax component (top) micro-ATR-FTIR spectra.....	94
Figure 3.9 Stacked comparison of THC CRM (bottom) and case sample KDPS 18-9026 crystal (middle) and wax component (top) micro-ATR-FTIR spectra.....	95
Figure 3.10 Micro-ATR-FTIR spectrum for the crystalline component of sample CBD Wax crystal (bottom) and wax (top) components	97
Figure 3.11 Micro-ATR-FTIR spectrum for sample CBD Shatter Crystals.....	97
Figure 3.12 Stacked comparison of CBD Shatter Crystal (top) and THCA CRM (bottom)	98
Figure 3.13 Stacked spectra comparing the crystalline components of KDPS 18-9026 (bottom), WB THCA Crystals (middle), and CBD Shatter Crystals (top)	104
Figure 3.14 Crystal structure from case sample KDPS 18-9026 determined by single-crystal XRD shown with molecular labelling scheme.....	106
Figure 3.15 Crystal structure from case sample KDPS 18-9026 displaying racemic, dimer crystalline properties	106

Figure 3.16 Crystal structure from dispensary sample CBD Shatter Crystal determined by single-crystal XRD shown with molecular labelling scheme of chiral atoms.....	109
Figure 3.17 Crystal structure from dispensary sample CBD Shatter Crystal displaying hydrogen bonding and dimer crystalline properties.....	109
Figure 3.18 Comparison of single-crystal XRD refined structures for KDPS 18-9026 (A) and CBD Shatter Crystals (B).....	117
Figure A3.1 Geometric depictions of Bravais lattices ²⁵	120
Figure A3.2 PPO 14-20332-10 micro-ATR-FTIR spectrum.....	121
Figure A3.3 KCSD 14-10811 – 28967 micro-ATR-FTIR spectrum.....	121
Figure A3.4 KCSD 14-10811 – 28960 micro-ATR-FTIR spectrum.....	122
Figure A3.5 KCSD 14-10811 – 28964 micro-ATR-FTIR spectrum.....	122
Figure A3.6 Skymint PB THCA Wax crystalline component spectrum	123
Figure A3.7 PPO 14-20332-10 wax component micro-ATR-FTIR spectrum (baseline corrected)	123
Figure A3.8 KCSD 14-10811 – 28967 wax component micro-ATR-FTIR spectrum (baseline corrected)	124
Figure A3.9 KCSD 14-10811 – 28960 wax component micro-ATR-FTIR spectrum (baseline corrected)	124
Figure A3.10 KCSD 14-10811 – 28964 wax component micro-ATR-FTIR spectrum (baseline corrected)	125
Figure A3.11 KDPS 18-9026 XRD packing diagram	125
Figure A3.12 WB THCA Crystal XRD structure showing chiral centers.....	126
Figure A3.13 WB THCA Crystal XRD structure showing hydrogen bonding	126
Figure A3.14 WB THCA Crystal XRD packing diagram	127
Figure A3.15 CBD Shatter Crystal XRD packing diagram.....	128
Figure A3.16. THCA chemical structure.....	128
Figure A3.17. CBD chemical structure.....	129

Figure 4.1 Example TMS derivatives: (A)hydroxyl, (B) carboxyl, and (C) amide.....	136
Figure 4.2 Averaged chromatograms of THCA derivatizations using ethyl acetate and pyridine	151
Figure 4.3 Mass spectrum and chemical structure of THCA-2TMS	153
Figure 4.4 Mass spectrum and chemical structure of THC-TMS.....	154
Figure 4.5 Overlay of averaged chromatograms from low (dark blue), high (light blue), and center point (dashed) level pyridine supported derivatizations.	158
Figure 4.6 Overlay of averaged chromatograms from low (dark green), high (light green), and center point (dashed) level ethyl acetate supported derivatizations.....	158
Figure 4.7 THCA-2TMS abundance changes with changes in reaction temperature.....	160
Figure 4.8 Overlay of averaged chromatograms from each concentration study	162
Figure 4.9 Chromatogram of case sample KDPS 18-9026.....	165
Figure 4.10 Mass spectrum and chemical structure for CBN-TMS	166
Figure 4.11 Mass spectrum for unidentified peak at 22.2 minutes.....	166
Figure 4.12 Mass spectrum and chemical structure for THCA-2TMS.....	167
Figure 4.13 Chromatogram of Skymint THCA Crystal sample	169
Figure 4.14 Mass spectrum and chemical formula for THCA-2TMS	169
Figure 4.15 Chromatogram of Cannabidiol Life CBD Crystal sample	171
Figure 4.16 Mass spectrum and chemical formula for CBD	171
Figure 4.17 Mass spectrum and chemical structure of CBD-2TMS.....	172
Figure A4.1 THC mass spectrum.....	176
Figure A4.2 NIST library mass spectrum result for THC-TMS.....	177
Figure A4.3 Averaged chromatograms comparing refrigerated and 24 hour hold samples of THCA derivatization using ethyl acetate	178
Figure A4.4 Averaged chromatograms comparing refrigerated and 24 hour hold samples of THCA derivatization using pyridine.....	178

Figure A4.5 Pareto chart for the pyridine full factorial design.....	180
Figure A4.6 Pareto chart for ethyl acetate full factorial design.....	181
Figure A4.7 Regression plot for THCA concentration study	182
Figure A4.8 Manufacturer information and quantification for Skymint THCA Crystal sample	183
Figure A4.9 NIST library mass spectrum for CBN-TMS.....	183
Figure A4.10 NIST library mass spectrum for CBD	183
Figure A4.11 NIST library mass spectrum for CBD-2TMS.....	184

1. INTRODUCTION

1.1 CANNABIS SATIVA – MARIJUANA AND HEMP

Cannabis sativa is federally controlled in the Controlled Substances Act (CSA) as a Schedule I substance, indicating that it has no accepted medical use and a high risk for addiction amongst users.¹ The psychoactive component of *Cannabis sativa* responsible for the associated “high” users feel is the cannabinoid delta-9-tetrahydrocannabinol (Δ^9 -THC). Δ^9 -THC is found in the resinous capitate (globular) trichomes on the leaves and bracts of female *Cannabis sativa* plants.² These globular trichomes also contain over 100 additional cannabinoids related to Δ^9 -THC, but these cannabinoids do not demonstrate psychoactive effects and are being extensively researched for their pharmacological activities. One such cannabinoid of interest for the presented research is delta-9-tetrahydrocannabinolic acid (Δ^9 -THCA), as this cannabinoid is readily converted to Δ^9 -THC through thermal decarboxylation and is often present in marijuana products. Additionally, in recent years, the cannabinoid cannabidiol (CBD) has been researched and marketed for its medical benefits.²

Marijuana and hemp represent two broad classes of *Cannabis sativa* plants. While both marijuana and hemp originate from the *Cannabis sativa* species, they differ in their cannabinoid composition and their legality in the United States. The 2018 United States Agriculture Improvement Act (referred to as the Farm Bill), which approved the legality of hemp and its products, distinguishes hemp and marijuana on the basis of Δ^9 -THC concentration.³ As stated in the Farm Bill, any *Cannabis sativa* plant with less than 0.3% THC (by dry weight) is considered hemp, while any plant with THC content above that threshold is still considered marijuana. As such, the 2018 Farm Bill ratified the production and sale of hemp products while maintaining marijuana as a Schedule I drug.

1.2 CANNABIS SOLVENT EXTRACTS

The isolation and concentration of cannabinoids for the production of cannabis extracts can be performed in a wide range of techniques. While the production of extracts is more commonly performed for the concentration of THC from marijuana, the recreational sale of CBD products has influenced the production of cannabis extracts derived from hemp. Regardless of plant material used, similar techniques can be used to concentrate cannabinoids. Such techniques include manual separation (*e.g.*, hashish), heat and pressure extractions (*e.g.*, rosin), and solvent extractions (*e.g.*, butane hash oil). Solvent extractions can be produced using a variety of solvents, but most commonly hydrocarbons, such as butane or pentane, or supercritical CO₂ (CO₂ in a liquid state) are used.⁴

The solvent selected for extraction impacts the overall concentration of cannabinoids and terpenes present in the final extracted product. Hydrocarbon extractions have been used historically, due to their efficiency for the extraction of both cannabinoids and terpenes from the plant material.⁴ Supercritical CO₂ extraction is a relatively new technique when applied to cannabis solvent extraction and has become popular due to the ability to “tune” the extraction process for the selection of specific cannabinoids and terpenes. Tuning this extraction method by manipulating the pressure and temperature of the extraction provides a variety of products, ranging from pure cannabinoid extracts to mixtures of cannabinoids and terpenes.⁵ The extraction of cannabinoids, specifically CBD, from hemp is most commonly performed using supercritical CO₂.

Butane hash oil (BHO) is a general class of cannabinoid extract using butane as the extract solvent. Butane hash oil is colloquially referred to as wax, shatter, or crumble – each referring to different textures of product made from similar extraction processes. Similar textures

can be achieved using supercritical CO₂ extraction. Due to the solubility of the cannabinoids in butane and supercritical CO₂, their extraction from plant material into the final BHO product increases the total potency of Δ⁹-THC or CBD (depending on extraction from marijuana or hemp) in products, such that BHO extracts are six to eight times more potent than plant material alone.⁶

Prior to recreational legalization in a number of states, clandestine production of BHO extracts were performed using a simple, yet dangerous, procedure. In clandestine laboratories, BHO was generally produced by packing a glass or steel column with cannabis plant material, fitting a filter to the end, passing butane through the column, collecting the extracted material in a glass dish, and allowing the solvent to evaporate. As the solvent (butane) passed through the column, the cannabinoids were readily dissolved and extracted from the trichomes. The danger of clandestine operations was due to the low vapor pressure of butane which, when evaporated from the extract, can result in explosions in open systems. While state-wide legalization has allowed for safer, closed-loop manufacturing systems to be used for large-scale BHO production for recreational sale, clandestine manufacturing of BHO is still performed. The Bureau of Alcohol, Tobacco, Firearms and Explosives (ATF) warns that clandestine BHO production may be greater in states with legalized marijuana, as access to larger amounts of plant material will be easier than in states where recreational sales remain illegal.⁷ States with recreational marijuana, including Michigan and California, have combatted this by outlawing the use of butane or other hydrocarbons for the clandestine production of BHO extracts.^{8,9}

The popularity of cannabis extracts has grown with the federal legality of hemp and the state-wide legalization of recreational marijuana. From 2016 to 2019, the Colorado Marijuana Enforcement Division reported a 128% increase in cannabis extract or concentrate sales.¹⁰

Similar growth has been shown internationally with Canadian recreational extract and concentrate sales increasing 154% between 2018 and 2019.¹⁰ Data specifically on the sale of hemp extracts is limited, however economic projections related to CBD products as a whole estimate the CBD product market will be a \$20 billion dollar industry in the United States alone by 2024.¹¹

1.3 FORENSIC ANALYSIS OF SEIZED DRUGS

The Scientific Working Group for the Analysis of Seized Drugs (SWGDRUG) is a committee working to improve and standardize the forensic analysis of illicit drugs.¹² To improve the quality of drug analysis, SWGDRUG has compiled recommendations as a guideline for forensic laboratories to follow as minimum requirements for drug identification. The guidelines follow an analytical scheme comprised of techniques that can be categorized (A, B, or C) based on their specificity and discriminating power. Category C techniques include color tests or melting point measurements are the least discriminatory, providing only general or class characteristics. Category B techniques, such as microchemical tests and microscopic analysis (specifically for cannabis), and various chromatography methods, provide chemical or physical characteristics, making them more discriminatory and selective than Category C techniques. Category A techniques include mass spectrometry, infrared spectroscopy, and X-ray diffraction and are the most selective and discriminatory, providing structural information toward identification for drug samples.¹² Minimum recommendations for the identification of drug samples include the use of one Category A technique with either another Category A, B, or C. When a Category A technique is not available, three separate techniques are necessary for identification with at least two Category B techniques.¹²

1.4 ADDRESSING THE IDENTIFICATION OF CANNABIS EXTRACTS

The production of cannabis extracts, from both marijuana and hemp, results in a variety of textures of final extracted products. These textures range from viscous to glassy, as well as highly crystalline. The current analysis of cannabis extracts utilizes primarily a Duquenois-Levine color test for the presence of cannabinoids followed by gas chromatography-mass spectrometry (GC-MS) for the identification of cannabinoids (specifically Δ^9 -THC). While this analytical scheme does provide for the identification of the scheduled, federally illegal cannabinoid Δ^9 -THC, little research has been completed characterizing additional cannabinoids or other components of these extracts using alternative SWGDRUG recommended techniques.

While many cannabis solvent extracts appear completely amorphous macroscopically, through microscopic analysis, two distinct components can typically be observed for cannabis solvent extracts. These components include an amorphous wax and well-formed crystalline material. The analysis of these individual components has not been completed using the aforementioned common methods, and as such the separate components have not been characterized or identified. Given the macroscopic similarity of solvent extracts derived from marijuana and hemp, the presence of crystalline material in both may allow for rapid screening based on the optical properties of the crystals. Differentiating marijuana-based and hemp-based solvent extracts by a rapid screening method may provide presumptive identification, more specific than a Duquenois-Levine color test, prior to identification using a SWGDRUG recommended Category A technique. Additionally, with the passage of the 2018 Farm Bill, the differentiation of marijuana and hemp-based products is necessary in a forensic context given the legality of most CBD products (derived from hemp) as opposed to the state-specific recreational legality of THC products.

Similarly, the state-wide mandates regarding the identification of THC potency in products differs across the United States. As such, some forensic laboratories are only responsible for the identification and quantification of total THC potency (THC plus THCA) while others need to identify and quantify both the cannabinoid acids and neutrals. The extensive use of GC-MS for the quantification of cannabinoids in forensic laboratories readily identifies and quantifies cannabinoid neutrals. The identification of cannabinoid acids, however, requires sample derivatization, as decarboxylation of the acids rapidly occurs in the injection port of the GC-MS. This decarboxylation converts the cannabinoid acids into their neutral forms (*i.e.* THCA to THC). In order to combat this issue, research has been performed in the forensic community regarding the identification of total THC potency,^{13,14} as well as determining methods through which both the neutral and acidic cannabinoids can be quantified and identified.^{15,16} Though methods of cannabinoid acid derivatization are available and utilized, this procedure has not been optimized using single cannabinoids, but rather most utilize a mixture of cannabinoid acids and neutrals in their development. By designing and optimizing the method using a mixture of both cannabinoid acids and neutrals, the extent of decarboxylation occurring due to underivatized acidic product cannot be readily differentiated from the abundance of the neutral cannabinoid itself. As such, optimization using a single cannabinoid acid is necessary to qualitatively observe the extent of reaction to ensure the complete derivatization of each cannabinoid acid.

1.5 RESEARCH OBJECTIVES

The proposed research is intended to reduce the knowledge gap present for cannabis extracts by providing a comprehensive optical and chemical characterization for the two components, with much focus placed on the characterization and identification of the crystalline component. This was accomplished through the analysis of both forensic laboratory case samples

as well as commercially available marijuana solvent extracts and hemp-derived CBD extracts. Optical characterization was completed using polarized light microscopy (PLM), while chemical characterization and identification was performed using micro-attenuated total reflectance-Fourier transform infrared spectroscopy (micro-ATR-FTIR), single crystal X-ray Diffraction (XRD), and GC-MS.

Due to the crystalline material present in the cannabis solvent extracts, extensive optical characterization by PLM was performed. Using PLM, the morphology, refractive indices, and characteristics in crossed-polarized light and conoscopic view were used to group crystals from each class of cannabis solvent extract (either marijuana or hemp-derived). Next, spectroscopic analysis of both the wax and crystalline components was performed using micro-ATR-FTIR. The chemical characterization by micro-ATR-FTIR spectroscopy allowed for optically similar crystals to be compared further by structural information. Additionally, analysis by micro-ATR-FTIR provided preliminary identification of both the crystalline and wax components of each cannabis solvent extract. The confirmatory identification of the crystalline components of select crystalline samples was completed by single-crystal XRD. Two subsets of crystals from cannabis solvent extracts – two from marijuana-derived extracts and one from a hemp-derived extract – were identified and spectroscopically characterized by single-crystal XRD to identify the chemical structure as well as the dimensions and angles of the unit cell to further associate the optically similar crystals in each solvent extract subset.

Additionally, due to the common presence of THCA in marijuana-derived extracts, derivatization studies focused on optimizing the derivatization reaction (silylation) of THCA was accomplished using an experimental design procedure. Specifically, a published derivatization procedure was optimized in terms of solvent choice, temperature of derivatization, reaction time,

and solvent to derivatizing agent ratio.¹⁵ Further, the experimental design followed a full factorial screening analysis to determine significant factors for variability in the abundance of derivatized product when analyzed by GC-MS. The optimized procedure was then used to chemically characterize a subset of cannabis solvent extracts produced from both marijuana and hemp. While cannabis solvent extracts were solely analyzed in this work, the optimization of this reaction allows for confident identification and quantification of THCA in a variety of cannabis products and is not exclusively limited to cannabis solvent extracts.

REFERENCES

REFERENCES

- (1) Drug Enforcement Administration. Drug Scheduling
https://www.deadiversion.usdoj.gov/synthetic_drugs/about_sd.html.
- (2) Andre CM, Hausman J-F, Guerriero G. Cannabis sativa: The Plant of the Thousand and One Molecules. *Frontiers in Plant Science* 2016;7.
- (3) Agriculture Improvement Act of 2018 (P.L. 115-334), 2018.
<https://www.congress.gov/115/plaws/publ334/PLAW-115publ334.pdf>
- (4) Beadle, A. Advances in Cannabis Extraction Techniques. *Analytical Cannabis*, 2019.
<https://www.analyticalcannabis.com/articles/advances-in-cannabis-extraction-techniques-311772>
- (5) Rovetto LJ, Aieta NV. Supercritical carbon dioxide extraction of cannabinoids from Cannabis sativa L. *The Journal of Supercritical Fluids* 2017;129:16–27.
- (6) Elsohly MA, Mehmedic Z, Foster S, Gon C, Chandra S, Church JC. Changes in Cannabis Potency Over the Last 2 Decades (1995–2014): Analysis of Current Data in the United States. *Biological Psychiatry* 2016;79(7):613–9.
- (7) Hughes T. ATF warns of danger from 'hash oil' explosions USA Today. 2015;
<https://www.usatoday.com/story/news/nation/2015/05/23/hash-oil-explosions/27737635/>
- (8) Michigan Proposal 18-1. Ballot Measure. 2018;
https://www.michigan.gov/documents/sos/Full_Text_-_CRMLA_635255_7.pdf
- (9) California Legislative Information. Code Section 11379.6. http://leginfo.ca.gov/faces/codes_displaySection.xhtml?lawCode=HSC§ionNum=11379.6
- (10) MacIver B. Increasing Popularity of 7/10 Exemplifies Rise in Cannabis Concentrates. *Cannabis Business Times*. 2020; <https://www.cannabisbusinesstimes.com/article/710-popularity-rises-concentrate-sales/>
- (11) Dance A. As CBD Skyrockets in Popularity, Scientists Scramble to Understand How It's Metabolized. *Scientific American*. 2019; <https://www.scientificamerican.com/article/as-cbd-skyrockets-in-popularity-scientists-scramble-to-understand-how-its-metabolized/>

- (12) Scientific Working Group for the Analysis of Seized Drugs (SWGDRUG) Recommendations, 2019.
http://swgdrug.org/Documents/SWGDRUG%20Recommendations%20Version%208_FINAL_ForPosting_092919.pdf.
- (13) James A. Cannabis Quality Control Testing Using Gas Chromatography. Cannabis Science and Technology 2018;1(2).
- (14) Ruppel TD, Kuffel N, PerkinElmer, Inc. Cannabis Analysis: Potency Testing Identification and Quantification of THC and CBD by GC/FID and GC/MS. Application Note.
https://www.perkinelmer.com/lab-solutions/resources/docs/app_cannabis-analysis-potency-testing-identification-and-quantification-011841b_01.pdf
- (15) Rigdon A. Accurate Quantification of Cannabinoid Acids and Neutrals by GC. Restek.com, 2015.
- (16) Cardenia V, Toschi TG, Scappini S, Rubino RC, Rodriguez-Estrada MT. Development and validation of a Fast gas chromatography/mass spectrometry method for the determination of cannabinoids in Cannabis sativa L. Journal of Food and Drug Analysis 2018;26(4):1283–92.

2. OPTICAL CHARACTERIZATION OF CRYSTALLINE STRUCTURES IN CANNABIS SOLVENT EXTRACTS

The use of microscopy as a forensic technique is most rooted in the trace evidence examination of well-formed crystalline materials commonly found during soil analysis, fibers, and amorphous material such as glass. Though seized drugs identification often utilizes instrumentation such as Fourier transform-infrared spectroscopy and gas chromatography-mass spectrometry, the microscopic characterization of crystalline materials proves beneficial when working with trace amounts of samples. While the use of polarized light microscopy (PLM) has diminished in forensic applications, recent literature highlights the use of PLM as a characterization method for a variety of crystalline samples outside of this field.¹⁻³

Most recent literature shows the use of PLM in the characterization of food and drug crystals, as well as plant and physiological samples. The application of PLM to a variety of materials for identification and characterization is due to the ability to observe the same identifying characteristics of any sample type, as long as light can be transmitted through the sample. Polowsky *et al.* utilized PLM to characterize and identify common surface crystals of smear-ripened cheeses, including ikaite, calcite, and brushite.¹ In this work they specifically utilized PLM for the ability to identify samples based on their refractive index and characteristics in crossed-polarized light (XPL). Further, they compared the identifications made using PLM to those obtained spectroscopically via powder X-ray diffractometry and demonstrated the similarities in identification between the two methods. Duncke *et al.* demonstrated the use of PLM to characterize liquid crystals within Brazilian crude oil samples.² This work highlighted the use of PLM to differentiate and characterize lamellar liquid crystals and noted the environment-specific optical properties of such crystals. Such optical characteristics exploited in

this work were the morphology and micrometry of sample crystals crystallized in different oil environments and birefringence characteristics in XPL. Nie *et al.* employed PLM to study the crystalline solid dispersion rate of salt disproportionation (the conversion from ionized to neutral state) for solid formations of active pharmaceutical ingredients.³ Finally, PLM has been used extensively in the realm of synthetic and natural fiber identification.^{4,5} Most recently, Reffner *et al.* developed a new method by which to differentiate synthetic textile fibers using relative contrast (given by differences in refractive indices) and angle measurements rather than the by standard determination of principle refractive indices.⁶

Similar to aforementioned research regarding crystal characterization, drug analysis utilizes PLM to characterize crystals resulting from microchemical tests often used for presumptive identification of drug samples.⁷ Additionally, as many drug samples, such as methamphetamine and cocaine, themselves are crystalline, they too can be characterized using PLM and their properties can be compared against standard materials acquired by laboratories. In the case of this work, crystalline materials from cannabis solvent extracts of a variety of sources will be characterized and compared. Similar to the literature highlighted, sets of crystals will be characterized to determine similarities in chemical composition based on the optical properties present. Establishing similarity between the optical characteristics of each crystal set will provide precedent that these crystals can be considered comparable in crystal system (unit cell) and chemical structure.

2.1 POLARIZED LIGHT MICROSCOPY

While standard, compound microscopes and stereomicroscopes utilize an unpolarized light source, polarized light microscopes (PLMs) differ in the inclusion of two polarizing films – one at the base of the microscope (the polarizer) and one following the objective lens (the analyzer). The use of polarizing films effectively selects the direction of the light rays entering the sample, allowing only the light rays that are oriented in the East-West (E-W) direction to illuminate the sample. This configuration is shown in **Figure 2.1**, where the main components of a PLM are highlighted.

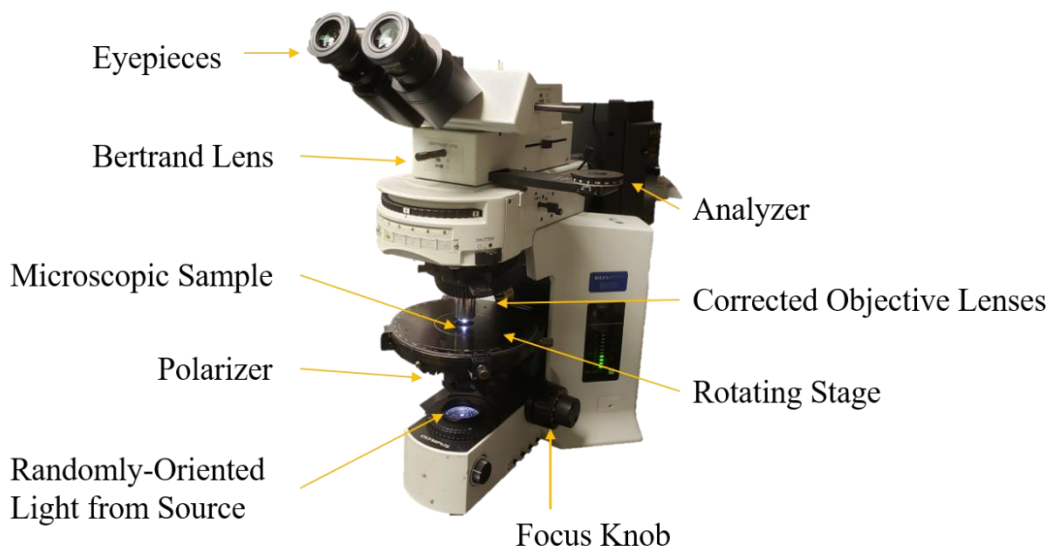


Figure 2.1 Labeled diagram of a polarized light microscope

Polarized light microscopy is used to observe and record the optical characteristics of anisotropic materials – those with more than one refractive index. While materials that are isotropic, including glass and cubic crystals such as table salt, display similar optical characteristics regardless of the orientation of light, anisotropic materials have optical properties that vary with light orientation and interaction with a sample's crystallographic axes. By

orienting parallel light rays to the crystallographic axes of a sample material, unique properties can be observed that are unavailable when using standard compound microscopes. These unique properties include anisometry, pleochroism, refractive index, birefringence, and extinction characteristics.

Utilizing the unique optical properties ascertained by PLM analysis, the crystal system of an unknown sample crystalline material can be determined. The ability to establish the crystal system of an unknown sample is especially advantageous in narrowing down the list of potential identities of an unknown crystal and allows for comparison of crystallographic properties to other techniques, including X-ray crystallography. Crystal systems relate to the shape of the unit cell, including the length and angle between crystallographic axes. Such a determination *via* PLM is made by considering the characteristics of the sample, specifically the number of principle refractive indices present and the extinction characteristics. Every crystal is a member of one of the crystals systems: cubic, tetragonal, hexagonal, rhombohedral, orthorhombic, monoclinic, and triclinic.⁹ **Table 2.1** summarizes the 7 crystal systems and their parameters; a, b, and c refer to crystallographic axes, while α , β , and γ refer to the angles between the three crystallographic axis a, b and c. A more complete explanation of crystal systems as they relate to unit cells and Bravais lattices is discussed in Section 3.1.2.1.

Table 2.1 Summary of crystal systems and parameters⁹

Crystal System	Parameters
Cubic	$a=b=c$; $\alpha=\beta=\gamma=90^\circ$
Tetragonal	$a=b\neq c$; $\alpha=\beta=\gamma=90^\circ$
Hexagonal	$a=b\neq c$; $\alpha=\beta=90^\circ$, $\gamma=120^\circ$
Rhombohedral	$a=b=c$; $\alpha=\beta=\gamma\neq 90^\circ$
Orthorhombic	$a\neq b\neq c$; $\alpha=\beta=\gamma=90^\circ$
Monoclinic	$a\neq b\neq c$; $\alpha=\gamma=90^\circ$, $\beta\neq 90^\circ$
Triclinic	$a\neq b\neq c$; $\alpha\neq\beta\neq\gamma\neq 90^\circ$

2.1.1 Observations in Plane-Polarized Light

Similar to microscopic analysis using standard compound microscopes, simple observations in PLM include morphology, micrometry, and sample color in transmitted light. Morphology refers to the classification of sample shape, including acicular (needle like), conchoidal fractures (irregularly curved and striated surfaces, like that of broken glass), cube (like that of table salt), and anhedral morphology for particles that lack apparent crystalline structures. Micrometry determines the size of the microscopic sample by utilizing a calibrated ocular micrometer. Sample color is recorded as the observed color in transmitted, polarized light and may differ from that of the sample in reflected light.

When light traveling through the microscope assembly is filtered by the polarizer, the illumination is referred to as plane-polarized light (PPL). As shown in **Figure 2.1**, the polarizer of the PLM sits at the base of the apparatus and filters the randomly-oriented light from the source bulb to an ordered, parallel beam of light traveling in only one direction (E-W). When observing samples in PPL, additional characteristics can be determined, including pleochroism, optical relief, and refractive index. Such characteristics cannot be identified using standard compound microscopes, because orientation of the light in one direction is necessary. The determination of these additional characteristics is due to the specific physical phenomena that occur when parallel light interacts with the crystallographic axes and electron environments of anisotropic materials.¹⁰ Pleochroism is a relatively rare feature displayed by colored anisotropic samples and refers to the change in color or brightness of the sample as the vibration direction of light changes due to the interaction of parallel light with the refractive indices.¹⁰ Optical relief refers to the definition of sample boundaries and occurs as light is scattered from the uneven surface of the sample. Relief can be thought of as the contrast between the sample and the

mounting medium (generally a Cargille refractive index liquid), and the extent of relief increases as the difference in refractive index between the sample and mounting medium increases (**Figure 2.2**). Relief is often used to quickly determine the relative refractive index of the sample as compared to the mounting medium.⁹

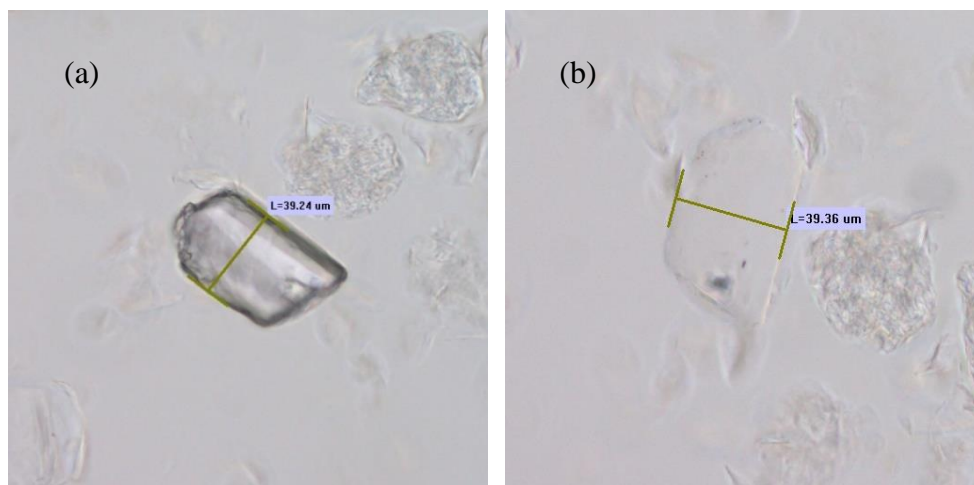


Figure 2.2 Example of relief differences relative to refractive index medium; (a) high relief, (b) low relief

Refractive index determination is generally considered one of the most powerful techniques performed by PLM. By aligning polarized light with the crystallographic axes of a sample, the relative refractive index of the sample can be determined by comparison to the surrounding mounting medium. Though the measurement of the principle refractive indices occurs in PPL, understanding the crystal morphology and orienting the principle refractive indices requires a combination of PLM techniques, including extinction characteristics in XPL and conoscopic observation of the crystal sample. As such, the discussion of these optical characteristics is paramount prior to further explanation of refractometry. More information on

the use of refractometry for the determination of principle refractive indices is provided in Section 2.1.4.

2.1.2 Observations in Crossed-Polarized Light

While light propagating through a PLM sample is subjected to polarization due to the polarizer, a second polarizing film, referred to as the analyzer, can be positioned above the objective lens of the microscope to provide an additional view of light optics through the sample. The analyzer is commonly oriented perpendicular to the lower polarizer in the North-South (N-S) position, and as such when the analyzer is inserted in the light path the sample is said to be viewed in XPL. Due to the perpendicular orientation of the two polarizers, no light passes through the system and a darkfield view is observed.¹⁰

In order to observe samples in XPL, interference of the incident light must occur as it passes through the sample.^{9,10} As such, isotropic samples which do not split the incident light appear black, or extinct, in XPL. Anisotropic samples, however, split the incident light beam into two components due to the multiple refractive indices present in the light path. These two-component light rays destructively interfere with one another and produce polarization colors in XPL, more commonly referred to as retardation colors, when the analyzer recombines components travelling in the same direction and vibrational plane (**Figure 2.3**).¹⁰

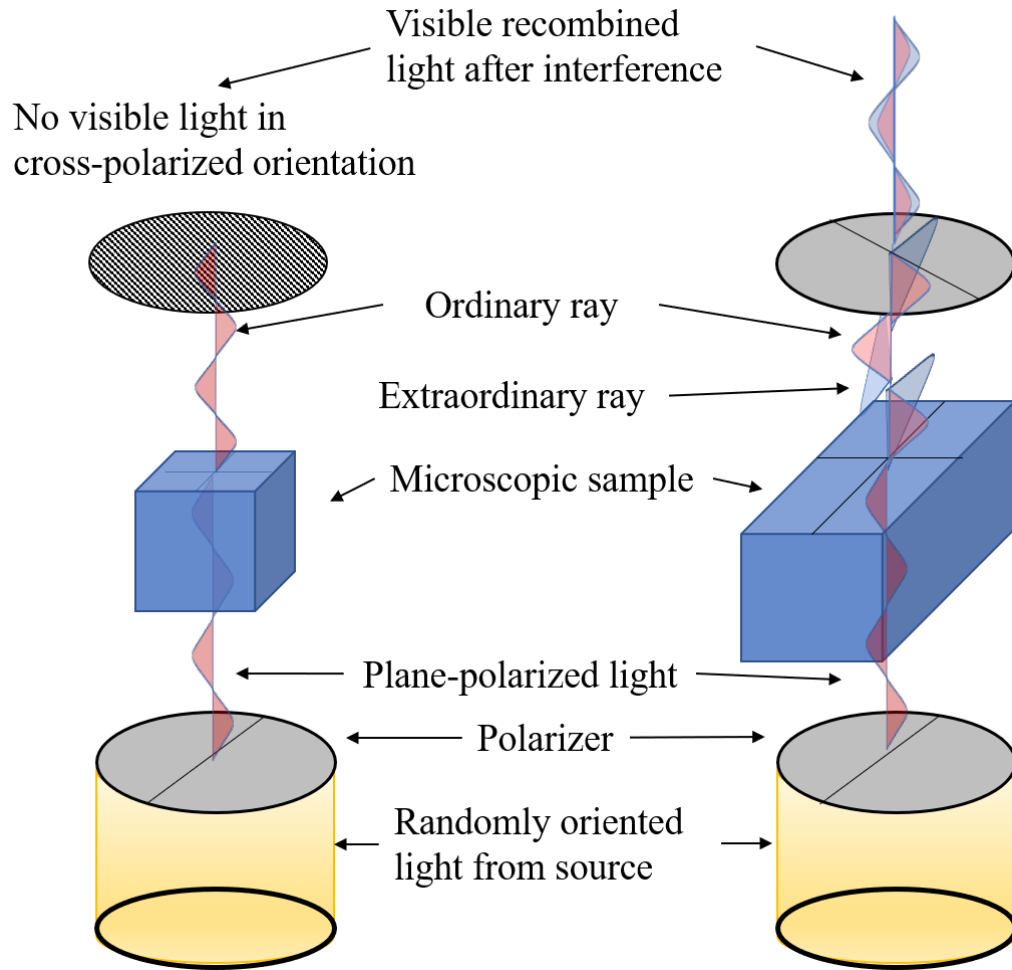


Figure 2.3 Diagram illustrating the interaction of light with isotropic media (left) and anisotropic media (right)

The two components of light – noted as the ordinary and extraordinary ray in **Figure 2.3** – travel orthogonally to one another at different speeds through the sample based on the refractive indices. The difference between the speeds at which the ordinary and extraordinary rays of light is described as birefringence. Birefringence can be measured quantitatively as the numerical difference between the sample’s highest and lowest principle refractive indices. Additionally, birefringence can be observed qualitatively by utilizing a Michel- Lévy birefringence interference color chart (**Figure 2.4**). Additionally, the retardation colors of a

sample can be characterized by comparing the order of red to those displayed in the Michel-Lévy chart.

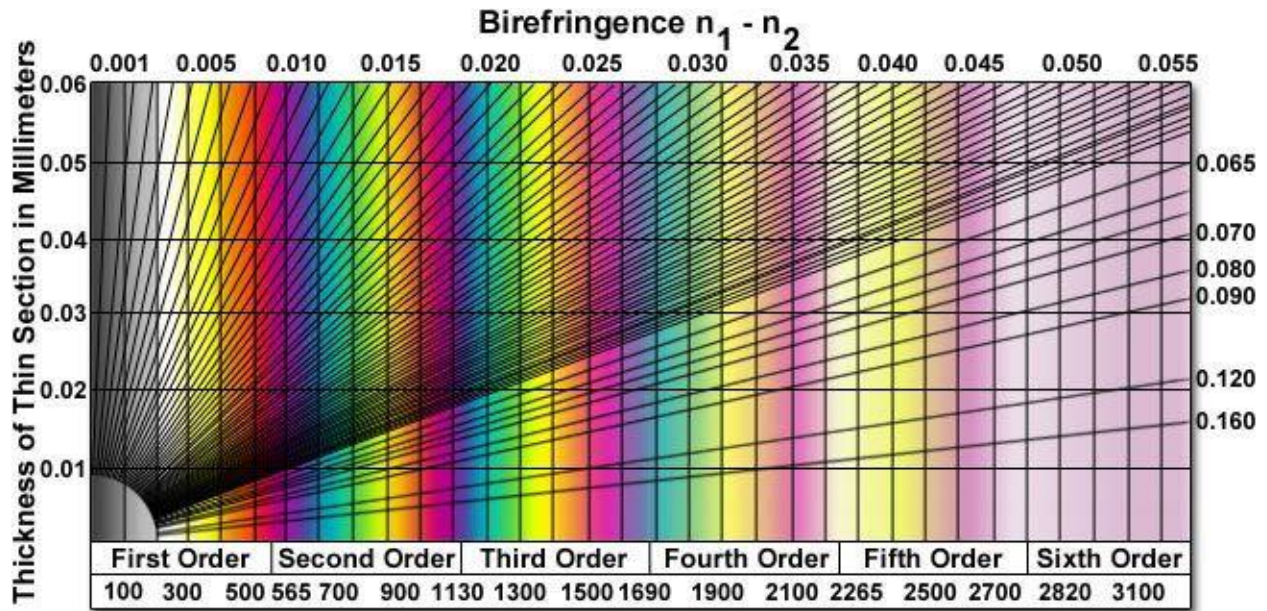


Figure 2.4 Michel-Lévy Birefringence Chart¹¹

Retardation increases linearly with both the thickness and birefringence; thus, the Michel-Lévy chart utilizes both thickness and retardation to determine birefringence of a sample.¹⁰ From **Figure 2.4**, retardation colors are a series of Newtonian colors, which repeat in “orders” that are marked by a red color. Though only showing Newtonian colors through the sixth order, each new order of retardation color becomes less vibrant until approximately the 10th order of red, which can be characterized as “high order white.”⁹ Furthermore, the birefringence of a sample can be categorized into three general categories: low (0 – 0.010), moderate (0.010 – 0.050), and high (>0.050).¹⁰

An additional characteristic observed for anisotropic samples in XPL is extinction. Retardation colors vary in intensity as the sample is rotated relative to the polarizers. This change

in intensity varies cyclically from zero intensity (extinction) to maximum brightness at 45° from extinction and back to zero intensity at 90° rotation. At either extinction point, one principle refractive index is aligned with the polarizers, indicating that only one vibrational direction is passing through the polarizer. This phenomenon occurs regardless of sample rotation for isotropic samples, as the direction of light exiting the sample is unchanged at any orientation relative to the incident light. The extinction of anisotropic samples can be categorized as complete (zero intensity occurs), incomplete (zero intensity does not occur regardless of sample rotation), and oblique (zero intensity occurs at an angle not parallel to the boundaries of a well-formed crystalline sample). Incomplete extinction most often occurs with samples that are comprised of stacked crystal structures, due to the inconsistent orientation of principle refractive indices of each crystal.

2.1.3 Conoscopy and Interference Figures

When viewing a sample in PPL or XPL, an orthoscopic image is produced due to the sample being viewed perpendicular to the path of incident light. An additional technique utilized during PLM analysis is conoscopic characterization of samples, during which conoscopic light is used to analyze the sample, rather than orthoscopic. Under conoscopic conditions, the light coming from the sample is viewed at multiple difference angles simultaneously in a cone of converging light. Unlike orthoscopic analysis, which transmits the image to the focal plan though the oculars, conoscopic images manifest on the back focal plane of the objective lens. Due to this, the use of a Bertrand lens is necessary in order to visualize and interpret the interference figures formed by anisotropic samples.

In conoscopic view, the converging cone of light from the sample travels in various directions, retaining the two-component, orthogonal light waves that originate when polarized light interacts with samples of more than one refractive index. Conoscopic light contains information regarding speed, retardation, and vibration direction from a given sample. **Figure 2.5** provides an example of an interference figure produced by a uniaxial (having two refractive indices) sample. Some features to note include the circles of retardation colors emerging from the center of the interference figure, referred to as isochromes. Each circle represents light with the same retardation and birefringence. The dark cross-shape is made up of isogyres, indicating where there is extinction in the sample due to the parallel polarizers and wave vibrations of the sample. The wedge-shaped, smaller end of the uniaxial isogyre is referred to as the homodrome, and points to the position of the optic axis. The melatope of the interference figure is found where the two isogyres intersect and indicates the position of the optic axis of the sample.¹²

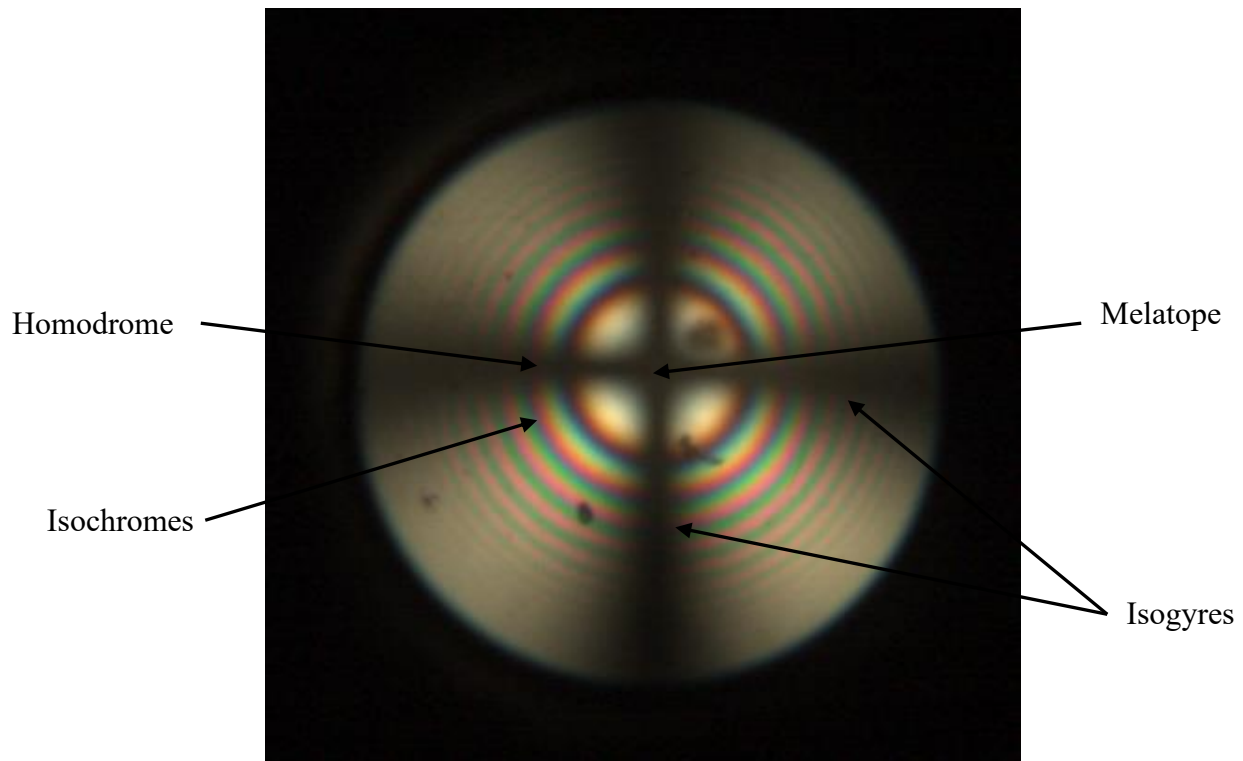


Figure 2.5 Example of a uniaxial interference figure with key features labeled

When rotating the microscope stage, the positioning of the interference figure changes. This is due to the changing shape and symmetry of the isochromes and isogyres with the changing orientation of the sample. As the stage rotates, the sample orientation moves resulting in changes to the travel time of light rays, retardation, and vibration direction. **Figure 2.6** displays how a uniaxial interference figure may change with stage rotation. An exception to this is when the sample is viewed perpendicular to its optic axis, as shown in **Figure 2.5**.

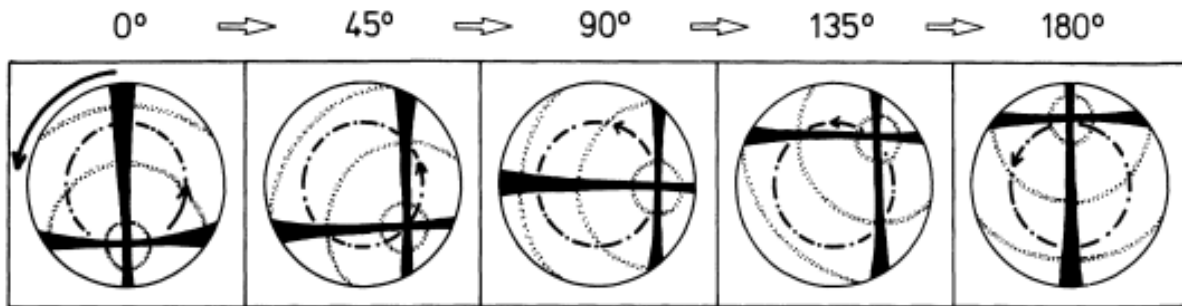


Figure 2.6 Conoscopic images of uniaxial interference figure orientation changes with microscope stage rotation¹²

Biaxial (having three principle refractive indices) samples have distinctly different interference figures when viewed in conoscopic light. **Figure 2.7** provides an example of a biaxial interference figure in a similar optic axis orientation as **Figure 2.5**. Similar to uniaxial interference figures, colorful isochromes emerge from the center of the figure while the black isogyre indicates conoscopic positions of extinction. The melatope can be found at the thinnest point of the isogyre and marks the optic axis for this sample.

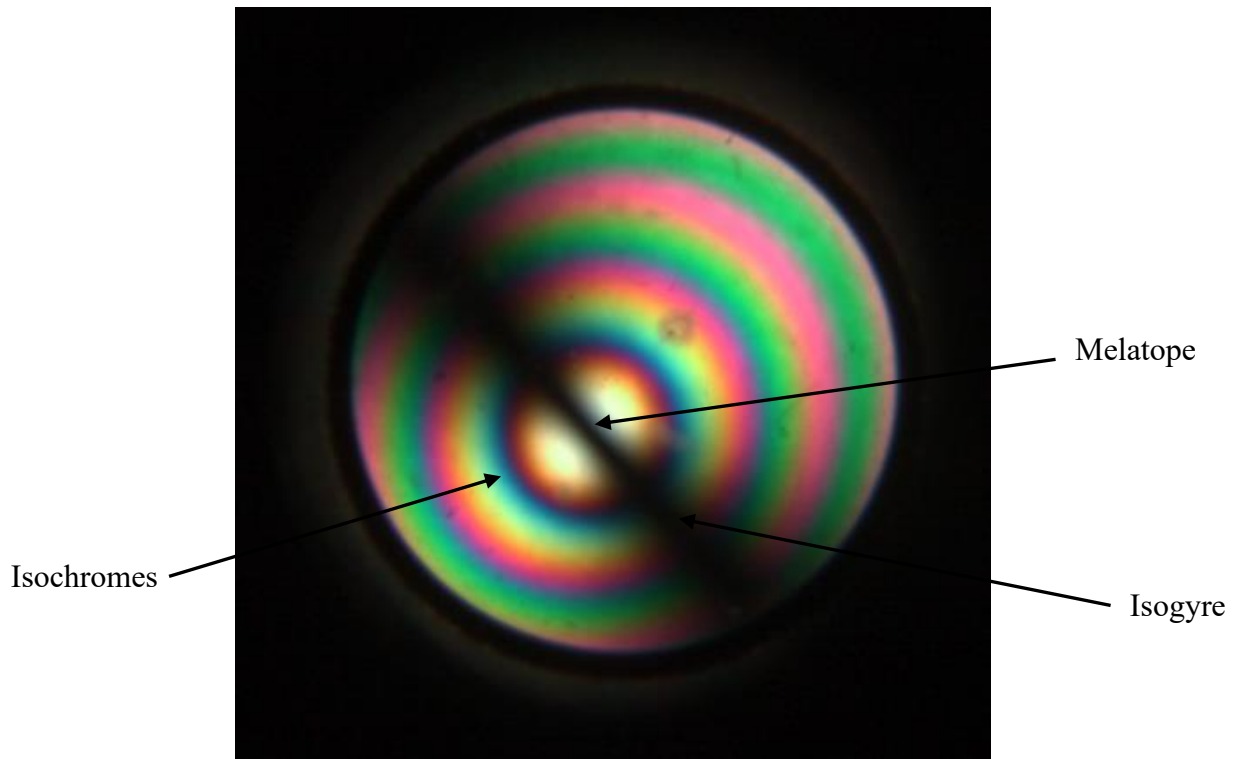


Figure 2.7 Example of a biaxial interference figure

Biaxial interference figures differ in characteristic shape from uniaxial interference figures due to the number and positioning of the optic axes present. Uniaxial samples only have one optic axis, whereas biaxial samples have two at varying positions from one another. When one optic axis is centered and viewed conoscopically, the other optic axis is not in the plane of view. The angle between the two optic axes (referred to as $2V$ angle) can be estimated using the curve of the isogyre. **Figure 2.8** provides a diagram for comparison.

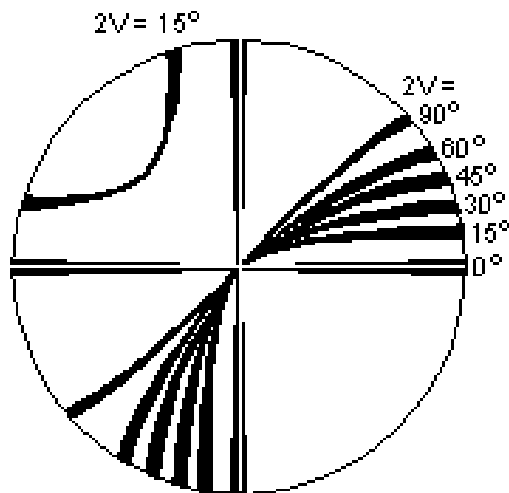


Figure 2.8 Estimation of biaxial $2V$ angle based on isogyre curvature in an optic axis interference figure¹⁰

When compared to **Figure 2.8**, the $2V$ angle of the sample shown in **Figure 2.7** is between $70\text{--}80^\circ$. It should be noted that the curvature of the isogyres decreases until the isogyre forms nearly a straight line at 90° . A $2V$ angle of 0° indicates a uniaxial sample; as such, it is often difficult to differentiate biaxial and uniaxial samples when the $2V$ angle is below 15° . While estimating the $2V$ angle using the curvature of isogyres in an optic axis orientation is a common qualitative method, the exact $2V$ angle can be calculated using an equation following the determination of the three principle refractive indices and the optic sign biaxial sample.

One final characteristic observed in conoscopic light is the optic sign of an anisotropic sample. Anisotropic samples (both uniaxial and biaxial) can be categorized as optically positive (+) or negative (-). Optic sign is related to the refractive indices of anisotropic samples. Uniaxial optic sign is determined by the direction of the principle refractive indices, while the position of the optic axes relative to the principle refractive indices determines the optic sign of a biaxial sample. Due to the close relation of optic sign to refractive index, this characteristic is further discussed in Section 2.1.4.

2.1.4 Determining the Principle Refractive Indices using Biaxial Refractometry

Understanding the orientation of crystallographic axes while observing interference figures is necessary to fully characterize a sample. The conoscopic interference figure provides a visualization of the sample's optical indicatrix (which does not exist in reality), which is used to predict crystal orientation and understand how refractive indices vary with the direction of a sample. To better illustrate this relationship, an example of a uniaxial indicatrix is provided in **Figure 2.9**. For uniaxial indicatrices, the primary axes are labeled X, Y, and Z, and coincide with the crystallographic axes a, b, and c and the refractive indices labeled by the letter n with the corresponding direction subscripted. Further, the optic axis coincides with the c crystallographic axis.

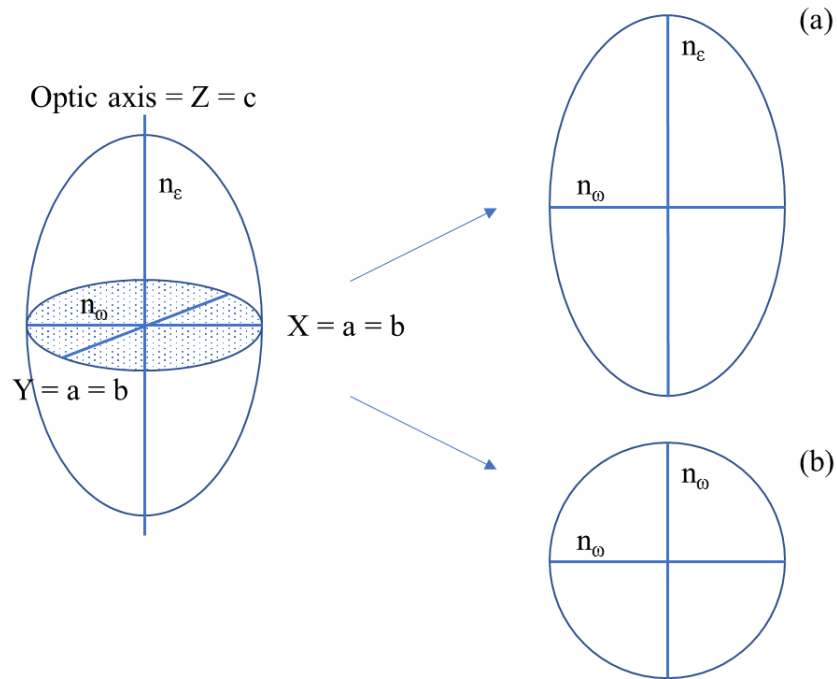


Figure 2.9 Uniaxial indicatrix with principle refractive index views (a) optic normal and (b) optic axis

The uniaxial indicatrix provides a simplified visualization of crystallographic axes and refractive index as they coincide with the primary axes of a crystalline sample. As shown, uniaxial samples have one optic axis, always parallel to the c crystallographic axis, and two refractive indices. The refractive indices are referred to as ordinary (n_o) and extraordinary (n_e). The ordinary and extraordinary refractive indices split the incident parallel light into two perpendicular rays, traveling at different velocities through the sample. The rays are represented by vectors with both direction and magnitude, such that the length of the refractive index vectors in the indicatrix relate to the velocities of light traveling through the sample and thus is proportional to the refractive index. As such, in **Figure 2.9** the velocity of light traveling parallel to Z (the long vector) is greater than the velocity of light parallel to either Y or X (the short vector). The relationship of velocities can also be expressed as the relationship between

refractive indices as $n_\epsilon > n_\omega$. Additionally, the optic axis (denoted as O.A. in **Figure 2.10**) is perpendicular to the n_ω refractive index vector, thus light propagates at the same velocity in all direction (as shown by **Figure 2.9 b**).

Biaxial indicatrices are more complicated than the previous uniaxial example. This is due to the fact that biaxial samples have three different refractive indices and may contained angled crystallographic axes relative to the primary axes. **Figure 2.10** provides an example of a simplified biaxial indicatrix with no angled crystallographic axes.

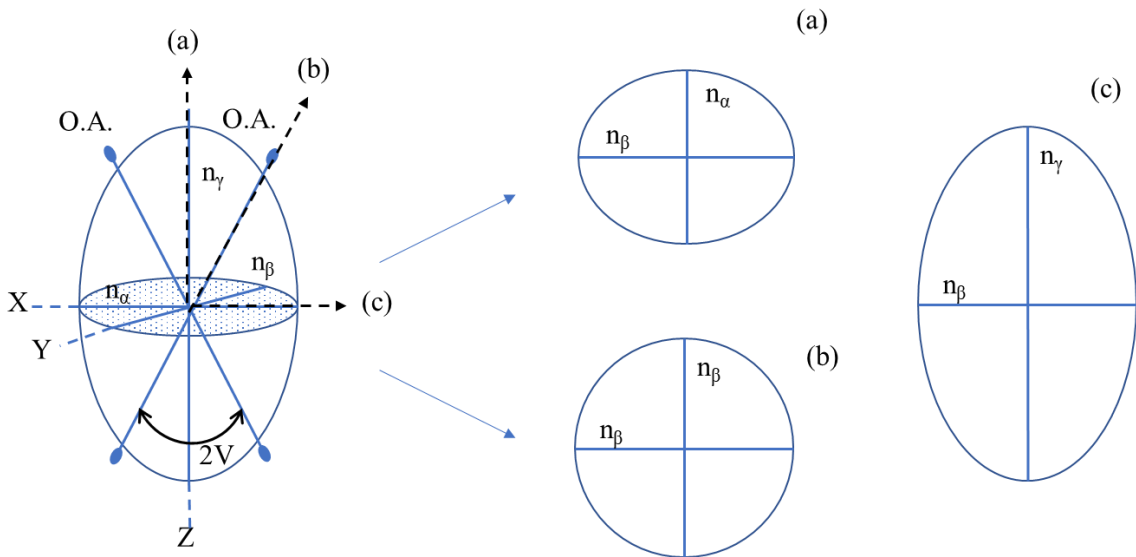


Figure 2.10 Biaxial indicatrix with principle refractive index views (a) optic normal and (b) optic axis, and (c) obtuse bisectrix (Bxo)

Unlike uniaxial samples, where the OA coincides with the primary Z axis and C crystallographic axis, the OAs of biaxial samples do not lie on any primary axis within the crystalline sample. By definition, the OAs are perpendicular to the region of the indicatrix in which light propagates at the same velocity in all directions. In the case of biaxial samples, the OAs are perpendicular to the n_β vector direction and lie between n_γ and n_α .

As discussed in Section 2.1.3, the angle between the two OAs is defined as the 2V angle. **Figure 2.10** displays this characteristic as it relates to the biaxial indicatrix. The relationship between OA location and n_β orientation between n_α and n_γ gives rise to the optic sign of a biaxial sample, as introduced in Section 2.1.3. Since n_β can lie anywhere between n_α and n_γ , it may lie closer to n_α or n_γ in a particular biaxial sample. If n_β is closer to n_α , the optic axes are closer to n_γ and the angle between them is bisected by n_γ . In this case, the OA forms an acute angle with n_γ and n_γ is designated as the acute bisectrix (Bxa). Oppositely, n_α forms an obtuse angle with the OA and is designated as the obtuse bisectrix (Bxo). In this example, when n_β is closer to n_α , the sample is said to be optically positive (+). **Figure 2.11 A** provides an example of a (+) biaxial indicatrix. If, however, n_β lies closer to n_γ , the OAs are at an acute angle with n_α and an obtuse angle with n_γ indicating an optically negative (-) sample (**Figure 2.11 B**).

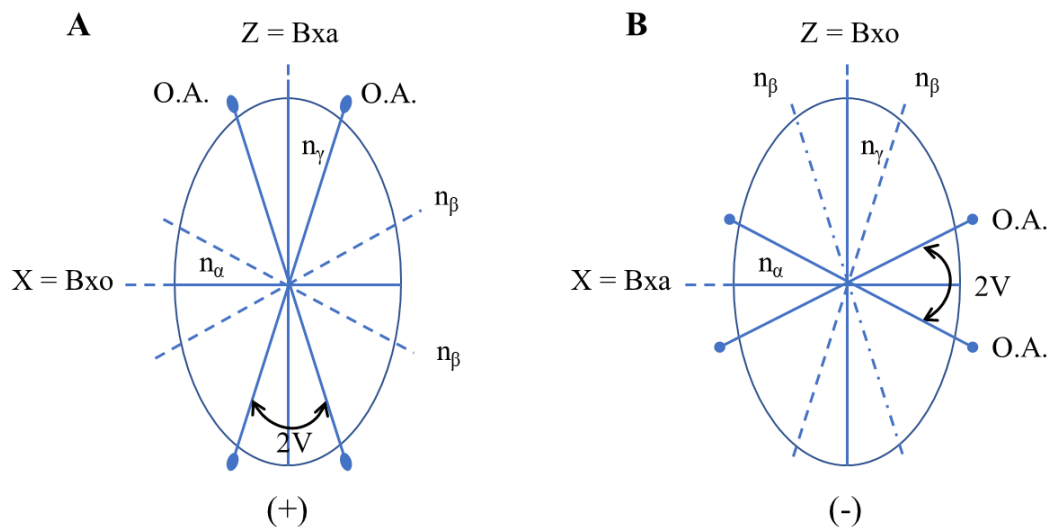


Figure 2.11 Optically positive (A) and optically negative (B) biaxial indicatrices

To measure the principle refractive indices of both uniaxial and biaxial samples, observation of the sample in both orthoscopic and conosopic light is performed. Conoscopic observation provides a method to orient the crystallographic axes and refractive indices, while orthoscopic view is used to perform relative refractive index measurements. As such, it is necessary to understand the relationship between conosopic figures and their associated indicatrix to correctly orient the refractive indices of anisotropic samples. For the purposes of this work, only the characteristic measuring refractive indices for biaxial samples will be discussed.

As discussed in Section 2.1.3, the interaction of conosopic light with a biaxial sample produces characteristic interference figures that can be used in conjunction with the aforementioned biaxial indicatrix to orient the refractive indices. While the specific methods used to select and orient crystal samples will be discussed in Section 2.2.5, **Table 2.2** provides a summary of the common interference figures and the associated principle refractive indices. It

should be noted that n_{β} can be determined from most interference figures, so long as the optic axial plane can be identified.

Table 2.2 Common interference figures for biaxial refractometry

Interference Figure	Refractive Index Determined
Optic Axis	n_{β} only
Acute Bisectrix (Bxa) & Obtuse Bisectrix (Bxo)	n_{β} (always) & n_{α} or n_{γ} based on optic sign
Pendulum Figures	n_{β}
Optic Normal	n_{α} and n_{γ}

Following the determination of crystal orientation *via* conoscopic analysis, the sample's refractive index can be characterized in PPL using the Becke line method. The Becke line refers to the small halo of bright light that moves at the boundary of a transparent sample when the microscope focus is changed¹⁰. The formation of the Becke line around transparent samples is due to the refraction of light as it interacts with media of different refractive indices. **Figure 2.12** provides a visual of the Becke line for a sample.

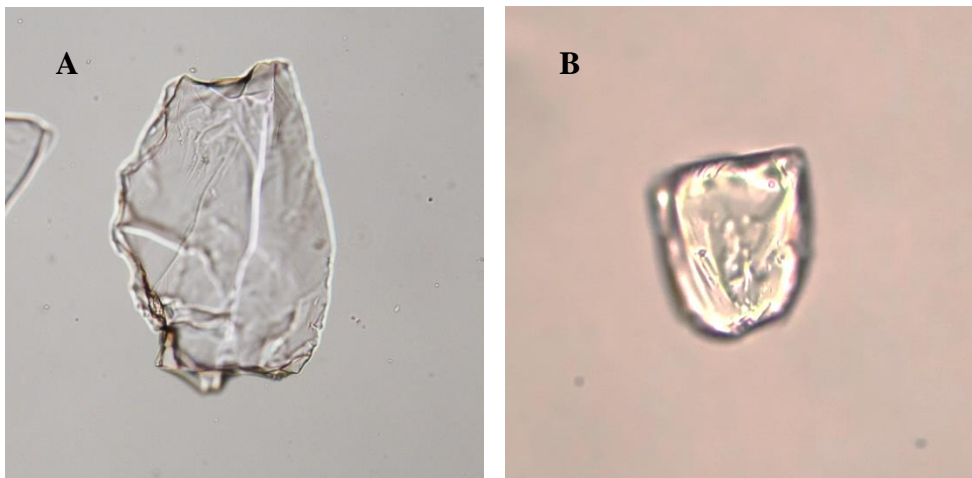


Figure 2.12 (A) Becke line moving out into higher refractive index medium and (B) into a sample crystal with higher refractive index

It should be noted that the Becke line always moves into the medium with a higher refractive index when the microscope is focused above the sample, and as such can be used to compare the relative refractive index of a sample crystal to the refractive index of the surrounding medium (most commonly a Cargille refractive index liquid). For example, **Figure 2.12 A** displays a crystal sample that is higher in refractive index than the surrounding medium while **Figure 2.12 B** shows a crystal sample that is lower in refractive index than the surrounding medium.

2.2 MATERIALS AND METHODS

2.2.1 Samples

Five case samples of marijuana extract (categorized as BHO) submitted to the Kalamazoo County Sheriff's Department (KCSD) were used throughout this work. These case samples ranged in consistency, crystal size distribution, and age, which was defined as the time elapsed since the sample was submitted to the laboratory. To identify each sample, the laboratory assigned case number was used.

An additional four samples were obtained for further characterization. These samples included two BHO samples (crumble and crystals) procured from a local dispensary (Skymint, Lansing, MI) as well as two hemp derived samples purchased from a dispensary (Cannabidiol Life, Sanford, FL) that utilizes hemp produced in Colorado. The Skymint dispensary samples were extracted from marijuana using hydrocarbon solvents similar to the KCSD case samples. The Cannabidiol Life samples were extracted from hemp using supercritical CO₂. **Table 2.3** summarizes the source, identity, and age of samples in this work.

Table 2.3 Sample identifications, sources, and year obtained

Sample Identity	Source	Year Obtained
KDPS 18-9026	KCSD	2018
PPO 14-20332- 10	KCSD	2014
KCSD 14-10811 - 28964	KCSD	2014
KCSD 14-10811 - 28967	KCSD	2014
KCSD 14-10811 - 28960	KCSD	2014
“Punch Breath” Sugar/Wax	Skymint	2020
“Wonka Bars 13” THCA crystals	Skymint	2020
CBD Shatter Crystals	Cannabidiol Life	2020
CBD Crumble/Wax	Cannabidiol Life	2020

2.2.2 Sample Preparation Techniques and Macroscopic Observations

Less than 1 mg of each solvent extract sample was placed on a microscope slide and viewed through a stereomicroscope. Samples were first preliminarily screened for the presence of anisotropic crystalline structures followed by manual separation of the crystal and wax components. Using a fine tungsten needle, the desired crystal was manipulated out of the wax material, taking care to remove as much of the wax as possible without cleaving the crystal. Crystals were selected for microscopic analysis within a desired range of sizes (approximately 50 – 100 μm) as measured using an optical micrometer. Successfully separated crystals were then moved to a separate microscope slide and individually placed under handmade, in-house, 3 mm

micro-cover glasses. Handmade micro-cover glasses were made by scoring standard microscope cover glasses (VWR International, Radnor, PA) with a diamond scribe. Cargille refractive index liquids (Cargille Laboratories, Cedar Grove, NJ) were applied dropwise to each crystal sample prior to characterization by PLM. Additionally, consistency and crystal size were noted for the physical, macroscopic description of each sample. Macroscopic photographs of the samples can be found in the appendix (**Figures A2.1-A2.9**).

2.2.3 Polarized Light Microscopy

Each sample was characterized using generally accepted PLM and optical crystallography techniques on an Olympus BX10 PLM (Olympus Corporations of America, Center Valley, PA). The following characteristics were determined under PPL: size distribution, color, morphology, pleochroism, and the three principle refractive indices. Size distribution was determined using a calibrated ocular micrometer, taking measurements of the crystalline component in PPL. The three principle refractive indices were determined using biaxial refractometry (Section 2.2.4).

Additional characteristics determined using XPL included retardation colors, birefringence, and extinction characteristics. Retardation colors were compared to the Michel Lévy birefringence chart and categorized by orders of red. Birefringence was determined both quantitatively, following the determination of the three principle refractive indices, as well as qualitatively, using the categories discussed in Section 2.1.3.

Finally, in conoscopic light, the optic sign, $2V$ angles, and crystal system were determined for each sample. Optic sign was established using a centered optic axis interference figure, with the concave curve of the isogyre facing north east (NE), and noting constructive or

destructive isochrome interference upon the insertion of a red one waveplate (Olympus Corporations of America, Center Valley, PA). Constructive interference indicates an optically positive crystal, while destructive interference indicates an optically negative crystal. The 2V angle was estimated by comparing the curve of a well-centered optic axis figure with literature schematics derived from Wright (**Figure 2.7**).¹⁰ The crystal system was deduced using information related to the extinction characteristics, number of optic axes, and refractive indices of the sample crystal as discussed in Section 2.1.

2.2.3 Refractive Index Determinations using Biaxial Refractometry

For the determination of the three principle refractive indices, Cargille® refractive index liquids ranging from refractive index 1.4 – 1.8 were used (Cargille Laboratories). Biaxial refractometry was used to correctly identify and align the principle refractive indices of the crystal to the polarizer. Additionally, principle refractive index measurements were determined in triplicate for each refractive index liquid used, and a sodium D filter (Orange21) (The Tiffen Company, Hauppauge, NY) was used for accurate interpretation of Becke line movement.

Due to the hydrophobic nature of the Cargille refractive index liquids and the high lipid affinity of cannabis products, both the crystal and wax components of BHO dissolved in the Cargille liquids during PLM analysis. The rate at which the crystals dissolved was related to the relative strength of the refractive index liquid used. That is, in higher refractive index liquids (i.e., $n_D = 1.68$), crystals dissolved more quickly (~ 30 s) than in lower refractive index liquids (~ 15 min in $n_D = 1.50$). While the chemical composition of the Cargille refractive index liquids is proprietary, it is presumed that the liquids are lipid-based and hydrophobic. As such, it is assumed that the concentration of the proprietary hydrophobic mixture increases with refractive

index, resulting in a faster rate of dissolution. Due to the different rates at which the crystals dissolved into the refractive index liquid, the optical characterization of the crystals was performed as quickly as possible while still maintaining proper technique.

The principle refractive index, n_{β} , was determined by the following method. In XPL, a crystal which showed the lowest retardation as the stage rotated was selected for analysis. This display of retardation colors in XPL indicates that the optic axis of the crystal is perpendicular (or nearly so) to the stage (**Figure 2.9B**). In conoscopic view, the interference figure was characterized for uniaxial or biaxial indicatrix and the optic sign was determined using a red one waveplate (Olympus Corporation of America). Once the orientation for n_{β} was confirmed, the microscope was returned to orthoscopic illumination in PPL and the Becke line method was used to compare the refractive index of the crystal to that of the immersion liquid. To perform the Becke line method, the stage was lowered (raising the objectives), while observing the crystal, and the direction of the Becke line was noted – the Becke line always moves into the medium of higher refraction when the stage is lowered. This process was repeated, following the movement of the Becke line, until a range of refractive indices was determined. Additionally, pendulum figures were also used to orient n_{β} for a given crystal grain. In XPL, a crystal that exhibited moderate retardation colors (between the highest and lowest observed orders of retardation) was selected for analysis. In conoscopic view, n_{β} was positioned parallel to the lower polarizer by orienting the pendulum arm of the isogyres in the N-S direction.

To determine n_{α} and/or n_{γ} , with crossed polarizers, crystals with the highest retardation colors were selected. Selecting a crystal with the highest possible birefringence increased the likelihood of observing a flash interference figure. This interference figure occurs when the crystal is oriented with the optic normal perpendicular to the stage and the optic plane horizontal

to the stage. In XPL, the crystal vibration direction was determined using a red one compensator in order to orient the fast direction parallel to the lower polarizer (this would orient n_α for measurement). To orient n_γ , the stage was rotated 90° such that the slow direction of the crystal was parallel to the lower polarizer. Due to the high order retardation colors exhibited by the crystals in XPL, determining the fast and slow ray directions proved difficult using a red one compensator. Additionally, these refractive indices were measured from a Bxa/Bxo figure, however the flash figure method was most commonly used throughout this work.

2.3 RESULTS OF OPTICAL CHARACTERIZATION BY POLARIZED LIGHT MICROSCOPY

2.3.1 Kalamazoo County Sheriff's Department Case Samples

Older case samples previously analyzed by KCSD were analyzed via PLM and the optical characteristics of the crystalline components were compared (**Table 2.4**).

Table 2.4 KCSD BHO case sample wax consistency and crystalline component summaries

Sample Identity	Sample Consistency	Crystal Size Range (μm)
KDPS 18-9026	Wax (Crumble)	10 – 200
PPO 14-20332 - 10	Wax (Soft – Solid/Hard)	10 – 150
KCSD 14-10811 - 28964	Wax (Soft, Viscous)	10 – 200
KCSD 14-10811 - 28967	Wax/Shatter (Solid, Hard; Glass-like)	10 – 100
KCSD 14-10811 - 28960	Wax (Soft to Glass-like)	10 – 75

Though each sample was fully optically characterized in this work, case sample KDPS 18-9026 was used for initial refractive index determinations due to the ease of crystal isolation. Case sample KDPS 18-9026 was a BHO sample submitted for forensic analysis in 2018, though the date of manufacture is unknown. Macroscopically, this sample consisted of large, yellow orange, anhedral material (**Figure 2.13**). Microscopically, the well-formed crystals were differentiated from the wax component based on color and anisotropy. While the wax component of BHO is typically brown-orange in color, the embedded crystals are colorless (**Figure 2.14**), which is readily observed using a standard stereomicroscope or compound microscope. **Figure 2.14** provides a PPL photomicrograph, showing the difference in color among the particles with colorless crystals (blue circle), dark brown-orange wax (red circle), and light-yellow colored particles where the wax material is lightly stuck to the crystal (green circle).



Figure 2.13 Macroscopic view of case sample KDPS 18-9026 in glass vial

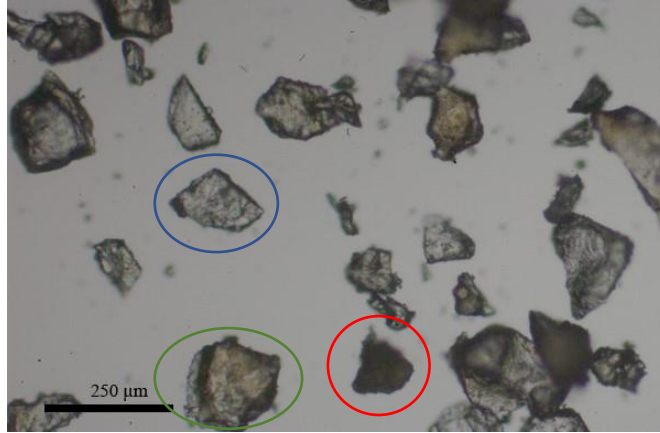


Figure 2.14 Photomicrograph of KDPS 18-9026 at 100X magnification in PPL

Using a PLM in XPL configuration, the distinction between the wax and crystal component becomes even more visible due to the very high order retardation colors exhibited by the crystals, while the wax component does not exhibit retardation colors due to its isotropy.

Figure 2.15 provides a XPL photomicrograph, showing the difference in retardation colors amongst particles with high order white shown by the crystalline material (blue circle) and dark brown-black exhibited by the wax material (red circle). After confirming the presence of crystals using PLM in crossed polarized configuration, crystals were manually separated from the wax and mounted in Cargille refractive index liquids for further optical characterization.

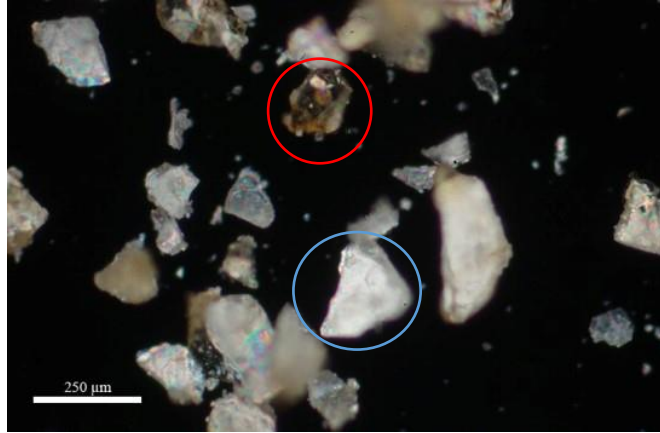


Figure 2.15 Photomicrograph of KDPS 18-9026 at 100X magnification in XPL

In PPL, crystals from case sample KDPS 18-9026 were colorless and displayed no pleochroism. Crystal morphology ranged from thin and platy to anhedral as crystal size increased. Upon the rotation of the microscope stage, the crystal relief was observed to range significantly (**Figure 2.16A and B**) indicating that the difference between the principle refractive indices is extreme.

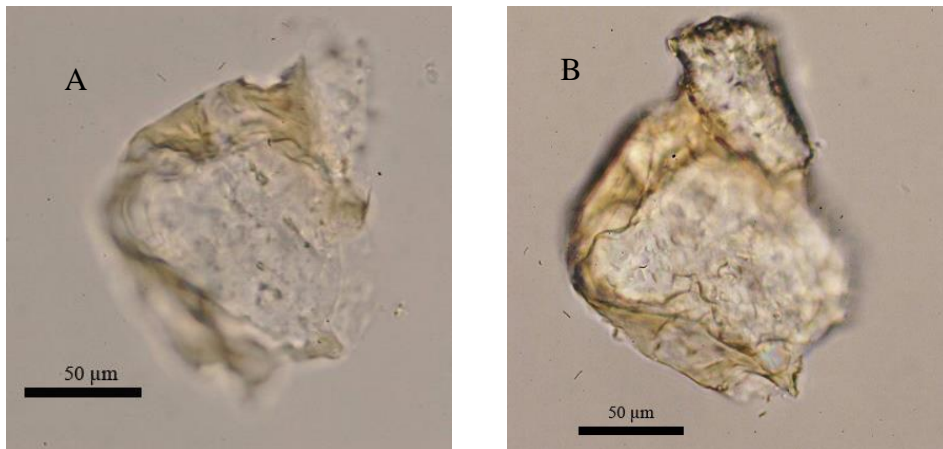


Figure 2.16 KCSD 18-9026 with polarizer at (A) 0° orientation and (B) 90° orientation to demonstrate changes in relief

The maximum retardation colors observed for the sample crystals were high order white, even in moderately sized crystals. High order white retardation was exclusively observed in the majority of samples selected for optical analysis (~100 μm in size). This indicates retardation of more than six orders of red when compared to the Michel-Lévy chart. In XPL, birefringence was estimated using the Michel-Lévy chart which indicated high order white retardation with sample crystals ~50 μm in size. Using this, the birefringence was qualitatively characterized as “high.”

Further observations made in XPL included extinction characteristics. Though the anhedral crystals did not provide a cleavage face by which to measure exact angles of extinction, noting the degree of rotation on the microscope stage at each exhibited extinction allowed for approximate measure of extinction angles. Upon rotation of the stage in XPL, crystal grains exhibited highest order retardation at approximately 45° of stage rotation, and showed no retardation colors, or “went extinct,” at approximately every 90° of rotation. Furthermore, the extinction was complete for each crystal, regardless of size or morphology.

Biaxial refractometry allowed for conoscopic characterization of the sample as well the determination of the principle refractive indices in PPL. During biaxial refractometry procedures, analysis of the crystals in conoscopic view indicated that the crystal was biaxial (containing three principle refractive indices). Biaxial crystals exhibit optic axis interference figures with one curved isogyre that look like cat eyes (**Figure 2.17**). The optic sign was determined to be negative following insertion of a red one waveplate, and destructive interference in regard to isochrome color was observed. Additionally, the $2V$ angle, or angle between the two optic axes, was determined to be $\sim 70^\circ$ when comparing the curvature of the isogyre to literature values⁸.

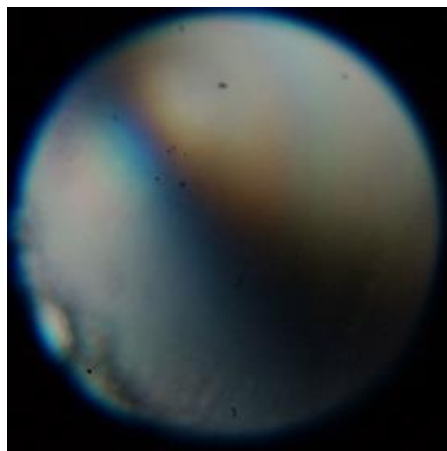


Figure 2.17 Conoscopic view of a KDPS 18-9026 crystal displaying an optic axis interference figure

Using biaxial refractometry techniques, the three principle refractive indices (n_α , n_β , and n_γ) for KDPS 18-9026 were determined. The process of determining each refractive index range was performed in triplicate at each new refractive index. Additionally, new crystals were selected from the bulk BHO material to ensure that the results of the Becke line test were reproducible. As such, to complete the crystal characterization and refractive index determination, over 150 crystals were manually separated from the bulk BHO material, analyzed for characteristics in PPL and XPL, and subjected to biaxial refractometry. The characterization of the principle refractive indices for sample KCSD 18-9026 was reported as ranges, rather than an exact match point. This is a more common approach in optical crystallography and was especially necessary due to any possible change in refractive index from dissolution. Within the range provided, the contrast difference between the crystal and refractive index liquid was extremely low, indicating that the exact match point for the refractive index was very close to the current refractive index being measured. The ranges determined for KDPS 18-9026 are tabulated in **Table 2.5**.

Due to the time-consuming nature of the biaxial refractometry procedure for case sample KDPS 18-9026, relative rather than absolute ranges, refractive indices were determined for crystals of the remaining case samples. Relative refractive index measurements were made in triplicate for each principle refractive index. With that being said, full characterization in PPL, XPL, and conoscopic view was completed for each case sample in similar manner to KCSD 18-9026. In each case, the crystals were selected from the bulk material, mounted in the refractive index liquid, characterized in PPL and XPL, and the Becke line test was performed following orientation using biaxial refractometry. Though these relative refractive indices reported are not given as ranges, the contrast between the crystal and the respective refractive index liquid was very low, indicating that the principle refractive index was very close to the liquid being used for relative determinations. **Table 2.5** summarizes the complete characterization of the five case samples.

Table 2.5 Summary of Case Sample Optical Properties by PLM

Sample	KDPS 18 - 9026	PPO 14 - 20332 - 10	KCSD 14 - 10811 - 28964	KCSD 14 - 10811 - 28967	KCSD 14 - 10811 - 28960
Morphology	Anhedral chunks	Thin/platy - Anhedral chunks	Anhedral chunks	Anhedral chunks	Thin/platy - Anhedral chunks
Size (μm)	10 – 200	10 – 150	10 – 200	10 – 100	10 – 75
Color	Colorless	Colorless	Colorless	Colorless	Colorless
Refractive index (α)	1.4920 – 1.5040 \pm 0.0002	≤ 1.4960	≥ 1.4960	≤ 1.4960	≥ 1.4960
Refractive index (β)	1.6320-1.6330 \pm 0.0002	≥ 1.6320	≥ 1.6320	≥ 1.6320	≥ 1.6320
Refractive index (γ)	1.6850-1.6900 \pm 0.0002	≤ 1.6900	≥ 1.6900	≥ 1.6900	≥ 1.6900
Birefringence	High	High	High	High	High
Extinction characteristics	Complete; $\sim 90^\circ$	Complete; $\sim 90^\circ$	Complete; $\sim 90^\circ$	Complete; $\sim 90^\circ$	Complete; $\sim 90^\circ$
Optic Sign	Biaxial (-)	Biaxial (-)	Biaxial (-)	Biaxial (-)	Biaxial (-)
2V angle	$\sim 70^\circ$	$\sim 70^\circ$	$\sim 70^\circ$	$\sim 70^\circ$	$\sim 70^\circ$

As summarized in **Table 2.5**, the optical characteristics for each case sample display similarities between crystals in BHO samples irrespective of age or consistency (wax-like *versus* glass-like). Crystal sizes in each case sample varied widely, indicating that sample consistency does not appear to affect the size or presence of crystalline material. It should be noted that although crystals between 50 – 100 μm were preferentially analyzed, a crystal of any size would provide similar optical properties and can be used for characterization. Properties in PPL, XPL, and conoscopic view were consistent amongst all case samples. Photomicrographs of each case sample in PPL and XPL are provided for comparison in Appendix II.

Additionally, refractive index measurements were uniform with the exception of principle refractive index n_{γ} in the three KCSD 14-10811 case samples which was slightly higher than the originally determined range from the analysis of case sample KDPS18-9026. The Becke line test for the three case samples for which n_{γ} was slightly higher than the determined range proved difficult due to extremely low contrast between the crystal and refractive index liquid. This very low contrast indicates that although the refractive index may be greater than the established range, it is very close to $n_D = 1.6900$. Similarly, the relative refractive index measurements for the additional four case samples were all performed in Cargille refractive index liquids in which the contrast was very low, indicating that the refractive index of the crystal was very close to that of the liquid.

2.3.2 Skymint Dispensary BHO Samples

Samples were purchased from Skymint, a local Lansing, MI dispensary, for analysis and comparison to the aforementioned samples from KCSD. This subset of crystals was selected to provide characterization of industry-produced, BHO samples as a comparison to the KCSD case samples of unknown origin. Additionally, these samples provide the ability to observe crystal habits in new, relatively young samples, compared to the aged KCSD case samples. **Table 2.6** provides a summary of the macroscopic sample consistency and microscopic crystal size range.

Table 2.6 Skymint BHO macroscopic sample summary

Sample Identity	Sample Consistency	Crystal Size Range (μm)
“Punch Breath” Sugar/Wax	Crystalline/Wax (oil/wax material)	20 – 150
“Wonka Bars 13” THCA crystals	Crystalline Material (No wax)	10 – 150

Each dispensary sample was fully characterized using analogous methods to the KCSD case samples. Macroscopically, these samples differed from the KCSD BHO case samples by containing far less wax material relative to the crystalline component. The “punch breath” sugar/wax sample (referred to as “PB THCA wax”) was a characteristic light orange-brown color and consisted of both crystal and wax material (**Figure 2.18A**). The “Wonka Bars 13” crystal sample (referred to as “WB THCA crystals”), however, was a light off-white color in reflected light and consisted of only agglomerated crystalline material (**Figure 2.18B**).

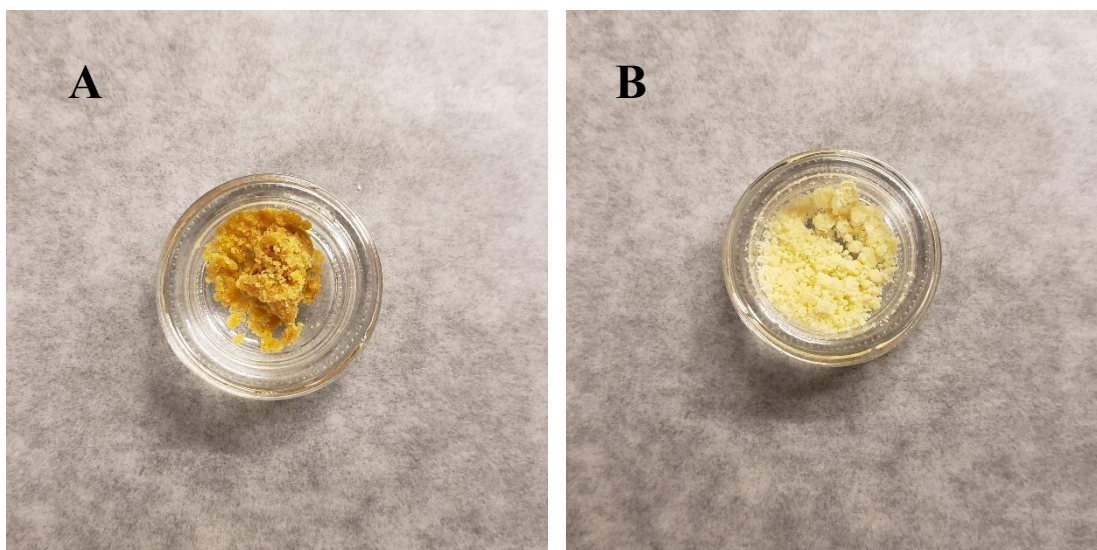


Figure 2.18 Macroscopic view of PB THCA wax (A) and WB THCA crystals (B) in dispensary glass containers

Microscopically, the well-formed crystals in PB THCA wax were readily differentiated from the oily, wax component based on anisotropy. The agglomerated crystals for both samples were colorless, which is readily observed using a standard stereomicroscope or compound microscope (**Figure 2.19 A and B**). The wax component in the PB THCA wax consisted of an oily, liquid residue that did not readily cling to the crystal component (**Figure 2.20**). Using a

stereomicroscope, the dispensary sample crystals were separated from each agglomerate in order to analyze single crystals for analysis.

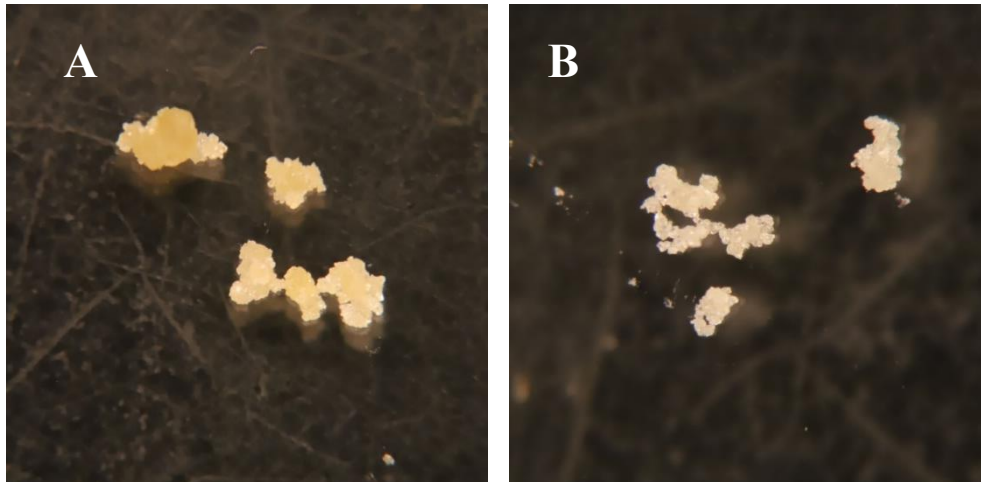


Figure 2.19 Stereoscopic view of PB THCA wax (A) and WB THCA crystals (B) showing the crystal color in reflected light and agglomerated form

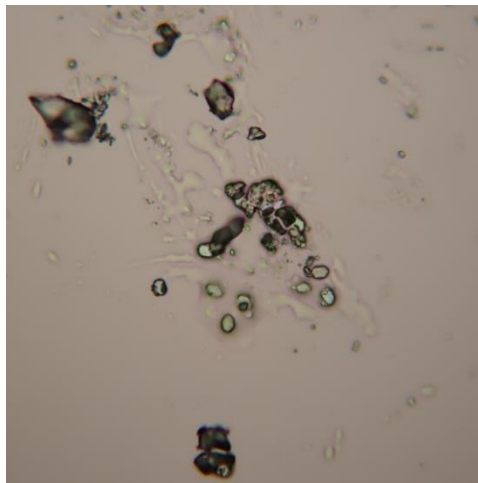


Figure 2.20 PB THCA wax crystals shown in PPL, note the oily, wax component separate from the crystalline component

In PPL, crystals from each dispensary sample were colorless and displayed no pleochroism. Crystal morphology ranged from thin and platy ($\sim 25 \mu\text{m}$ in size) to anhedral as crystal size increased. Crystal relief changed drastically for each sample when the microscope stage was rotated (represented by PB THCA wax crystals in **Figure 2.21 A and B**) indicating that the difference between the principle refractive indices is extreme.

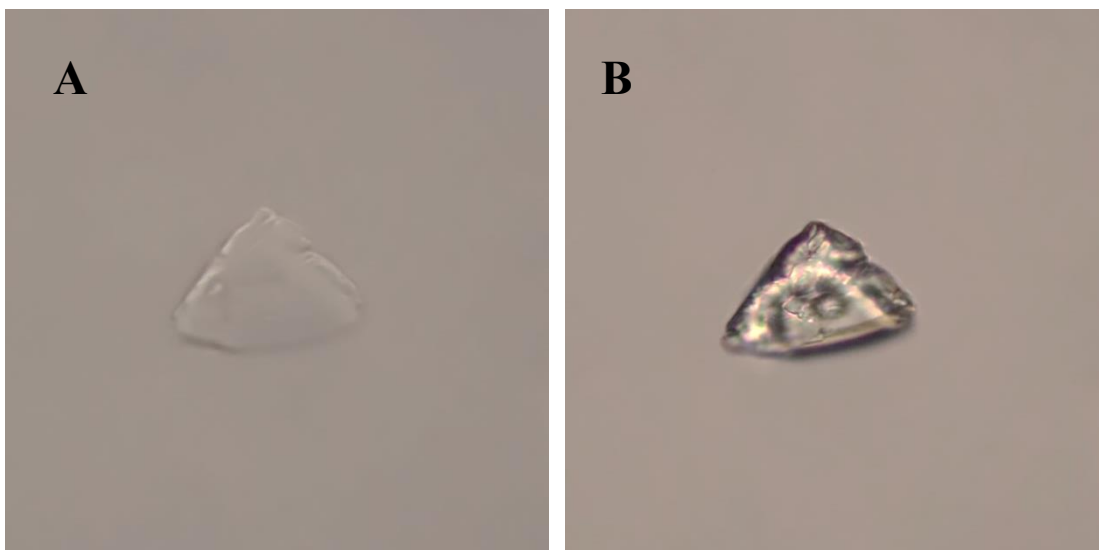


Figure 2.21 PB THCA wax crystals with polarizer at (A) 0° orientation and (B) 90° orientation to demonstrate changes in relief

In XPL, birefringence was estimated using the Michel-Lévy chart. The maximum retardation colors observed for each sample's crystals were high order white, even in moderately sized crystals. Smaller crystals ($\sim 25 \mu\text{m}$ or less in size) with thin, platy morphology displayed retardation in the 2nd – 3rd order of colors when compared to the Michel-Lévy chart (**Figure 2.22 A**). High order white retardation was exclusively observed in the majority of samples selected for optical analysis (those $\sim 50 - 100 \mu\text{m}$ in size) (**Figure 2.22 B**). This indicates retardation of more than six orders of red when compared to the Michel-Lévy chart and corresponds to high birefringence.

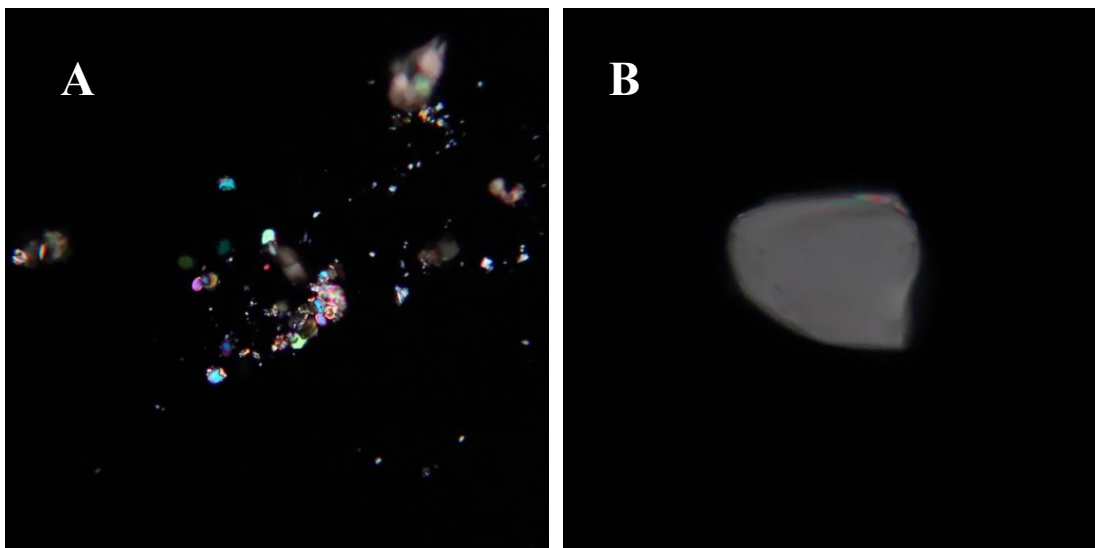


Figure 2.22 Small PB THCA wax crystals in XPL displaying moderate retardation (A) and large crystals showing high order white retardation (B)

Further observations made in XPL included extinction characteristics. Each dispensary sample contained crystals with anhedral morphology, thus no straight cleavage edge by which to measure exact angles of extinction. As such, only approximate extinction angles were noted when rotating the stage by marking the degree of rotation at each exhibited extinction point for the sample. Upon rotation of the stage in XPL, crystal grains exhibited highest order retardation at approximately 45° of stage rotation, and showed no retardation colors, or “went extinct,” at approximately every 90° of rotation. Furthermore, the extinction was complete for each crystal, regardless of size or morphology.

Biaxial refractometry allowed for conoscopic characterization of the sample as well the determination of the principle refractive indices in PPL. During biaxial refractometry procedures, analysis of the crystals in conoscopic view indicated that the crystals from both dispensary samples were biaxial (**Figure 2.23**). The optic sign for both dispensary samples was determined to be negative following insertion of a red one waveplate, and destructive interference in regard

to isochrome color was observed. Additionally, the $2V$ angle, or angle between the two optic axes, was determined to be $\sim 70^\circ$ when comparing the curvature of the isogyre to literature values⁸.

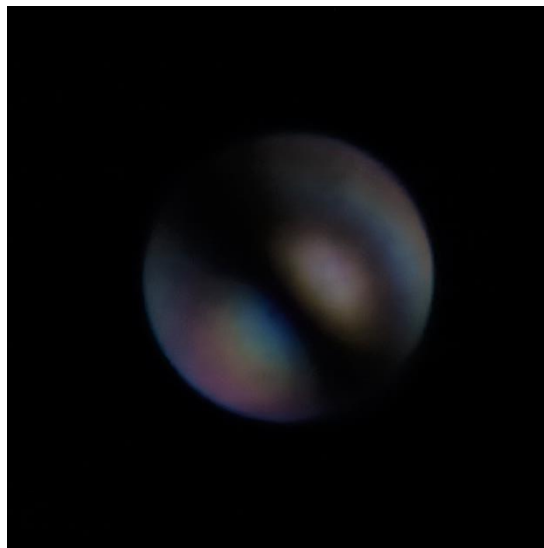


Figure 2.23 Conoscopic view of a PB THCA wax crystal displaying an optic axis interference figure

Using biaxial refractometry techniques, the three principle refractive indices (n_α , n_β , and n_γ) for each dispensary sample were determined. The process of determining each refractive index range was performed in triplicate at each new refractive index. Complete refractive index ranges were determined for each dispensary sample, rather than match points, due to the rapid dissolution of sample crystals into the refractive index liquids. Within the range provided, however, the contrast difference between the crystal and refractive index liquid was extremely low, indicating that the exact match point for the refractive index was very close to the current refractive index being measured. The ranges determined for both the PB THCA wax and WB THCA crystal samples are tabulated in **Table 2.7**.

Table 2.7 Summary of optical characteristics for Skymint dispensary samples

Sample	WB THCA crystals	PB THCA wax
Morphology	Thin/platy - Anhedral chunks (agglomerated)	Thin/platy - Anhedral chunks (agglomerated)
Size (μm)	10 – 150	20 – 150
Color	Colorless	Colorless
Refractive index (α)	1.4920 – 1.5000 \pm 0.0002	1.4920 – 1.5040 \pm 0.0002
Refractive index (β)	1.6300 – 1.6320 \pm 0.0002	1.6300 – 1.6320 \pm 0.0002
Refractive index (γ)	≥ 1.700	≥ 1.700
Birefringence	High	High
Extinction characteristics	Complete; $\sim 90^\circ$	Complete; $\sim 90^\circ$
Optic Sign	Biaxial (-)	Biaxial (-)
2V angle	$\sim 70^\circ$	$\sim 70^\circ$

2.3.3 Cannabidiol Life Dispensary Samples

Hemp-derived solvent extract samples were purchased from Cannabidiol Life, an online-based Florida dispensary, which sources its hemp products from Colorado. This subset of crystals was selected to provide characterization of industry-produced hemp derived samples as a comparison to the BHO samples from KCSD and Skymint dispensary. Additionally, these samples provide the ability to observe crystal habits of an assumed different cannabinoid, as the samples were derived from hemp rather than marijuana. It is the aim of this subset to provide a comprehensive characterization of such crystals in order to propose PLM characterization as a method through which extracts can be potentially screened prior to chemical analysis. **Table 2.8** provides a summary of the macroscopic sample consistency and microscopic crystal size range.

Table 2.8 Cannabidiol Life CBD sample summary

Sample Identity	Sample Consistency	Crystal Size Range (μm)
CBD Crumble/Wax	Crystalline Material Oily Wax	130 - 800
CBD Shatter Crystals	Crystalline Material	100 - 1200

Each dispensary sample was fully characterized using analogous methods to the aforementioned KCSD case samples and Skymint dispensary samples. Macroscopically, these samples differed from one another, as the CBD Crumble/Wax (referred to as “CBD wax”) was dark orange-brown in color, while the CBD Shatter Crystals (referred to as “CBD crystals”) were light yellow and off white in color. Additionally, the CBD wax sample consisted of both crystal and wax material (**Figure 2.24A**), while the CBD crystal sample consisted of only well-formed crystalline material (**Figure 2.24B**).

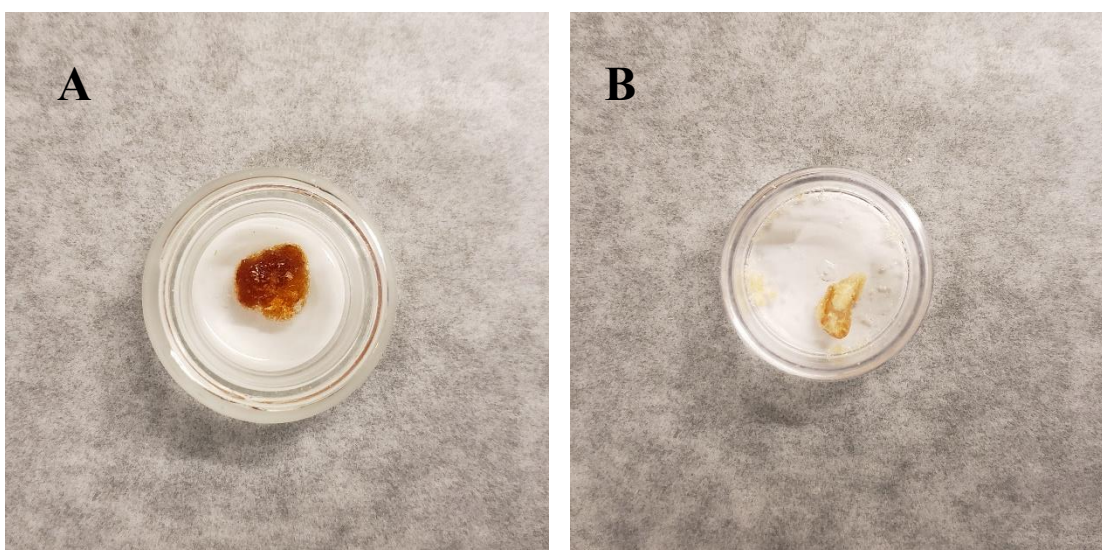


Figure 2.24 Macroscopic view of CBD wax (A) and CBD crystal (B) samples in dispensary containers

Microscopically, the well-formed crystals in CBD wax were readily differentiated from the oily, wax component based on anisotropy. The well-formed crystals for both samples were colorless, which is readily observed using a standard stereomicroscope or compound microscope (**Figure 2.25 A and B**). The wax component in the CBD wax sample consisted of an oily, liquid residue that did not readily cling to the crystal component (**Figure 2.26**). Using a stereomicroscope, the dispensary sample crystals were separated from each agglomerate in order to analyze single crystals for analysis.

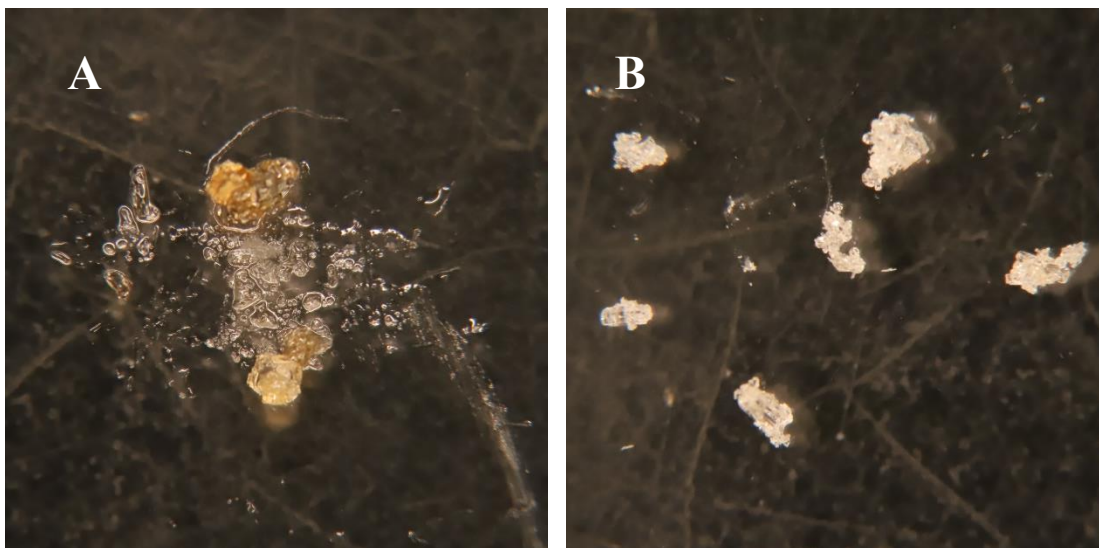


Figure 2.25 Stereoscopic view of CBD wax (A) and CBD crystals (B) showing the crystal color in reflected light and the difference in wax presence.

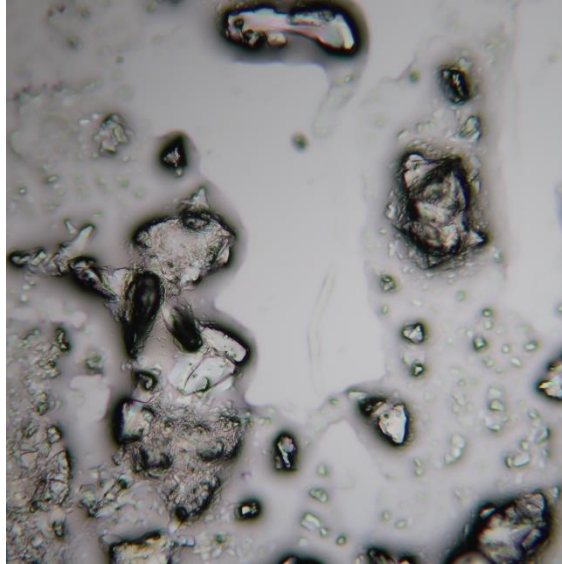


Figure 2.26 CBD wax crystals shown in PPL, note the oily, wax component separate from the crystalline component

In PPL, crystals from each CBD dispensary sample were colorless and displayed no pleochroism. Both the CBD wax and CBD crystal samples contained very well-formed crystals that had rod-shaped morphology and slightly angled edges. Crystal size ranged drastically in each sample from $\sim 100 \mu\text{m}$ to over $1000 \mu\text{m}$, each with similar morphologies in the well-formed crystals. Additionally, the sample crystals regularly broke apart in irregular patterns, leading to anhedral crystals in the gross sample, as displayed by **Figure 2.26**. Crystal relief changed for each sample when the microscope stage was rotated, though not as drastically. The differences in relief is represented by CBD wax crystals in **Figure 2.27 A and B** and indicates a moderate difference between the principle refractive indices.

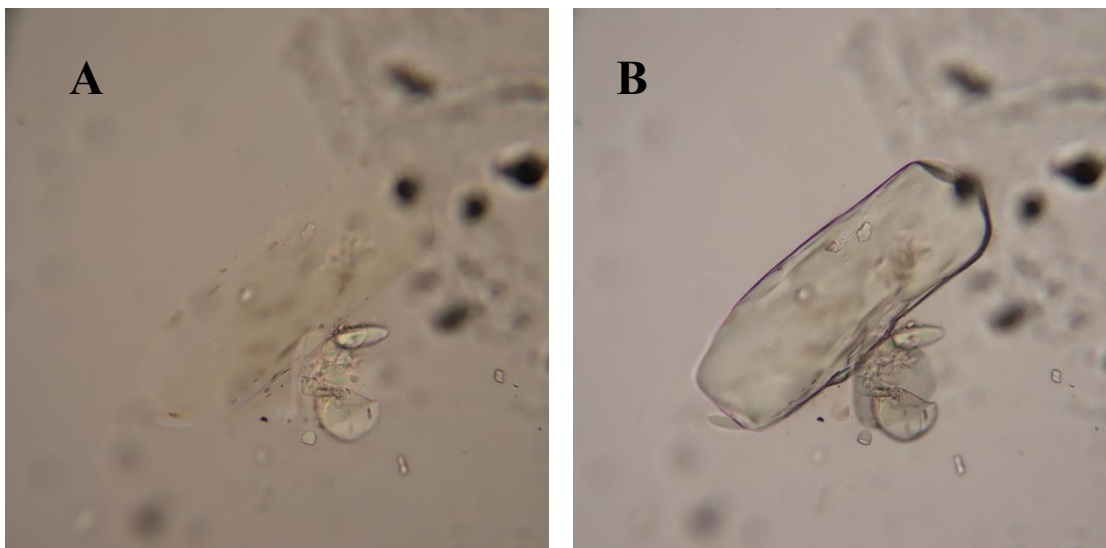


Figure 2.27 CBD wax crystals with polarizer at (A) 0° orientation and (B) 90° orientation to demonstrate changes in relief.

In XPL, birefringence was estimated using the Michel-Lévy chart. The maximum retardation colors observed for each sample's crystals were high order white for very large crystals, but moderate retardation (2nd – 3rd order red) in smaller, cleaved crystals (**Figure 2.28**). The high order white retardation in large crystals and moderate retardation in smaller crystals indicates a moderate-high overall birefringence of the crystalline component of both CBD dispensary samples.

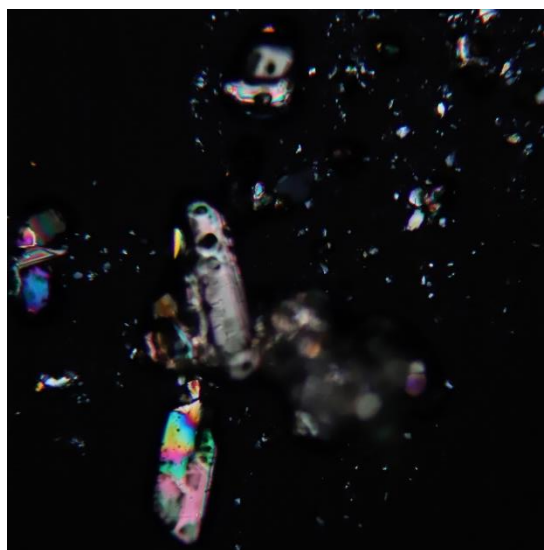


Figure 2.28 CBD wax crystalline component in viewed in XPL

Further observations made in XPL included extinction characteristics. Each dispensary sample contained crystals with well-formed, rod-shaped morphology with straight cleavage edges by which to measure exact angles of extinction. When the crystal edge was parallel to the vertical crosshair of the ocular micrometer, the crystal grain remained visible in XPL (**Figure 2.29**). This indicated a degree of inclined extinction, which was then measured using the straight edge of the crystal, noting the degree of rotation from the straight edge necessary to achieve complete extinction. Crystal extinction occurred regularly at every 90° of stage rotation but was inclined relative to the crystal edge at 44-46°.

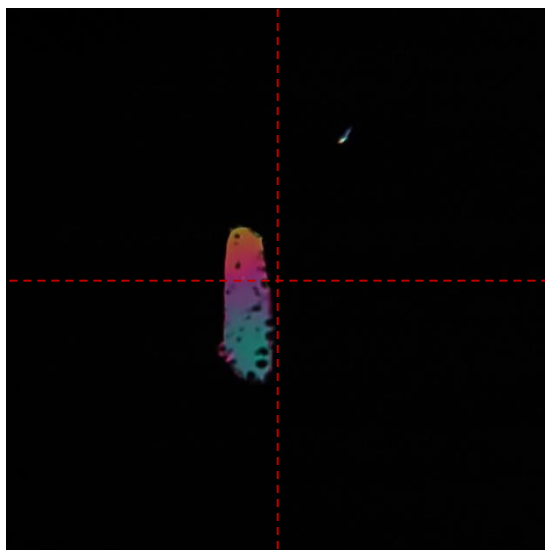


Figure 2.29 XPL view of CBD Wax crystal with straight edge parallel to the crosshair of the ocular micrometer (red)

During biaxial refractometry procedures, analysis of the crystals in conoscopic view indicated that the crystals from both CBD dispensary samples were biaxial (**Figure 2.30**). The optic sign for both dispensary samples was determined to be positive following insertion of a red one waveplate, and constructive interference in regard to isochrome color was observed. Additionally, the 2V angle, or angle between the two optic axes, was determined to be $\sim 80\text{-}90^\circ$, as the isochrome curvature was nearly straight. Further, using biaxial refractometry techniques, the ranges for three principle refractive indices (n_α , n_β , and n_γ) for each dispensary sample were determined (**Table 2.9**).

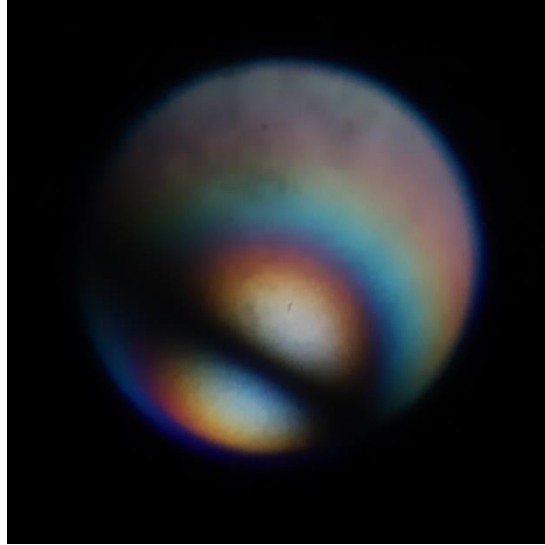


Figure 2.30 Conoscopic view of the CBD crystal sample displaying a biaxial optic axis interference figure

Table 2.9 Summary of optical characteristics for Cannabidiol Life dispensary samples

Sample	CBD crystals	CBD wax
Morphology	Rod-shaped to Anhedral chunks (fragments)	Rod-shaped to Anhedral chunks (fragments)
Size (μm)	100 - 1200	100 – 800
Color	Colorless	Colorless
Refractive index (α)	1.5560 – 1.5600 \pm 0.0002	1.5560 – 1.5600 \pm 0.0002
Refractive index (β)	1.600 – 1.6040 \pm 0.0002	1.600 – 1.6040 \pm 0.0002
Refractive index (γ)	1.6600 – 1.6700 \pm 0.0002	1.6600 – 1.6700 \pm 0.0002
Birefringence	High (>0.05)	High (>0.05)
Extinction characteristics	Complete; $\sim 90^\circ$ Inclined $\sim 45^\circ$	Complete; $\sim 90^\circ$ Inclined $\sim 45^\circ$
Optic Sign	Biaxial (+)	Biaxial (+)
2V angle	$\sim 80-90^\circ$	$\sim 80-90^\circ$

As summarized in **Table 2.9**, the crystalline components within each CBD dispensary sample were analogous. Additionally, when performing biaxial refractometry to determine the principle refractive indices of the crystal samples, it was noted that the high 2V angle directly correlated to the possible numerical value for n_β . Given that the 2V angle relates to the angle between both optic axes, and optic sign relates to the bisection of the optic axes by either n_α or n_γ the assumption could be made by the given characteristics that n_β would be nearly equal to half the difference between n_α and n_γ . Further, n_β would be closer in numerical value to n_α given the optic sign. This is well represented by the optical results provided in **Table 2.9**.

2.4 DISCUSSION AND COMPARISON OF CRYSTALLINE CHARACTERIZATION BY POLARIZED LIGHT MICROSCOPY

The optical characterization of the KCSD BHO case samples indicated similar classes of crystals both within individual case samples and among the entire subset of BHO samples. Similarly, commonalities in optical properties between the representative KCSD case sample (KDPS 18-9026) and Skymint dispensary samples were observed by comparing the results summarized in **Tables 2.5** and **2.7**. When comparing the optical characteristics of the analogous KCSD and Skymint crystals to that of the Cannabidiol Life, obvious differences arose. These optical differences directly related to differences in crystal structure and categorization of crystal system for each subset of samples. The optical characteristics for representative samples from each subset are provided by **Table 2.10**.

Table 2.10 Summary of optical characteristics from representative samples of each subset

Sample	KDPS 18-9026	WB THCA crystals	CBD crystals
Morphology	Anhedral chunks	Thin/platy - Anhedral chunks (agglomerated)	Rod-shaped to Anhedral chunks (fragments)
Size (µm)	10 – 200	10 – 150	100 - 1200
Color	Colorless	Colorless	Colorless
Refractive index (α)	1.4920 – 1.5040 ± 0.0002	1.4920 – 1.5000 ± 0.0002	1.5560 – 1.5600± 0.0002
Refractive index (β)	1.6320 –1.6330 ± 0.0002	1.6300 –1.6320 ± 0.0002	1.600 –1.6040 ± 0.0002
Refractive index (γ)	1.6850 –1.6900 ± 0.0002	≥ 1.700	1.6600 – 1.6700 ± 0.0002
Birefringence	High	High	High (>0.05)
Extinction characteristics	Complete; ~90°	Complete; ~90°	Complete; ~90° Inclined ~ 45°
Optic Sign	Biaxial (-)	Biaxial (-)	Biaxial (+)
2V angle	~70°	~70°	~80-90°

By utilizing the optical properties recorded for both the KCSD case samples and Skymint dispensary samples the crystal system for this set of crystals can be determined. The characteristics observed in XPL provided insight related to the possible crystal system of the samples. First, the anisotropy of the crystals, highlighted by the high order retardation and high birefringence, indicated that the sample contained more than one refractive index. This refined the possible crystal system to those with unequal crystallographic axis lengths (*i.e.*, $a=b\neq c$ or $a\neq b\neq c$). Extinction characteristics further relates to the angle between crystallographic axes of the sample, and as such can provide insight regarding crystal system. Given that the extinction for the crystals in each KCSD and Skymint sample occurred completely at approximately 90° of rotation, crystal systems could be refined to only those that have mutually perpendicular crystallographic axes (*i.e.* $\alpha=\beta=\gamma=90^\circ$).

The characteristics established through biaxial refractometry, including conoscopic characterization and refractive index determination, allowed for further crystal system refinement. In conoscopic view, a biaxial interference figure indicated that the sample contained two optic axes and three principle refractive indices. Noting this, the possible crystal system was identified as one with three unequal crystallographic axes ($a\neq b\neq c$): orthorhombic, monoclinic, or triclinic. Taking the XPL characteristics into consideration, specifically extinction characteristics, the crystal system for the crystal material from both the KCSD case samples and Skymint dispensary samples was categorized as orthorhombic. Given the presence of only one analogous crystal type in each case sample, similarities in chemical composition can be inferred between the clandestine and dispensary produced BHO samples.

Additionally, the crystal system for the crystalline component of the CBD dispensary samples can be determined in a similar fashion as the KCSD and Skymint samples above. The

anisotropy observed in XPL highlighted by the moderate to high order retardation and high birefringence indicated that the samples contained more than one refractive index. This refined the possible crystal system to those with unequal crystallographic axis lengths. Given that the extinction for the crystals in the dispensary samples occurred completely at approximately 90° of rotation, but that at least one principle refractive index aligned with the polarizer at an inclined (~45°) angle, the crystal systems for both the CBD wax and CBD crystal samples could be refined to only those that have one unequal crystallographic angle (*i.e.* ; $\alpha=\gamma=90^\circ$, $\beta\neq 90^\circ$; or $\alpha=\beta=90^\circ$, $\gamma=120^\circ$). In conoscopic view, a biaxial interference figure indicated that the sample contained two optic axes and three principle refractive indices. Noting this, the possible crystal system was identified as one with three unequal crystallographic axes ($a\neq b\neq c$): orthorhombic, monoclinic, or triclinic. Taking the XPL characteristics into consideration, specifically extinction characteristics, the crystal system for the CBD dispensary samples was categorized as monoclinic.

The difference in crystal system (*i.e.* optical properties) between the crystals from the KCSD and Skymint subsets and the Cannabidiol Life CBD subset allows for rapid differentiation of the crystals formed in extracts derived from marijuana versus hemp. The readily observed optical differences between the marijuana-derived and hemp-derived solvent extract samples provides the opportunity for rapid screening of samples by PLM in forensic laboratories based on their crystalline component. While these samples can be optically differentiated, identification of the chemical composition using spectroscopic instrumentation is necessary to provide a comprehensive method by which to reliably distinguish the crystal component of marijuana and hemp extracts. The chemical characterization and identification of each subset of crystals is provided by **Chapter 3**.

APPENDIX

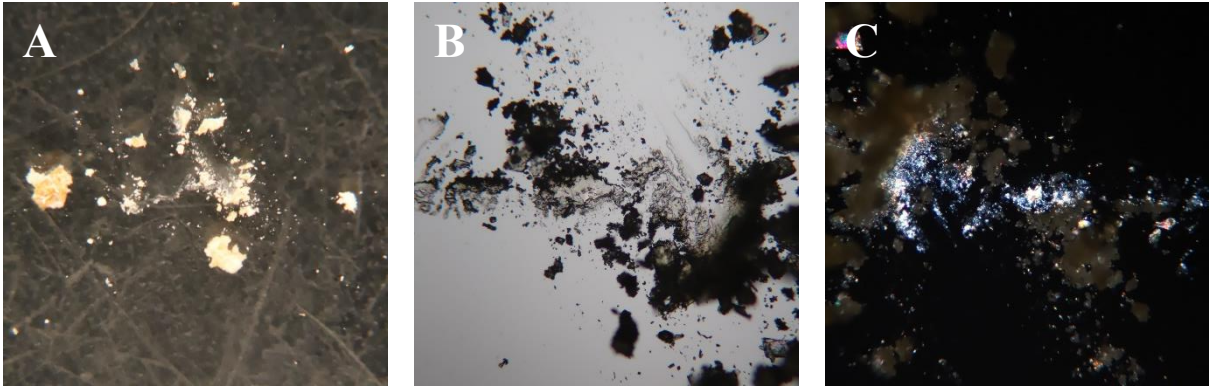


Figure A2.1 Macroscopic (A) and microscopic views of KCSD case sample PPO 14-20332-10 in PPL (B) and XPL (C)

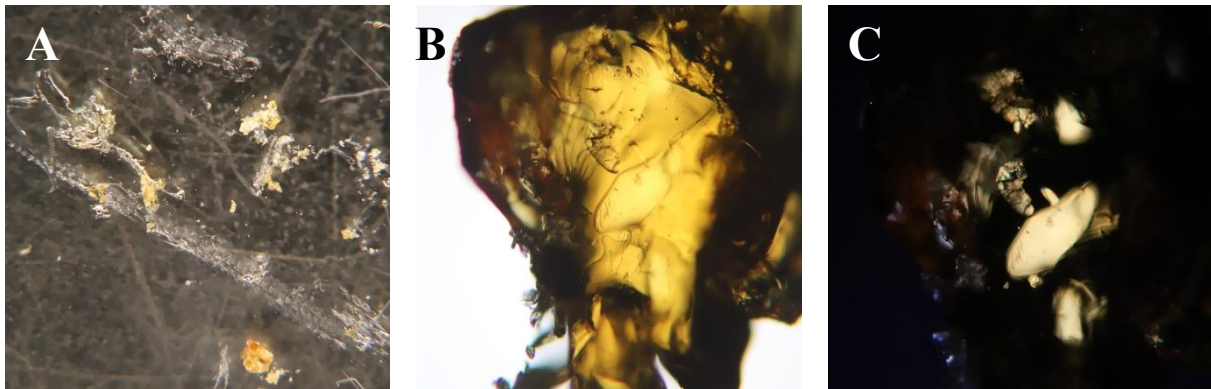


Figure A2.2 Macroscopic (A) and microscopic views of KCSD case sample KCSD 14-10811-28964 in PPL (B) and XPL (C)

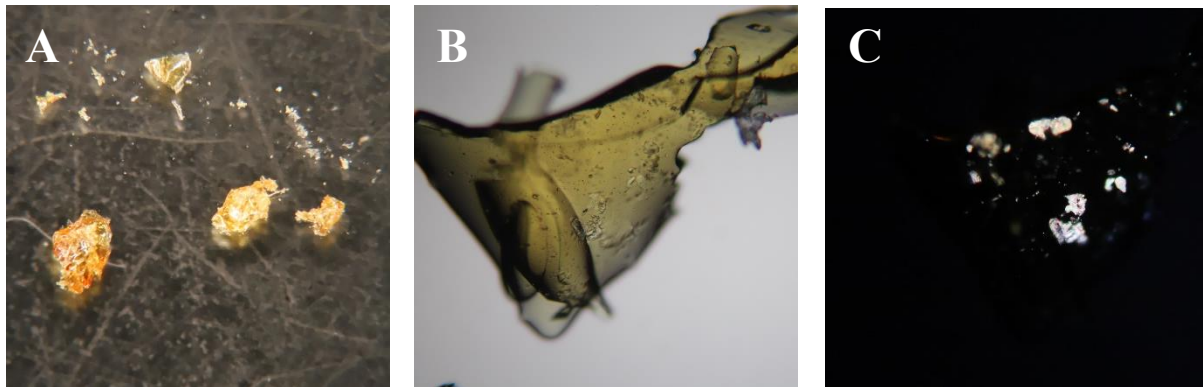


Figure A2.3 Macroscopic (A) and microscopic views of KCSD case sample KCSD 14-10811-28960 in PPL (B) and XPL (C)

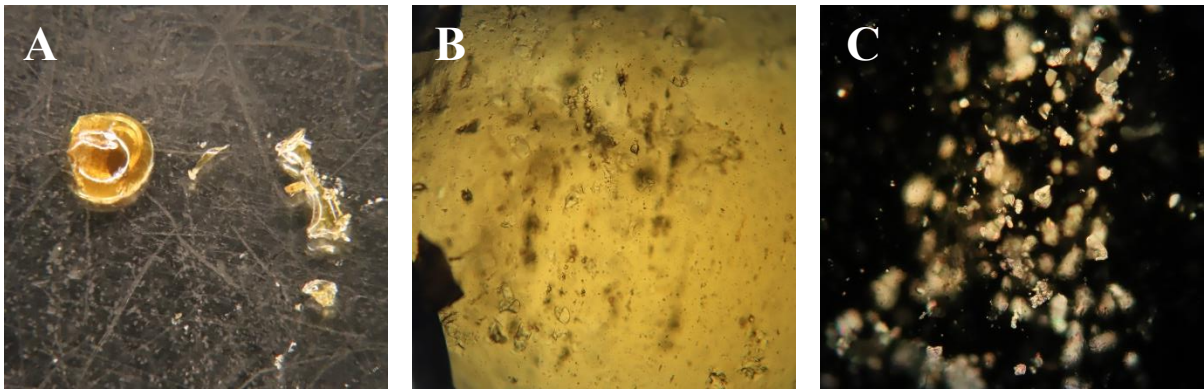


Figure A2.4 Macroscopic (A) and microscopic views of KCSD case sample KCSD 14-10811-28967 in PPL (B) and XPL (C)

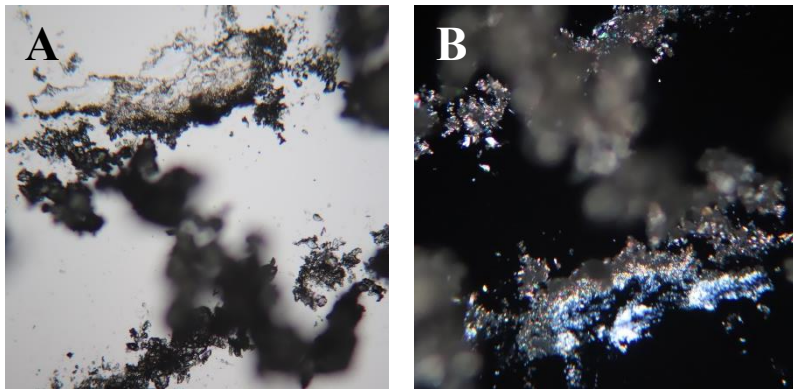


Figure A2.5 Microscopic views of Skymint dispensary sample WB THCA crystals in PPL (A) and XPL (B)

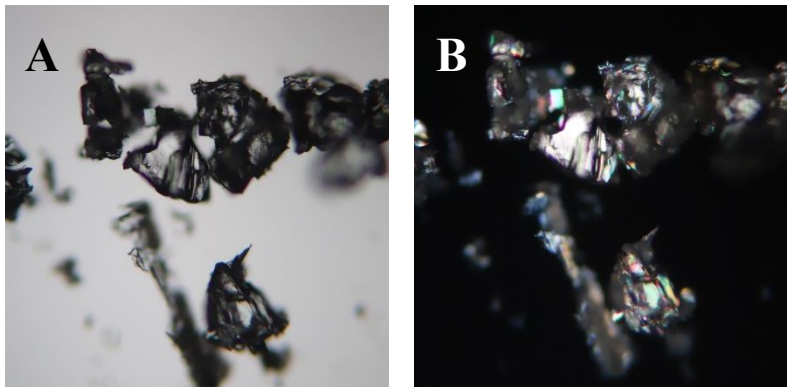


Figure A2.6 Microscopic views of Cannabidiol Life dispensary sample CBD crystals in PPL (A) and XPL (B).

Table A2.1 Table of refractive index measurements (n_α) for KDPS 18-9026

Crystal Number	Relative Refractive Index	Crystal Number	Relative Refractive Index
1	$n_\alpha < 1.520$	20	$n_\alpha \leq 1.5050$
2	$n_\alpha < 1.520$	21	$n_\alpha \leq 1.5050$
3	$n_\alpha < 1.520$	22	$n_\alpha \leq 1.5045$
4	$n_\alpha \leq 1.510$	23	$n_\alpha \geq 1.5045$
5	$n_\alpha \geq 1.510$	24	$n_\alpha \geq 1.5045$
6	$n_\alpha \geq 1.510$	25	$n_\alpha \geq 1.5045$
7	$n_\alpha \leq 1.510$	26	$n_\alpha \geq 1.5040$
8	$n_\alpha \leq 1.510$	27	$n_\alpha \geq 1.5040$
9	$n_\alpha > 1.5080$	28	$n_\alpha \geq 1.5040$
10	$n_\alpha < 1.5080$	29	$n_\alpha \geq 1.5040$
11	$n_\alpha < 1.5080$	30	$n_\alpha \leq 1.5040$
12	$n_\alpha < 1.5080$	31	$n_\alpha \leq 1.5040$
13	$n_\alpha < 1.5080$	32	$n_\alpha \leq 1.5040$
14	$n_\alpha < 1.5080$	33	$n_\alpha \leq 1.5000$
15	$n_\alpha \leq 1.5060$	34	$n_\alpha \leq 1.5000$
16	$n_\alpha \leq 1.5060$	35	$n_\alpha \leq 1.5000$
17	$n_\alpha \leq 1.5060$	36	$n_\alpha \geq 1.4920$
18	$n_\alpha \leq 1.5050$	37	$n_\alpha \geq 1.4920$
19	$n_\alpha \leq 1.5050$	38	$n_\alpha \geq 1.4920$

Table A2.2 Table of refractive index measurements (n_β) for KDPS 18-9026

Crystal Number	Relative Refractive Index	Crystal Number	Relative Refractive Index
1	$n_\beta < 1.6500$	15	$n_\beta \geq 1.6330$
2	$n_\beta < 1.6500$	16	$n_\beta \leq 1.6330$
3	$n_\beta < 1.6500$	17	$n_\beta \leq 1.6330$
4	$n_\beta < 1.6400$	18	$n_\beta \leq 1.6330$
5	$n_\beta < 1.6400$	19	$n_\beta \leq 1.6330$
6	$n_\beta < 1.6400$	20	$n_\beta \leq 1.6325$
7	$n_\beta \leq 1.6360$	21	$n_\beta \geq 1.6325$
8	$n_\beta \leq 1.6360$	22	$n_\beta \geq 1.6325$
9	$n_\beta \leq 1.6360$	23	$n_\beta \leq 1.6325$
10	$n_\beta \leq 1.6340$	24	$n_\beta \geq 1.6325$
11	$n_\beta \leq 1.6340$	25	$n_\beta \leq 1.6325$
12	$n_\beta < 1.6340$	26	$n_\beta \geq 1.6320$
13	$n_\beta \leq 1.6330$	27	$n_\beta \geq 1.6320$
14	$n_\beta > 1.6330$	28	$n_\beta \approx 1.6320$

Table A2.3 Table of refractive index measurements (n_γ) for KDPS 18-9026

Crystal Number	Relative Refractive Index	Crystal Number	Relative Refractive Index
1	$n_\gamma > 1.6400$	20	$n_\gamma \geq 1.6840$
2	$n_\gamma > 1.6400$	21	$n_\gamma \geq 1.6840$
3	$n_\gamma > 1.6400$	22	$n_\gamma \geq 1.6844$
4	$n_\gamma > 1.6500$	23	$n_\gamma \approx 1.6844$
5	$n_\gamma > 1.6500$	24	$n_\gamma \geq 1.6844$
6	$n_\gamma > 1.6500$	25	$n_\gamma \geq 1.6850$
7	$n_\gamma > 1.6600$	26	$n_\gamma \leq 1.6850$
8	$n_\gamma > 1.6600$	27	$n_\gamma \leq 1.6850$
9	$n_\gamma > 1.6600$	28	$n_\gamma \leq 1.6850$
10	$n_\gamma > 1.6700$	29	$n_\gamma \geq 1.6850$
11	$n_\gamma > 1.6700$	30	$n_\gamma \geq 1.6850$
12	$n_\gamma > 1.6700$	31	$n_\gamma \leq 1.6900$
13	$n_\gamma \geq 1.6800$	32	$n_\gamma \approx 1.6900$
14	$n_\gamma \geq 1.6800$	33	$n_\gamma \geq 1.6900$
15	$n_\gamma > 1.6800$	34	$n_\gamma \leq 1.6900$
16	$n_\gamma \geq 1.6833$	35	$n_\gamma \leq 1.6900$
17	$n_\gamma \geq 1.6833$	36	$n_\gamma < 1.7000$
18	$n_\gamma \geq 1.6833$	37	$n_\gamma < 1.7000$
19	$n_\gamma \geq 1.6840$	38	$n_\gamma < 1.7000$

Table A2.4 Table of refractive index measurements for PPO 14-20332-10

Crystal Number	Relative Refractive Index
1	$n_\alpha \leq 1.4960$
2	$n_\alpha \leq 1.4960$
3	$n_\alpha \leq 1.4960$
4	$n_\beta \geq 1.6320$
5	$n_\beta \geq 1.6320$
6	$n_\beta \geq 1.6320$
7	$n_\gamma \leq 1.6900$
8	$n_\gamma \leq 1.6900$
9	$n_\gamma \leq 1.6900$

Table A2.5 Table of refractive index measurements for KCSD 14-10811-28964

Crystal Number	Relative Refractive Index
1	$n_{\alpha} \geq 1.4960$
2	$n_{\alpha} \geq 1.4960$
3	$n_{\alpha} \geq 1.4960$
4	$n_{\beta} \geq 1.6320$
5	$n_{\beta} \geq 1.6320$
6	$n_{\beta} \geq 1.6320$
7	$n_{\gamma} \geq 1.6900$
8	$n_{\gamma} \geq 1.6900$
9	$n_{\gamma} \geq 1.6900$

Table A2.6 Table of refractive index measurements for KCSD 14-10811-28967

Crystal Number	Relative Refractive Index
1	$n_{\alpha} \leq 1.4960$
2	$n_{\alpha} \leq 1.4960$
3	$n_{\alpha} \leq 1.4960$
4	$n_{\beta} \geq 1.6320$
5	$n_{\beta} \geq 1.6320$
6	$n_{\beta} \geq 1.6320$
7	$n_{\gamma} \geq 1.6900$
8	$n_{\gamma} \geq 1.6900$
9	$n_{\gamma} \geq 1.6900$

Table A2.7 Table of refractive index measurements for KCSD 14-10811-28960

Crystal Number	Relative Refractive Index
1	$n_{\alpha} \geq 1.4960$
2	$n_{\alpha} \geq 1.4960$
3	$n_{\alpha} \geq 1.4960$
4	$n_{\beta} \geq 1.6320$
5	$n_{\beta} \geq 1.6320$
6	$n_{\beta} \geq 1.6320$
7	$n_{\gamma} \geq 1.6900$
8	$n_{\gamma} \geq 1.6900$
9	$n_{\gamma} \geq 1.6900$

Table A2.8 Table of refractive index measurements for WB THCA Crystals

Crystal Number	Relative Refractive Index	Crystal Number	Relative Refractive Index
1	$n_{\alpha} \leq 1.5040$	20	$n_{\beta} \leq 1.6320$
2	$n_{\alpha} \geq 1.5040$	21	$n_{\beta} \leq 1.6320$
3	$n_{\alpha} \leq 1.5040$	22	$n_{\beta} \geq 1.6320$
4	$n_{\alpha} \geq 1.5040$	23	$n_{\beta} \geq 1.6320$
5	$n_{\alpha} \leq 1.5040$	24	$n_{\beta} \leq 1.6320$
6	$n_{\alpha} \geq 1.5000$	25	$n_{\beta} \geq 1.6300$
7	$n_{\alpha} \geq 1.5000$	26	$n_{\beta} \geq 1.6300$
8	$n_{\alpha} \leq 1.5000$	27	$n_{\beta} \approx 1.6300$
9	$n_{\alpha} \leq 1.5000$	28	$n_{\gamma} > 1.6850$
10	$n_{\alpha} \geq 1.5000$	29	$n_{\gamma} > 1.6850$
11	$n_{\alpha} \leq 1.5000$	30	$n_{\gamma} > 1.6850$
12	$n_{\alpha} \leq 1.5000$	31	$n_{\gamma} > 1.6900$
13	$n_{\alpha} \geq 1.4960$	32	$n_{\gamma} > 1.6900$
14	$n_{\alpha} \leq 1.4960$	33	$n_{\gamma} > 1.6900$
15	$n_{\alpha} \leq 1.4960$	34	$n_{\gamma} \geq 1.7000$
16	$n_{\alpha} \leq 1.4960$	35	$n_{\gamma} \geq 1.7000$
17	$n_{\alpha} \geq 1.4920$	36	$n_{\gamma} \geq 1.7000$
18	$n_{\alpha} \geq 1.4920$		
19	$n_{\alpha} \geq 1.4920$		

Table A2.9 Table of refractive index measurements for PB THCA Wax

Crystal Number	Relative Refractive Index	Crystal Number	Relative Refractive Index
1	$n_{\alpha} \leq 1.5040$	13	$n_{\beta} \leq 1.6320$
2	$n_{\alpha} \leq 1.5040$	14	$n_{\beta} \leq 1.6320$
3	$n_{\alpha} \leq 1.5040$	15	$n_{\beta} \geq 1.6320$
4	$n_{\alpha} \geq 1.4960$	16	$n_{\beta} \geq 1.6320$
5	$n_{\alpha} \leq 1.4960$	17	$n_{\beta} \approx 1.6320$
6	$n_{\alpha} \leq 1.4960$	18	$n_{\beta} \geq 1.6300$
7	$n_{\alpha} \leq 1.4960$	19	$n_{\beta} \geq 1.6300$
8	$n_{\alpha} \geq 1.4960$	20	$n_{\beta} \geq 1.6300$
9	$n_{\alpha} \approx 1.4960$	21	$n_{\gamma} > 1.6900$
10	$n_{\alpha} \geq 1.4920$	22	$n_{\gamma} > 1.6900$
11	$n_{\alpha} \geq 1.4920$	23	$n_{\gamma} > 1.6900$
12	$n_{\alpha} \geq 1.4920$	24	$n_{\gamma} \geq 1.7000$
		25	$n_{\gamma} \geq 1.7000$
		26	$n_{\gamma} \geq 1.7000$

Table A2.10 Table of refractive index measurements for CBD Wax

Crystal Number	Relative Refractive Index	Crystal Number	Relative Refractive Index		
n_α	1	$n_\alpha \leq 1.5600$	n_β	19	$n_\beta \geq 1.5960$
	2	$n_\alpha \leq 1.5600$		20	$n_\beta \geq 1.5960$
	3	$n_\alpha \leq 1.5600$		21	$n_\beta \geq 1.5960$
	4	$n_\alpha \geq 1.5560$		22	$n_\beta \geq 1.6000$
	5	$n_\alpha \geq 1.5560$		23	$n_\beta \approx 1.6000$
	6	$n_\alpha \approx 1.5560$		24	$n_\beta \geq 1.6000$
	7	$n_\alpha > 1.5300$		25	$n_\beta \leq 1.6040$
	8	$n_\alpha > 1.5300$		26	$n_\beta \leq 1.6040$
	9	$n_\alpha > 1.5300$		27	$n_\beta \approx 1.6040$
n_β	10	$n_\beta > 1.5680$	28	$n_\beta \leq 1.6040$	
	11	$n_\beta > 1.5680$	n_γ	29	$n_\gamma \geq 1.6600$
	12	$n_\beta > 1.5680$		30	$n_\gamma \geq 1.6600$
	13	$n_\beta \geq 1.5800$		31	$n_\gamma \leq 1.6600$
	14	$n_\beta \geq 1.5800$		32	$n_\gamma \leq 1.6600$
	15	$n_\beta \geq 1.5800$		33	$n_\gamma \geq 1.6600$
	16	$n_\beta \geq 1.5900$		34	$n_\gamma \leq 1.6700$
	17	$n_\beta \geq 1.5900$		35	$n_\gamma \leq 1.6700$
	18	$n_\beta \geq 1.5900$		36	$n_\gamma \leq 1.6700$

Table A2.11 Table of refractive index measurements for CBD Crystal

Crystal Number	Relative Refractive Index	Crystal Number	Relative Refractive Index		
n_α	1	$n_\alpha \leq 1.5600$	n_β	13	$n_\gamma \geq 1.6600$
	2	$n_\alpha \leq 1.5600$		14	$n_\gamma \geq 1.6600$
	3	$n_\alpha \leq 1.5600$		15	$n_\gamma \leq 1.6600$
	4	$n_\alpha \geq 1.5560$		16	$n_\gamma \geq 1.6600$
	5	$n_\alpha \geq 1.5560$		17	$n_\gamma \leq 1.6700$
	6	$n_\alpha \approx 1.5560$		18	$n_\gamma \leq 1.6700$
n_β	7	$n_\beta \geq 1.6000$	19	$n_\gamma \leq 1.6700$	
	8	$n_\beta \geq 1.6000$			
	9	$n_\beta \geq 1.6000$			
	10	$n_\beta \leq 1.6040$			
	11	$n_\beta \approx 1.6040$			
	12	$n_\beta \leq 1.6040$			

REFERENCES

REFERENCES

- (1) Polowsky P, Tansman G, Kindstedt P, Hughes J. Characterization and identification of surface crystals on smear-ripened cheese by polarized light microscopy. *Journal of Dairy Science* 2018;101(9):7714–23.
- (2) Duncke ACP, Marinho TO, Barbato CN, Freitas GB, Oliveira MCKD, Nele M. Liquid Crystal Observations in Emulsion Fractions from Brazilian Crude Oils by Polarized Light Microscopy. *Energy & Fuels* 2016;30(5):3815–20.
- (3) Nie H, Xu W, Taylor LS, Marsac PJ, Byrn SR. Crystalline solid dispersion-a strategy to slowdown salt disproportionation in solid state formulations during storage and wet granulation. *International Journal of Pharmaceutics* 2017;517(1-2):203–15.
- (4) S. Stoeffler, "A Flowchart System for the Identification of Common Synthetic Fibers by Polarized Light Microscopy," *Journal of Forensic Sciences* 41, no. 2 (1996): 297-299
- (5) Bergfjord C, Holst B. A procedure for identifying textile bast fibres using microscopy: Flax, nettle/ramie, hemp and jute. *Ultramicroscopy* 2010;110(9):1192–7.
- (6) Reffner JA, Kamrath BW, Kaplan S. A More Efficient Method for Synthetic Textile Fiber Analysis Using Polarized Light Microscopy. *Journal of Forensic Sciences* 2019;65(3):744–50.
- (7) Brinsko KM, Golemis D, King MB, Laughlin GJ, Sparenga SB. U.S. Department of Justice, 2016; Available from: <https://www.ncjrs.gov/pdffiles1/nij/grants/249854.pdf>
- (8) Polarized Light Microscopy [Internet]. Nikon's MicroscopyU. Available from: <https://www.microscopyu.com/techniques/polarized-light/polarized-light-microscopy>
- (9) Nesse WD. Introduction to mineralogy. New York: Oxford Univ. Press, 2012;10. *The Essentials of Polarized Light Microscopy*
- (10) Delly JG. *Essentials of polarized light microscopy and ancillary techniques*. Westmont, IL: Hooke College of Applied Sciences, 2019;
- (11) Michel-Levy Birefringence Chart [Internet]. Specialized Microscopy Techniques - Michel-Levy Birefringence Chart | Olympus Life Science. Available from: <https://www.olympus-lifescience.com/en/microscope-resource/primer/techniques/polarized/michel/>
- (12) Pichler H., Schmitt-Riegraf C. (1997) Observations under conoscopic light. In: *Rock-forming Minerals in Thin Section*. Springer, Dordrecht. https://doi.org/10.1007/978-94-009-1443-8_3

3. SPECTROSCOPIC CHARACTERIZATION AND IDENTIFICATION OF CANNABIS SOLVENT EXTRACT COMPONENTS

Optical characterization, as discussed in **Chapter 2**, provides the ability to group and identify samples based on optical characteristics of known crystals. In order to identify the previously characterized crystalline components of each cannabis solvent extract, a variety of methods can be employed. The Scientific Working Group for the Analysis of Seized Drugs (SWGDRUG) provides recommendations for the analysis and identification of drug samples, including the cannabis extracts highlighted in this work. The methods by which forensic analysis and identification can be performed are categorized by SWGDRUG, ranking them from most to least discriminating. Based on these recommendations, one of the most commonly used, selective forensic analytical methods is spectroscopy, including Fourier-transform infrared (FTIR) spectroscopy and X-ray diffraction (XRD).

Forensic laboratories often utilize FTIR spectroscopy as a screening or identification technique to analyze submitted samples. As a SWGDRUG Category A method, FTIR spectroscopy can provide structural elucidation and identification, specifically for pure samples. The popularity of FTIR spectroscopy in forensic laboratories is due in part to the potential for non-destructive analysis, depending on the specific type of analysis performed as well as the tenacity of the sample. Additionally, such methods can provide quantitative and confirmatory results rapidly when compared to other common analytical methods.¹ Forensic analysis using FTIR spectroscopy commonly includes a variety of trace evidence not limited to fibers, paint chips, and adhesives.^{2,3} Further, FTIR spectroscopy has demonstrated suitability as both a quantitative and qualitative analytical method for seized drugs analysis, although pure samples are often necessary for identification.⁴⁻⁶ Moreover, the manufacturing and marketing of FTIR

spectrometers specifically for the identification and quantification of cannabinoids has increased recently, due to the necessity to provide cannabinoid profiles for on-site potency testing.⁷⁻⁹ The cannabinoids of interest for such on-site analyses include Δ^9 -tetrahydrocannabinol (Δ^9 -THC), tetrahydrocannabinolic acid (THCA), and cannabidiol (CBD).

An additional spectroscopic method recommended by SWGRUG as a Category A method for structural elucidation is XRD. Single-crystal XRD is an effective spectroscopic method through which the exact identity of an unknown can be determined. While FTIR analysis provides spectra to allow for interpretation and identification of functional groups within an organic compound, XRD provides the ability to identify the chemical formula, structure, and crystalline unit cell of any diffracting material. Moreover, XRD is an excellent identification technique as it allows for the identification of unknown samples without the necessity of a reference standard for comparison.¹⁰ Frequently, single-crystal XRD is used to establish the structure of protein crystals, for the purpose of visualizing the interaction between biochemical functions. However, small molecule crystal analysis has been performed, specifically with a forensic application for the characterization and differentiation of designer drugs.^{10,11}

3.1 INSTRUMENTAL THEORY

3.1.1 Micro-Attenuated Total Reflectance-Fourier Transform Infra-Red Spectroscopy

Due to the ease of sample preparation and analysis, attenuated total reflectance (ATR) - FTIR spectroscopy is commonly employed for IR analysis of forensic evidence. Attenuated total reflectance analysis is based on the interaction of internally reflected infrared light with a sample that is in close contact with an ATR crystal. This method can be both non-destructive and destructive, depending on the tenacity of the sample analyzed. In the case of this work, ATR-FTIR spectroscopy was a destructive analysis for the cannabis extract crystals. Standard ATR-FTIR analysis limits the size of samples compatible for analysis, as the entirety of the ATR crystal needs to be covered (~2mm in diameter) for the collection of representative spectra. While this lower size limit generally does not impact the routine analysis of common forensic trace evidence materials, it is not well-suited for the analysis of single crystal analysis. As such, the spectroscopic analysis of single crystals was performed using a micro-ATR-FTIR due to the ability to collect spectra for crystal samples as small as 10 μm .

While the instrumentation between standard ATR-FTIR and micro-ATR-FTIR differs, the general theory behind spectra collection and interpretation remains the same. Infrared light undergoes total internal reflectance between an optically dense ATR crystal and the sample that is pressed between the crystal and pressure anvil due to the difference in refractive index between the two materials.¹³ Moreover, at the point of interaction between the ATR crystal and sample, an evanescent wave of infrared light extends past the ATR crystal, interacts with the sample material, and is absorbed resulting in attenuated total reflection.¹³

The penetration of the evanescent wave into the sample media is dictated by the wavelength of light, the angle of incidence between the ATR crystal and sample material, and

the indices of refraction for the ATR crystal and sample material.¹⁴ Specifically, penetration depth is inversely related to wavelength, such that penetration is greater at lower wavelengths than higher wavelengths. In general, the depth of penetration for most samples measured by ATR is 1-2 μm . Due to the effect of wavelength on sample penetration, and the fact that an IR light source contains a range of wavelengths, the resulting FTIR spectra produced through ATR-FTIR differs from the standard absorbance spectra measured via transmission of light.¹⁴ Most notably, ATR-FTIR spectra emphasize the “fingerprint region” (smaller wavenumbers) while reducing the absorbance bands at higher wavenumbers. Due to the difference between the spectra obtained by ATR-FTIR and transmission FTIR, it is ideal for spectral comparisons to occur between reference and sample spectra obtained on the same instrument. When reference materials are not readily available for comparison, a library sample collected using ATR-FTIR rather than transmission FTIR can provide a method for presumptive identification.

The instrumental set-up for micro-ATR-FTIR utilizes a spectrometer and IR light source attached to a fully operational polarized light microscope. **Figure 3.1** illustrates this instrumental setup. For analysis by micro-ATR-FTIR, the sample of interest is mounted on a standard microscope slide and can be observed in plane-polarized light and crossed-polarized light as with a standard polarized light microscope. An ATR diamond crystal objective lens is used to make contact, essentially crushing the crystal sample, in order to produce total internal reflection and the evanescent wave. Additionally, micro-ATR-FTIR fitted microscopes include spectrometers with infrared light sources, interferometer, directing optics, and a detector. **Figure 3.2** provides a simplified scheme of an ATR objective and spectrometer.

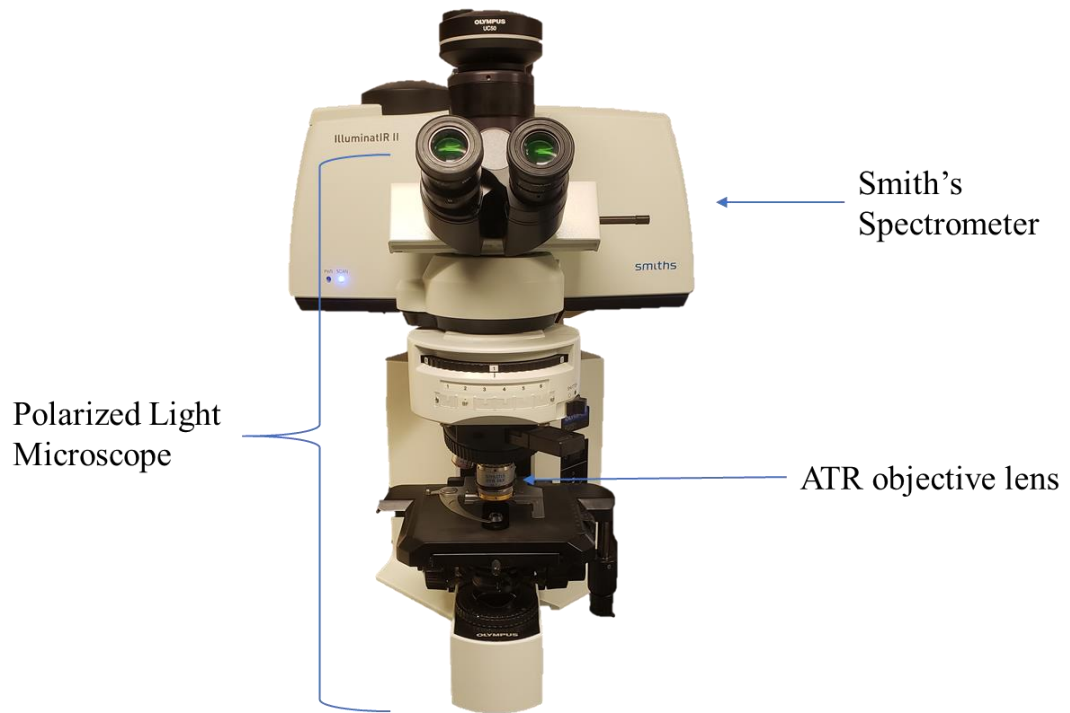


Figure 3.1 Smith's IlluminatIR II Micro-ATR-FTIR instrumental set-up

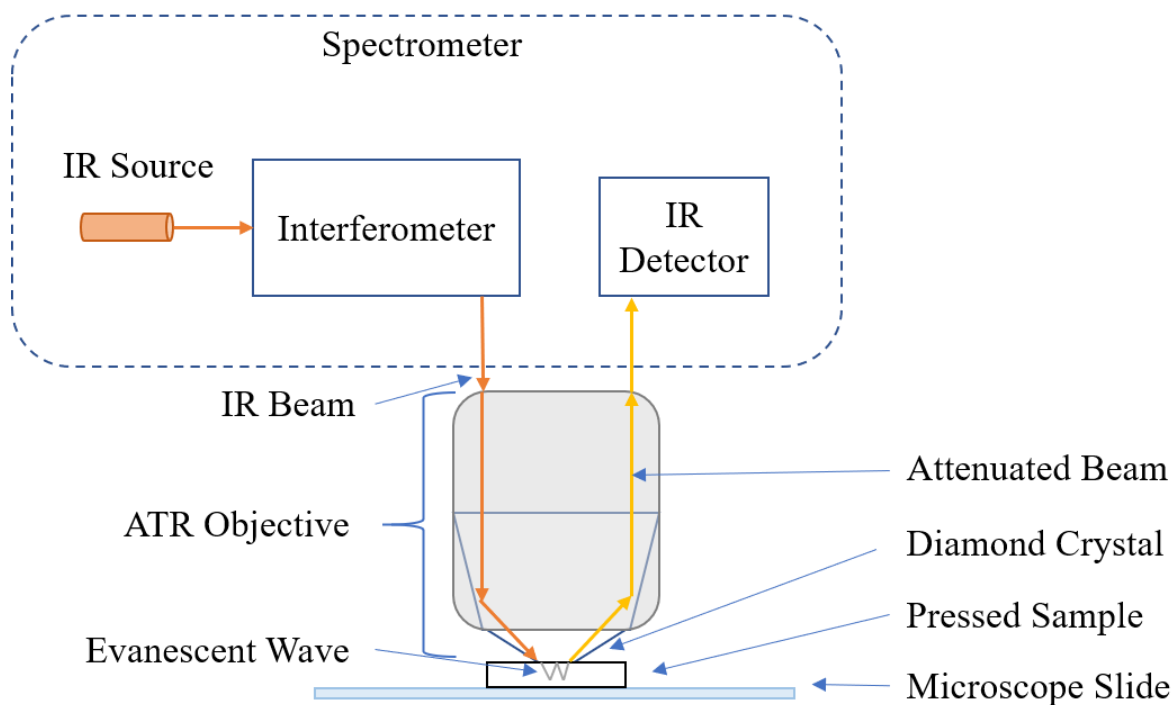


Figure 3.2 Simplified schematic of an ATR microscope objective and infrared spectrometer commonly used for microscopic infrared analysis

3.1.2 X-Ray Diffraction Theory and Instrumentation

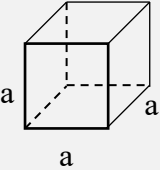
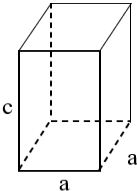
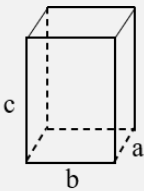
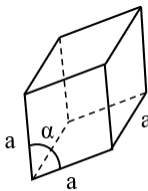
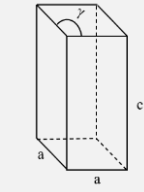
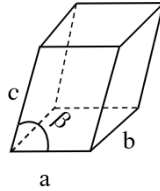
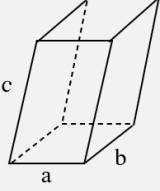
Single-crystal XRD is a powerful analytical technique through which an unknown sample can be characterized and identified. This technique utilizes X-ray radiation as an excitation source to aid in the determination of a crystalline unit cell. Further, to define the crystal structure, X-ray diffraction patterns for a unique crystal are solved, providing electron density maps which indicate the likely atom placement.

The fundamental concepts related to the determination of the crystalline unit cell and chemical formula include crystal structure, light and X-ray diffraction. Single-crystal XRD is a form of crystallography which refers to the study of the properties, structure, and formation of crystals. Crystal structure is categorized using Bravais lattices, which represents the most basic

building block of the crystal.¹⁵ The Bravais lattices are a collection of 14 different groups of points, which can be further categorized into seven crystal systems. Crystal systems were first introduced in **Chapter 2**, with their relation to optical properties of a crystal. Nonetheless, a more in-depth explanation of crystal systems is necessary in its application to X-ray diffraction.

The seven crystal systems are differentiated by the relationship between atomic spacing and angles in the unit cell. **Table 3.1** outlines the crystal systems and provides accompanying geometric summaries of each unit cell. The unit cell is the smallest group of atoms that, when repeated, produce the lattice of a crystal system.¹⁵ The length between two points on the corners of the lattice, or crystallographic axis, is denoted by a, b, or c, while the angle between the crystallographic axes is given by α , β , and γ . The unit cells increase in complexity and decrease in symmetry from cubic, in which all three crystallographic lengths and angles are equal, to triclinic, in which there are no equal lengths or angles.

Table 3.1 Summary of crystal systems with geometric unit cell depictions

Crystal System	Crystallographic Lengths and Angles	Unit Cell Depiction
Cubic	$a = b = c,$ $\alpha = \beta = \gamma = 90^\circ$	
Tetragonal	$a = b \neq c,$ $\alpha = \beta = \gamma = 90^\circ$	
Orthorhombic	$a \neq b \neq c,$ $\alpha = \beta = \gamma = 90^\circ$	
Rhombohedral	$a = b = c,$ $\alpha = \beta = \gamma \neq 90^\circ$	
Hexagonal	$a = b \neq c,$ $\alpha = \beta = 90^\circ, \gamma = 120^\circ$	
Monoclinic	$a \neq b \neq c,$ $\alpha = \gamma = 90^\circ, \beta \neq 90^\circ$	
Triclinic	$a \neq b \neq c,$ $\alpha \neq \beta \neq \gamma$	

The cubic lattice is the simplest and most symmetrical of all crystal systems with all angles equal to 90° and all axes equal in length. The Bravais lattices associated with the cubic crystal system are the primitive cubic, body-centered, and face-centered cubic. The body-centered cubic Bravais lattice includes an atom in the center of the cube as well as atoms positioned in the corners of the cubic structure (at the location of the primitive cubic vertices). The face-centered cubic includes atoms at the locations of the primitive cubic lattice as well as atoms in the center of each cube's face. An additional form of Bravais lattice is the base-centered lattice, which includes atoms in each primitive vertex and atoms positioned on two opposing faces, generally perpendicular to the c axis of the unit cell.¹⁵ Base-centered Bravais lattices are not part of the cubic system, but rather the orthorhombic and monoclinic crystal systems. Figures of the geometric symmetry of crystals by the Bravais lattices are provided in Appendix III.

To determine the crystal system and Bravais lattice of a crystal, X-ray diffraction is often employed. Diffraction occurs based on the interaction of monochromatic light with a regular, repeating material. The periodicity of the material increases the magnitude of the diffraction due to constructive interference of the diffracted light rays. The constructive interference occurs as diffracted light rays combine their amplitudes, resulting in a point of diffraction with an intensity proportional to the square of the light's amplitude.¹⁶ The regularly repeating lattice structures of crystals interact with light similarly, producing a diffraction pattern related to the spacing of atoms in the lattice. In order to produce diffraction on the atomic scale, X-rays are necessary as their wavelengths are on the same scale as the distance between atoms. The interaction between the crystal lattice and X-ray beam is dictated by Bragg's law, which states that constructive interference can only occur when **Equation 3.1** is satisfied.¹⁶ In this equation, n is an integer, λ

is the X-ray wavelength, d is the distance between lattice parallel planes, and θ is the angle of incidence. **Figure 3.3** demonstrates this relationship.

$$n\lambda = 2d \sin\theta \quad \text{Equation 3.1}$$

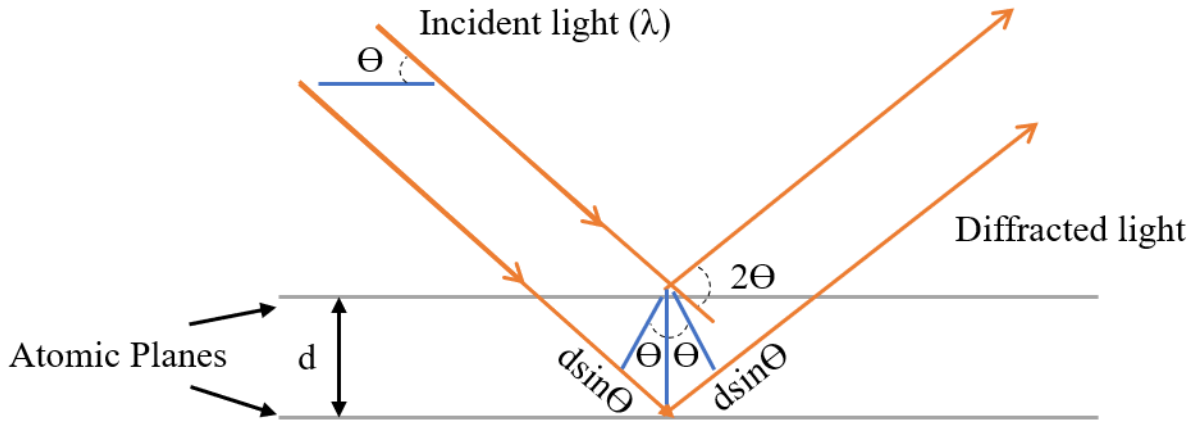


Figure 3.3 Illustration for the requirements of Bragg's Law¹⁶

In order to completely characterize a crystal lattice using diffraction, the diffraction patterns need to be obtained in many different angles and orientations around the crystal. This is due to the three-dimensional periodicity of crystals, which produce many different diffracting planes in orientations based on the crystal's symmetry group.¹⁶ The collection of diffraction patterns at different angles and orientations about the crystal produces a "reciprocal lattice." The reciprocal lattice includes information regarding the Fourier transform of the spatial wavefunction of the original lattice.¹⁶ It is important to denote the difference between the original lattice in "real space" and the reciprocal lattice in "reciprocal space." Real space includes the physical crystal, atoms, and lattice. Reciprocal space is the Fourier transform of real

space, resulting from the diffraction pattern of all possible crystal orientations. By collecting diffraction patterns from all possible crystal orientations, a three-dimensional reciprocal lattice can be constructed, thus allowing the real crystal lattice to be solved by performing a Fourier transform.

Solving the crystal structure by XRD requires the recombination of the diffracted beams with the correct amplitudes and relative wave phases.¹⁷ This recombination provides a map of the electron densities of a given plane of the crystal lattice, representing the positioning of atoms in the unit cell. Each diffraction spot (or reflection) includes a different intensity related to the surrounding spacing of electron density features in each unit cell.¹⁸ The recombination is performed via Fourier transformation, where the amplitude and phase of each diffracted X-ray wavelength act as Fourier coefficients and can be added together by Fourier synthesis to obtain the original periodic function (*i.e.*, electron density) represented by the diffraction pattern.¹⁷

In a diffraction experiment, however, only the amplitude of the diffracted beam is known, not the phases. This gives rise to the “phase problem” in crystallography. For small molecules (less than 20 atoms), solving the phase problem is unnecessary, as the amplitude of a diffracted spot generally provides enough insight related to possible structural features. Rather than solving the phase problem in these small molecules, the Patterson function can be employed, which provides a map of peaks at every interatomic vector position in the structure. However, this function is only useful for small molecules as the number of interatomic vectors increases with N atoms, such that the function will contain $N(N-1)$ vectors, with many overlapped.¹⁸ Additionally, small and intermediate sized crystals can be solved using direct methods, which provide a mathematical method through which phases are chosen for strong reflections based on knowledge of the possible molecule. The phases for other reflections are then generated based on

known interaction relationships between strong reflections and an electron density map is constructed to determine atomic positioning.¹⁸ Structural refinement following the determination of a rough electron density map is performed given the ability to apply chemical knowledge to a structure, improving the electron density and phases together.

3.2 MATERIALS AND METHODS

3.2.1 Samples

The same nine cannabis extract samples introduced and optically characterized in **Chapter 2** were further chemically characterized *via* micro-ATR-FTIR and single-crystal XRD. **Table 3.2** summarizes the source, identity, and age of the samples.

Table 3.2 Sample identifications, sources, and year obtained

Sample Identity	Source	Year Obtained
KDPS 18-9026	KCSD	2018
PPO 14-20332- 10	KCSD	2014
KCSD 14-10811 - 28964	KCSD	2014
KCSD 14-10811 - 28967	KCSD	2014
KCSD 14-10811 - 28960	KCSD	2014
“Punch Breath” Sugar/Wax	Skymint	2020
“Wonka Bars 13” THCA crystals	Skymint	2020
CBD Shatter Crystals	Cannabidiol Life	2020
CBD Crumble/Wax	Cannabidiol Life	2020

3.2.2 Micro-Attenuated Total Reflectance-Fourier Transform Infra-Red Spectroscopy – Sample Preparation

Characteristic crystals from each case sample were selected for micro-ATR-FTIR. Each sample crystal was cleaved from a larger crystal such that both PLM characterization and spectroscopic analysis were performed on equivalent crystals. Micro-ATR-FTIR analysis was performed using an Olympus BX51 PLM (Olympus Corporations of America, Center Valley, PA) with Smith's IlluminatIR II spectrometer and micro-ATR objective (Smiths Detection, Edgewood, MD).

Prior to crystal analysis, the FTIR center burst was aligned and the strength of the center burst peak was verified to be ~14,500 units. Additionally, between each sample analysis, instrument background scans were collected with the micro-ATR objective placed over, but not in contact with, the sample. Triplicate spectra were collected for each case sample. Instrument parameters for analysis were as follows: resolution of 4 cm^{-1} , 20-100 μm aperture (depending on crystal size), and 16 scans collected. Samples were crushed using the micro-ATR objective until the entirety of the aperture was covered by the crushed crystal sample, but without pressing so hard that interference from the supporting glass microscope slide overwhelmed the sample spectrum. Sample spectra were characterized based on functional group frequencies tabulated by Pretsch *et al.*¹⁹ and compared to THC and THCA certified reference materials (all Cayman Chemical Co, Ann Arbor, MI) for preliminary identification.

3.2.3 Single-Crystal X-Ray Diffraction – Sample Preparation

Single crystals from case sample KDPS 18-9026, Skymint THCA crystal sample, and Cannabidiol Life CBD crystal sample were selected for crystallographic identification via single-crystal XRD. The individual crystals were mounted on a nylon loop using paratone oil. Single-crystal XRD for case sample KDPS 18-9026 was performed using a Bruker APEX-II CCD diffractometer (Bruker Analytical X-ray Systems, Madison, WI) at a low temperature $T = 173$ K with an Oxford Cryosystems low-temperature device (Oxford Cryosystems Ltd., Long Hanborough, Oxford, UK). In the time between the analysis of the KDPS case sample and the dispensary samples, a new single-crystal XRD was purchased by the Center for Crystallographic Research at Michigan State University. As such, analyses for the Skymint THCA crystal and Cannabidiol Life CBD crystals were performed using a XtaLAB Synergy, Dualflex, HyPix diffractometer (Rigaku Americas Corporation, The Woodlands, TX) at a low temperature $T=100.01(10)$ K with an Oxford Cryosystems low-temperature device (Oxford Cryosystems Ltd.). For all crystal analyses, X-ray intensity data were collected using $\text{CuK}\alpha$ radiation. Lorentz polarization was corrected for the KDPS 18-9026 sample using the SAINT software (Bruker Analytical X-ray Systems, V8.38A, after 2013, Madison, WI), while the dispensary samples polarization was corrected using CrysAlisPro software (Agilent Technologies, XRD Products Oxfordshire, UK). For all crystals, the absorption correction was performed in the Θ SADABS-2016/2 software (Bruker Analytical X-ray Systems V2.008/2 2016/2, Madison, WI). The crystal structure was solved using dual methods using ShelXT (Sheldrick, G.M. (2015). *Acta Cryst.* A71,3-8). Refinement of the structure was performed using an Olex2 incorporated form of Least Squares (developed based on research by Dolomanov *et al.*²⁰) using version 2014/6 of XL (as developed by Sheldrick²¹). All non-hydrogen atoms were refined anisotropically. Hydrogen atom

positions were calculated geometrically using the riding model. This excludes hydrogen atoms on non-carbon atoms which were found by difference Fourier methods and refined isotropically. Crystal dimensions for the KDPS 18-9026 case sample crystals were $0.18 \times 0.07 \times 0.06 \text{ mm}^3$. Crystal dimensions for the Skymint PB THCA Crystals sample were $0.12 \times 0.07 \times 0.03 \text{ mm}^3$. Crystals dimensions for the Cannabidiol Life CBD Crystals sample were $0.33 \times 0.22 \times 0.15 \text{ mm}^3$.

3.3 FTIR SPECTROSCOPIC ANALYSIS OF CANNABIS SOLVENT EXTRACTS

3.3.1 Results of Micro-ATR-FTIR Analysis of Cannabis Solvent Extracts

3.3.1.1 Micro-ATR-FTIR Analysis of Optically Similar Crystals - KCSD Case Samples and Skymint Samples

Due to the similarities in optical properties between the KCSD BHO case samples and the Skymint BHO crystal and wax dispensary samples outlined in **Chapter 2**, it was assumed that the crystalline components of these samples shared chemical characteristics. While each of the seven samples between these two groups was characterized by micro-ATR-FTIR, one sample from each subset was selected to represent each group. Case sample KDPS 18-9026 was selected to represent the KCSD case samples, while the Skymint WB THCA Crystal sample represents the Skymint dispensary samples. Additionally, when present, the wax components of each BHO sample were also analyzed by micro-ATR-FTIR to determine any chemical similarities between waxes with varying textures. The KCSD and Skymint samples and wax textures are summarized in **Table 3.3**.

Table 3.3 KCSD and Skymint sample summary

Sample Source	Sample Identity	Sample Consistency
KCSD Case Samples	KDPS 18-9026	Wax (Crumble)
	PPO 14-20332-10	Wax (Soft /Viscous)
	KCSD 14-10811-28964	Wax (Soft to Glass-like)
	KCSD 14-10811-28967	Wax/Shatter (Solid, hard; Glass-like)
	KCSD 14-10811-28960	Wax (Soft to Glass-like)
Skymint Dispensary Samples	PB THCA Wax	Crystalline (Little Oily/Wax Matrix)
	WB THCA Crystals	Crystalline Material (No Wax Material)

Crystalline and wax components (when present) of each sample were analyzed by micro-ATR-FTIR and compared to a THCA certified reference material. A representative spectrum of case sample BHO crystal and wax components is provided by KDPS 18-9026 (**Figure 3.4**) while a representative spectrum of the Skymint dispensary samples is provided by WB THCA Crystals (**Figure 3.5**). These spectra display a rising baseline in the fingerprint region most likely caused by interference due to the glass microscope slide on which the crystal was mounted for analysis. The stretching frequency for the Si-O bond in glass is located from $\sim 1200 - \sim 800 \text{ cm}^{-1}$ and produces a very strong, broad peak. The size constraints of the crystals following cleavage ($\sim 25\text{-}50 \mu\text{m}$) allows for portions of the micro-ATR crystal to contact the supporting glass slide, rather than be entirely covered by the crushed crystalline sample. **Figure 3.6** provides an overlay of normalized FTIR spectrum of all optically similar crystalline samples for visual comparison, while **Figure 3.7** provides the normalized FTIR spectra for the wax component of each BHO

case sample. The separate representative spectra of the additional samples are included in Appendix III.

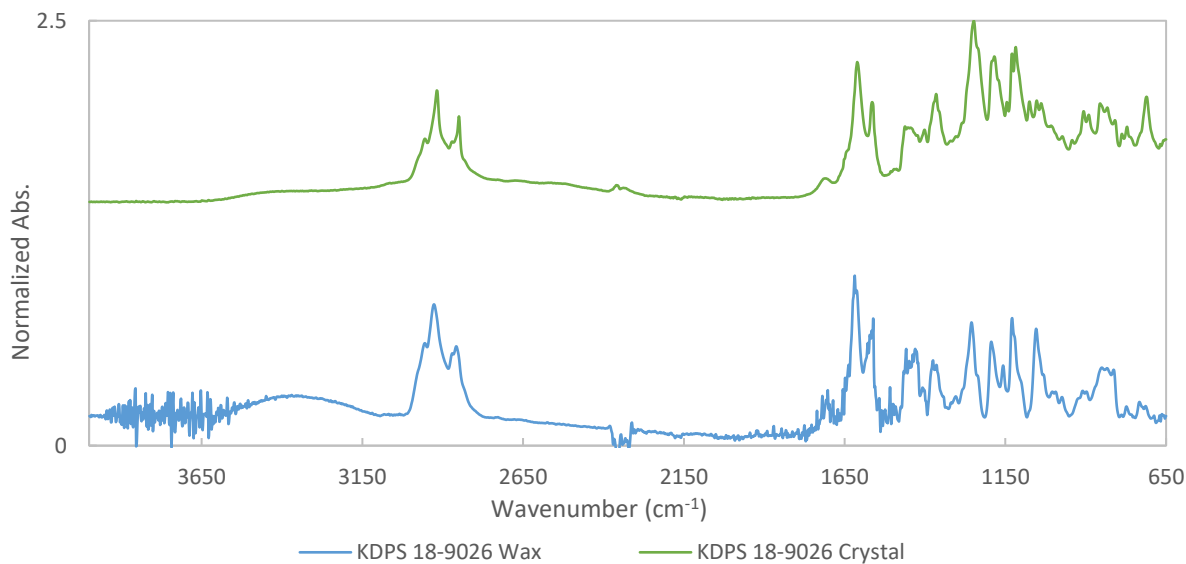


Figure 3.4 KDPS 18-9026 crystal (top) and wax component (bottom) IR spectrum

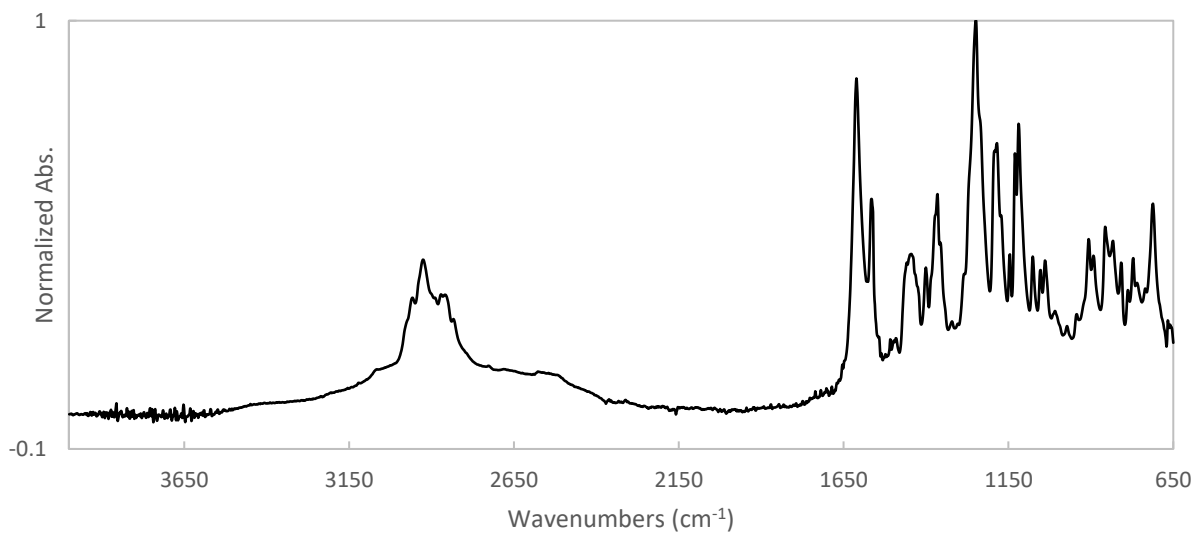


Figure 3.5 Representative Skymint sample - WB THCA Crystal IR spectrum

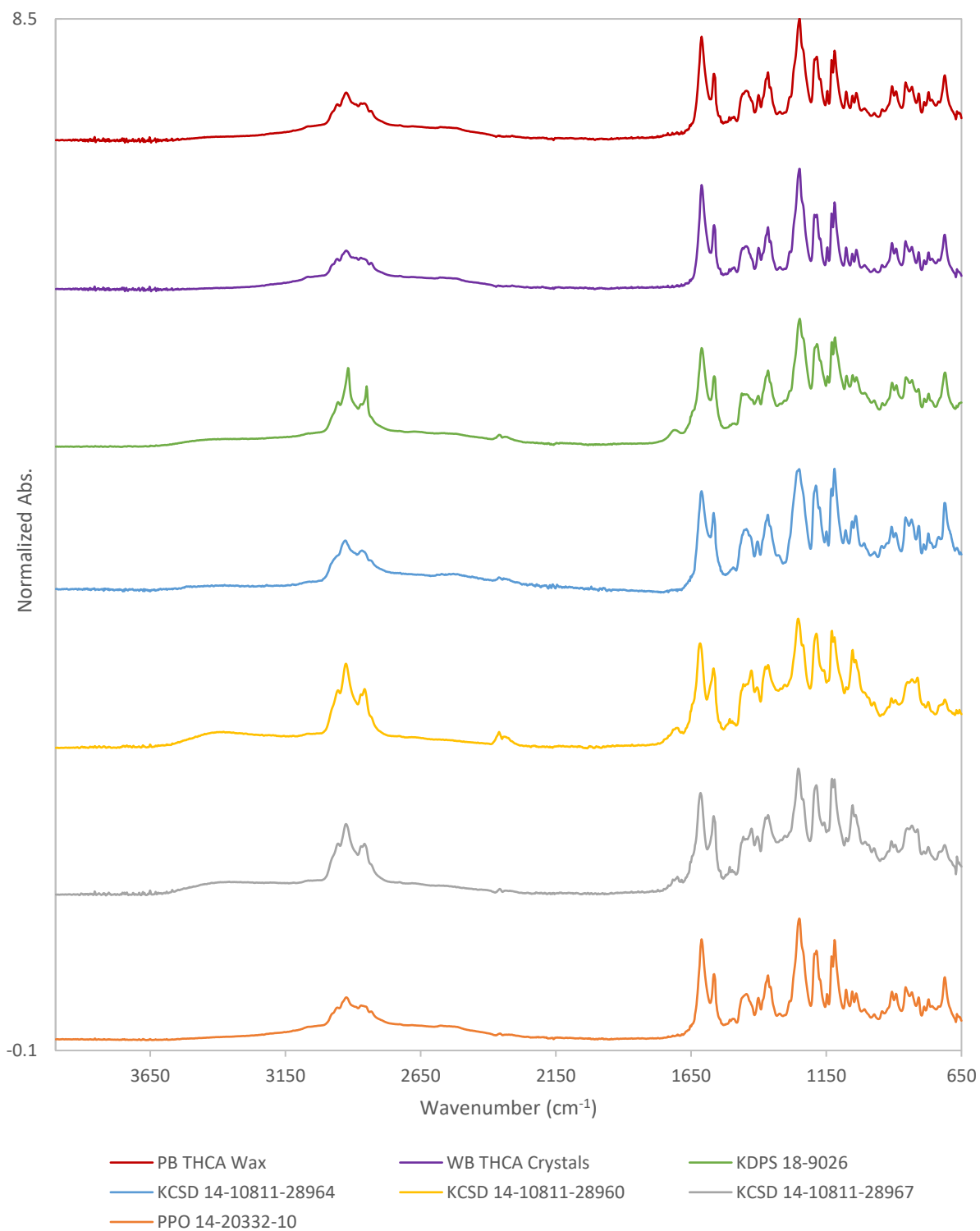


Figure 3.6 Stacked FTIR spectra for all sample crystalline components

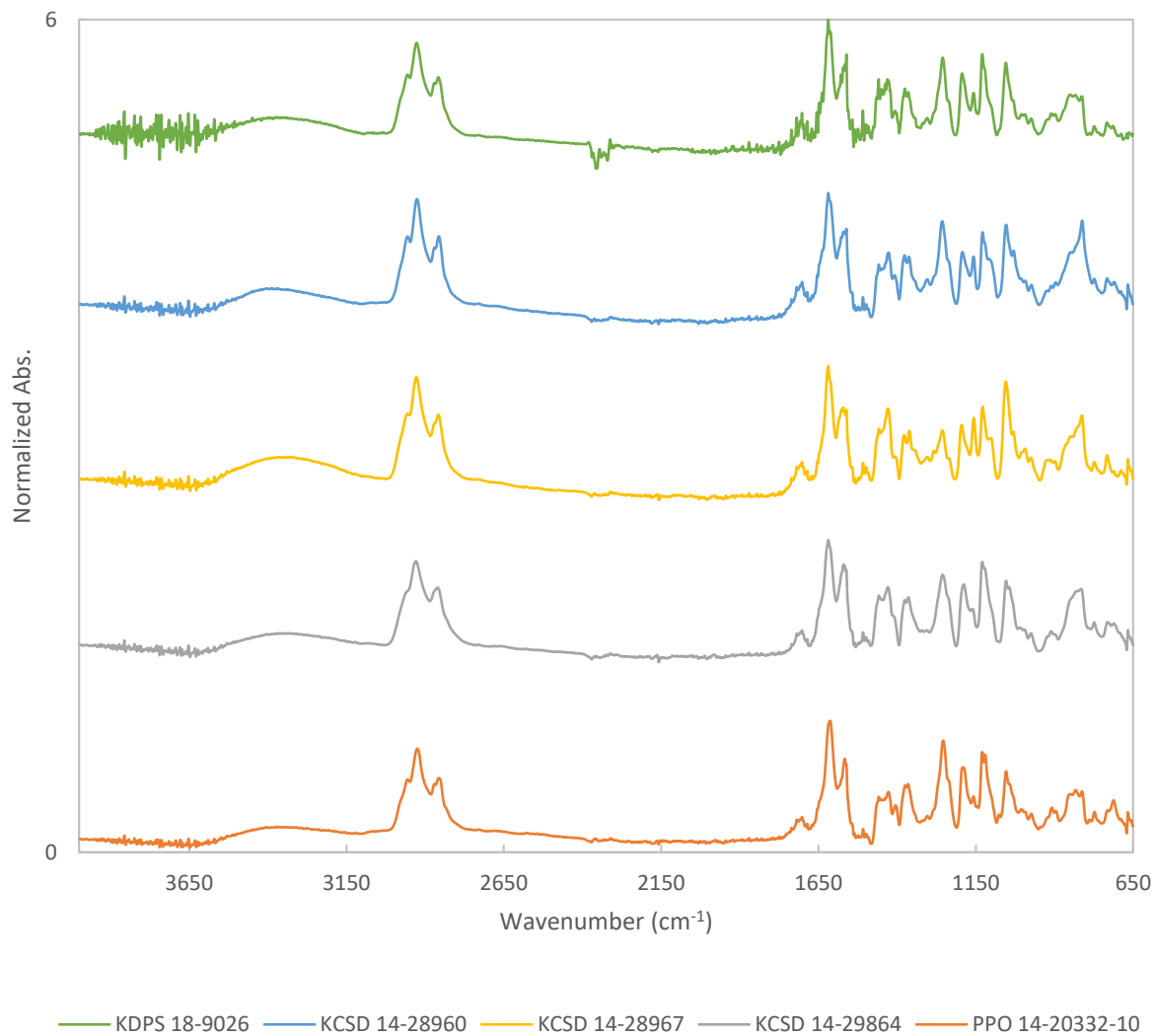


Figure 3.7 Stacked FTIR spectra for all case sample wax components

To presumptively identify the crystalline and wax components of the BHO case samples, a representative spectrum from each sample was first subjected to a standard library search and compared to the top matches. The most comparable match for each sample crystalline components was a nujol mull preparation of THCA. Comparatively, the top result for the wax component differed between nujol mull preparations of THCA and independent library spectra of

THC samples. Following the preliminary library identification, the case sample spectra were compared to the FTIR spectra of THCA and THC collected using micro-ATR-FTIR (**Figure 3.8** and **Figure 3.9**).

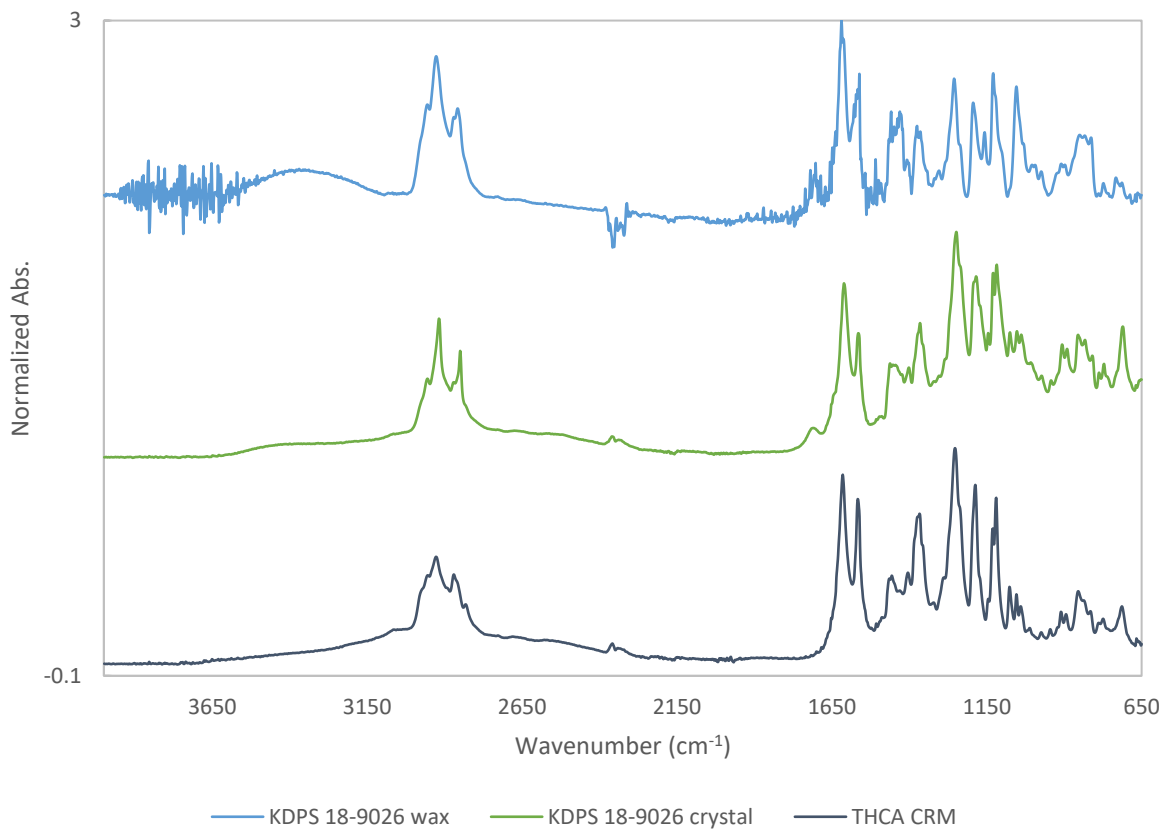


Figure 3.8 Stacked comparison of THCA CRM (bottom) and case sample KDPS 18-9026 crystal (middle) and wax component (top) micro-ATR-FTIR spectra

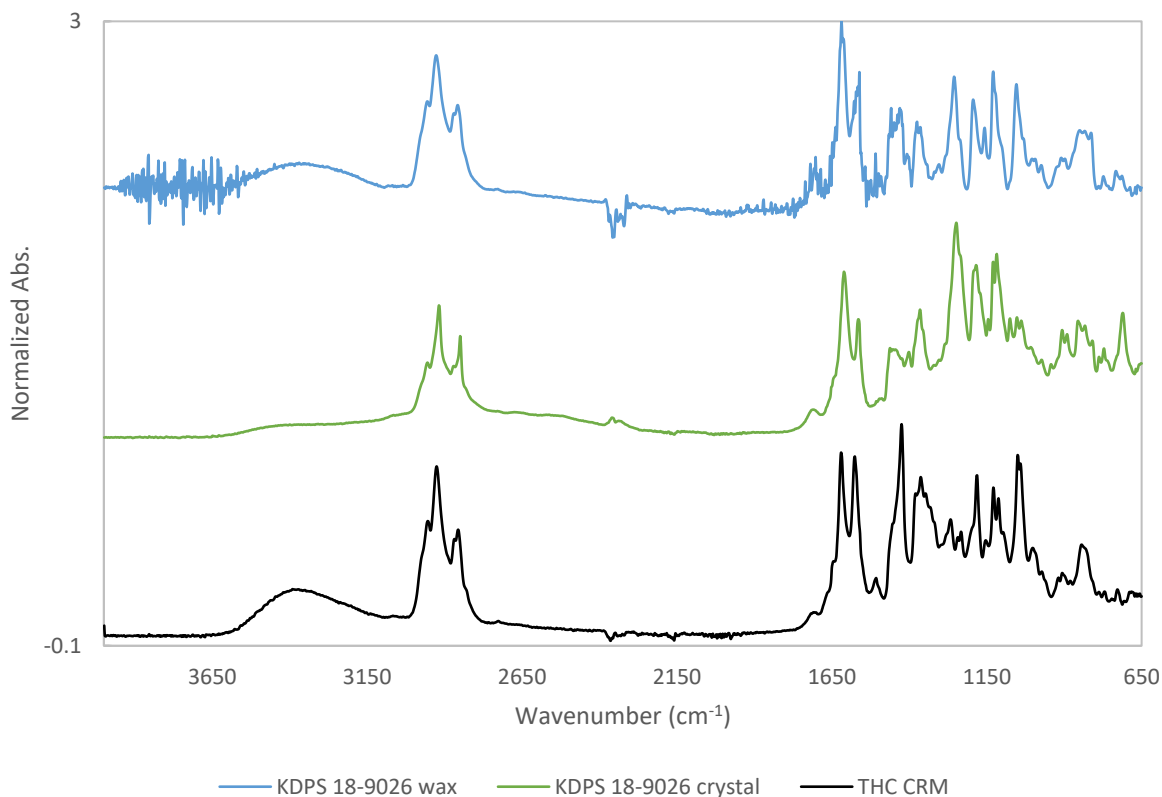


Figure 3.9 Stacked comparison of THC CRM (bottom) and case sample KDPS 18-9026 crystal (middle) and wax component (top) micro-ATR-FTIR spectra

3.3.1.2 Micro-ATR-FTIR Analysis of Cannabidiol Life Dispensary Samples

Based on the optical properties discussed in **Chapter 2**, the Cannabidiol Life dispensary samples contained optically different crystal components compared to the KCSD case samples or Skymint subsets. As such, micro-ATR-FTIR analysis was performed to determine the chemical composition of the crystals for further comparison and differentiation. **Table 3.4** provides a summary of the sample identity and consistency. It should be noted that each sample included terpene blueberry flavoring, which differs from the KCSD case samples or Skymint dispensary

samples. Additionally, the wax matrix observed in the CBD Wax sample was oily, as opposed to viscous or sticky.

Table 3.4. Cannabidiol Life CBD-containing sample summary

Sample Identity	Sample Consistency
CBD Wax	Mostly Crystalline Wax (Oily/Wax matrix)
CBD Shatter Crystals	Crystalline Material (No Wax Matrix)

Crystalline components of each sample were analyzed by micro-ATR-FTIR and compared to library search results and THCA certified reference material. **Figure 3.10** provides a spectrum for the Cannabidiol Life CBD Wax sample (both crystalline and oily residue), while **Figure 3.11** displays a spectrum for the CBD Shatter Crystals sample. The noise present in the CBD wax sample's wax component (oil residue) spectrum is likely due to the size of the sample used for analysis. The lack of residue around the crystals resulted in an overall lack of sample for ATR-FTIR analysis, leading to a lower quality spectrum collected.

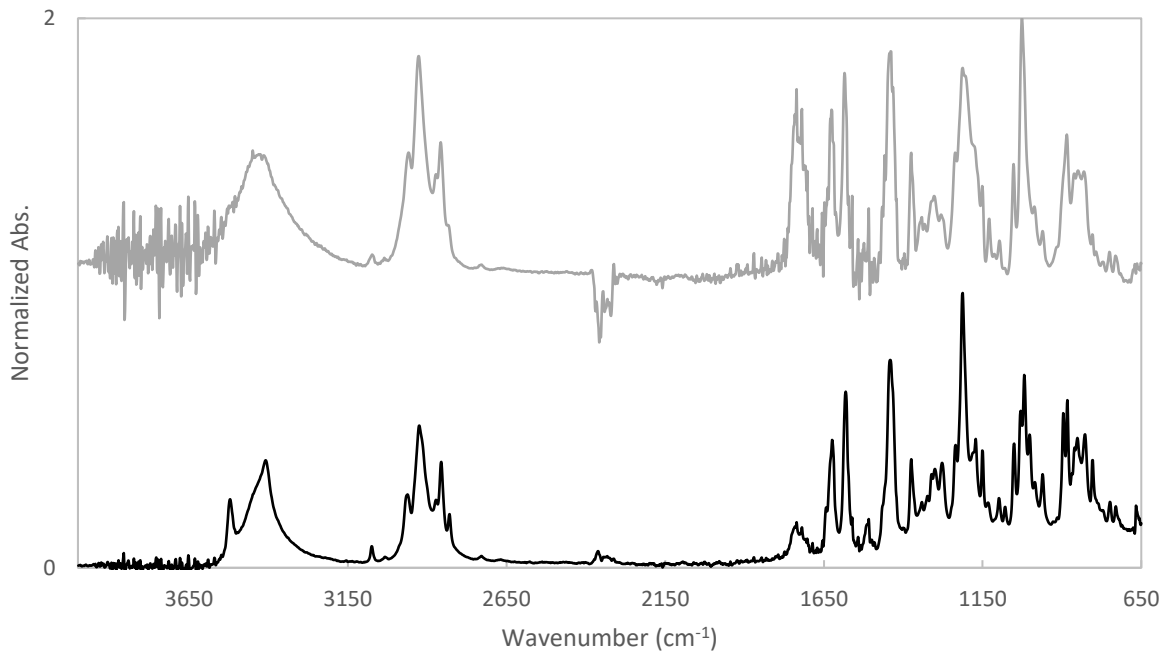


Figure 3.10 Micro-ATR-FTIR spectrum for the crystalline component of sample CBD Wax crystal (bottom) and wax (top) components

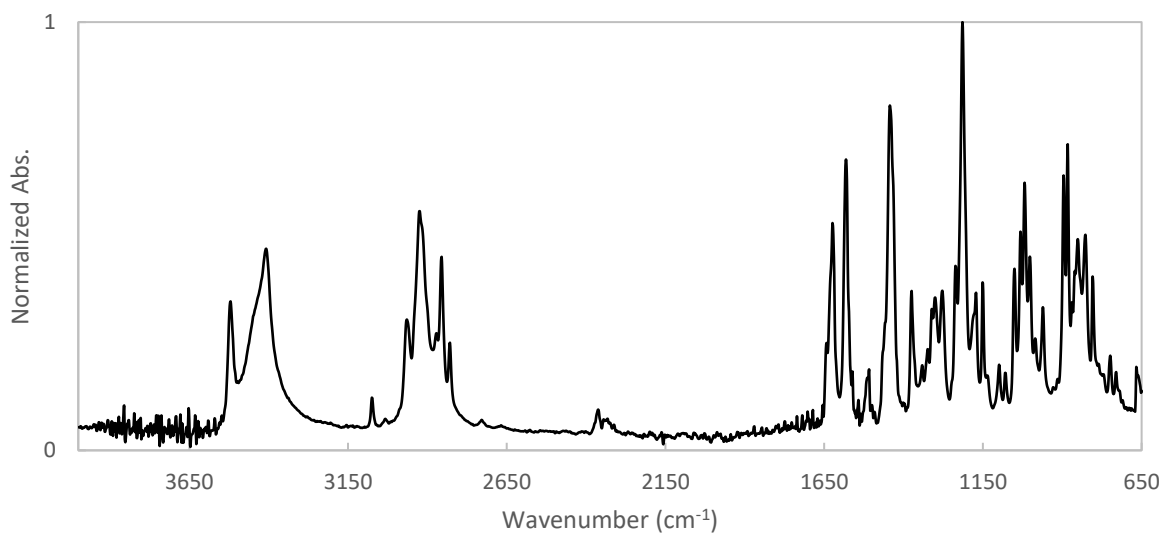


Figure 3.11 Micro-ATR-FTIR spectrum for sample CBD Shatter Crystals

To presumptively identify the crystalline and wax components of each Cannabidiol Life sample, each were subjected to a standard library search using the GRAMS IR spectral comparison software. For both crystalline samples, and the wax component of the CBD Wax sample, the top result was to a CBD nujol mull sample. Additionally, each Cannabidiol Life sample was compared to a THCA CRM. Comparison of the CBD Shatter Crystal sample to the THCA CRM spectrum (**Figure 3.12**) highlighted key differences.

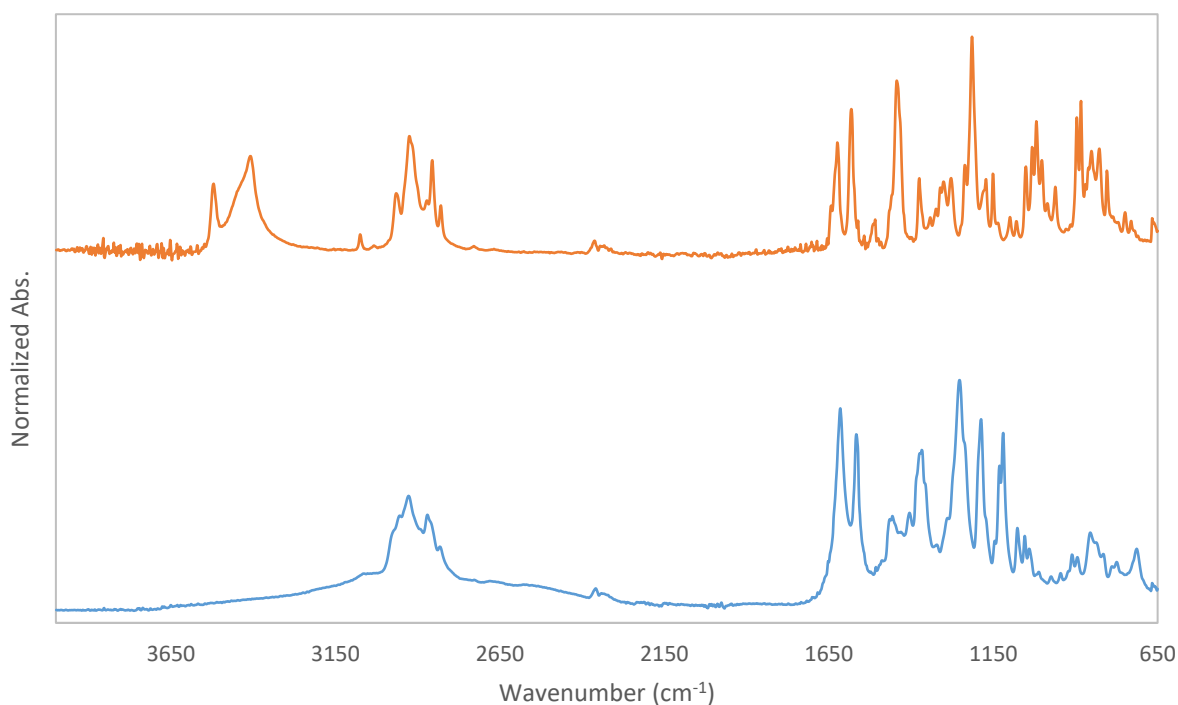


Figure 3.12 Stacked comparison of CBD Shatter Crystal (top) and THCA CRM (bottom)

3.3.2 Discussion of Micro-ATR-FTIR Analysis of Cannabis Solvent Extracts

As shown by **Figures 3.4 and 3.5**, the crystalline component of KDPS 18-9026 samples contains chemical characteristics comparable to that of the Skymint WB THCA Crystal dispensary sample. This is apparent due to both the presence of peaks at similar wavenumbers, as well as the ratio between normalized peak absorbances between the two crystal samples. The peaks present at ~ 2850 and ~ 2900 cm^{-1} are indicative of aliphatic C-H stretching. The lack of significant peaks above 3000 cm^{-1} suggests that the crystalline structure likely does not include many unsaturated C-C bonds (or those with adjacent C-H bonds), hydroxyl, or amine groups. Bands in the region between 1600 and 1650 cm^{-1} indicate alkene stretching, including cyclical and conjugated alkenes. In the fingerprint region of the spectrum, medium strength peaks located between ~ 1350 and ~ 1450 cm^{-1} are commonly due to hydroxyl bending, including bending from a carboxylic acid or phenol functional group. The most intense peak in the spectra at ~ 1250 cm^{-1} is due to C-O stretching, particularly by alkyl aryl ethers. Similarly, the peaks present between ~ 1120 and ~ 1190 cm^{-1} are caused by C-O stretching from tertiary hydroxyl groups. Finally, peaks below 900 cm^{-1} are generally due to C-H deformations, such as bending, twisting, and rocking.

Despite the lack of characteristic high frequency C-H stretching that occurs with unsaturated C-C bonds, strong bands suggesting alkene presence are included in the spectra between 1600 and 1650 cm^{-1} . This indicates the lack of hydrogens bonded to unsaturated carbons for this structure. Such a pattern of stretching points to the possibility of a cyclic alkene and multiply substituted aromatic ring structure with the addition of a saturated carbon chain, as indicated by the aliphatic C-H stretching and C-H deformations. Additionally, the stretching frequency in the region significant to alkyl aryl ethers further supports the likelihood of an

aromatic ring as part of the structure. Regardless of the strong stretching bands attributed to C-O bonds and hydroxyl bending, the spectrum lacks the characteristic broad, high frequency intermolecularly bonded O-H stretching peaks. This may indicate possible hydrogen bonding present in the crystalline structure, further stabilizing the hydroxyl groups.

Comparison of all crystalline sample spectra indicated similarities in structural components. Not only were the peaks present between samples similar in location, but the ratios between peaks were also comparable. Most notably, the crystalline component of each crystalline sample lacked O-H stretching in the high frequency region of the spectra but maintained peaks characteristic of C-O stretching and hydroxyl bending in the lower frequency regions of the spectra. Similarly, the presence of peaks indicative of cyclic and conjugated alkenes were found in each case sample spectra. These similarities provide confirmation that the crystalline components in both clandestine BHO samples and dispensary produced BHO samples are chemically comparable, in addition to being optically similar as described in **Chapter 2**.

Comparison of case sample spectrum to a spectrum of THCA CRM (**Figure 3.8**) highlighted similarities in organic functional groups. Similarities included peak presence and ratio specifically in the C-H bending ($\sim 850\text{ cm}^{-1}$), C-O alkyl aryl ether stretching ($\sim 1250\text{ cm}^{-1}$), O-H carboxylic acid and phenol bending ($\sim 1450\text{ cm}^{-1}$) and alkene stretching region ($\sim 1600\text{ cm}^{-1}$). Additionally, comparison of case sample spectra to a THC reference material spectrum (**Figure 3.9**) indicated stark differences, including a strong O-H stretching peak ($\sim 3200\text{-}3500\text{ cm}^{-1}$) and defined O-H phenol bending region (~ 1350 and $\sim 1450\text{ cm}^{-1}$). Due to the similarities between the THCA CRM and each case sample crystal, the crystalline component of BHO extracts was presumptively identified as THCA.

The spectrum of each case sample's wax component shared a high degree of similarity to their crystalline counterparts, with some minor, but notable, differences. The most readily visible spectral difference between these two components is the weak, broad peak present in the intermolecular O-H stretching region ($\sim 3200\text{-}3500\text{ cm}^{-1}$) of the wax component spectra. This peak is more defined in the individual IR spectra for each case sample (Appendix III). Further, although the two component's spectra contain peaks at similar wavenumbers, the relative ratios between peaks may indicate slight structural differences between the two components. Most notably, the peak ratios in the O-H bending ($\sim 1450\text{ cm}^{-1}$) regions and C-O stretching (1250 cm^{-1}) differ within the wax samples and between the wax and crystalline component spectra (**Figure 3.4**).

The characterization of the wax component was completed to further identify possible cannabinoids or natural waxes present. The texture and amount of wax component present differed between case samples, with textures ranging from soft and viscous to glass-like (**Table 3.3**). However, despite the differences in texture for the wax component, similar functional groups were identified. The harder, glass-like waxes appeared to provide a more defined, high absorbance O-H stretching peak, but the difference was minimal. Comparison of the wax component spectra of each case sample to the THC CRM spectrum highlighted similarities in organic functional groups. Similarities included peak presence and ratio specifically in the O-H stretching ($\sim 3350\text{ cm}^{-1}$), C-H bending ($\sim 850\text{ cm}^{-1}$), C-O alkyl aryl ether stretching ($\sim 1250\text{ cm}^{-1}$), O-H bending ($\sim 1450\text{ cm}^{-1}$) and alkene stretching region ($\sim 1600\text{ cm}^{-1}$). The addition of peaks in the O-H stretching region better correlated the wax component to THC than THCA, although similarities between the two cannabinoids were present given their high degree of structural similarity.

Given the optical differences between the Cannabidiol Life samples and the case samples and dispensary samples discussed previously, structural and chemical differences were expected. When analyzed by micro-ATR-FTIR, the crystalline component of the CBD Wax sample was analogous to the CBD Shatter Crystal sample (**Figure 3.10 and 3.11**). This was apparent due to both the presence of peaks at similar wavenumbers, as well as the ratio between normalized peak absorbances between the two crystal samples, with the only slight difference in ratios appearing in the fingerprint region of the spectra. The spectrum collected for the wax component of the CBD Wax sample included similar peaks to that of the crystalline component, indicating related chemical composition. However, some peak intensities and ratios differed between the two CBD Wax sample component spectra, but this did not lead to differences in library search results or spectral interpretation.

Within both CBD samples, the peaks present at ~ 3500 and ~ 3400 cm^{-1} are consistent with intermolecularly bonded O-H stretching. The weak, but reproducible peak at 3071 cm^{-1} relates to alkene C-H stretching, though such a stretching frequency is generally observed as a stronger (medium) relative absorbance. The weakness of this peak could indicate that the crystalline structure does not contain a significant amount of C-H bonds adjacent to alkene functional groups. The peaks between ~ 2850 and ~ 2900 cm^{-1} are indicative of aliphatic C-H stretching. Bands in the region between 1600 and 1650 cm^{-1} indicates alkene (C=C) stretching, including cyclical and conjugated alkenes. In the fingerprint region of the spectrum, the medium/strong strength peak located at 1440 cm^{-1} can be attributed to either hydroxyl or methyl bending, as both functional group frequencies occur in this region. The strongest peak in the spectra at ~ 1210 cm^{-1} is due to C-O stretching, possibly from ethers or hydroxyl functional group presence. Additionally, the series of sharp peaks present around ~ 1010 cm^{-1} may be due to alkene bending,

while the sharp peaks below 900 cm^{-1} are generally due to C-H deformations, such as bending, twisting, and rocking.

As highlighted in **Table 3.4**, Cannabidiol Life CBD Shatter Crystals had only a crystalline component, however CBD Wax contains both a crystalline and an oily, wax component. Given the inclusion of wax components in the THCA-containing samples, chemically characterizing the wax component of the CBD Wax sample may provide a more comprehensive analysis of the cannabinoids present in extracts derived from hemp, or other natural oils. **Figure 3.10** provides a representative spectrum of the oily, wax matrix surrounding the CBD Wax crystalline component.

When subjected to a standard library comparison search, a CBD nujol mull spectrum provided the best visible comparison. Additionally, the two Cannabidiol Life samples were compared to the THCA CRM material that was spectrally similar to the KCSD case samples and Skymint dispensary samples (**Figure 3.12**). Though the Cannabidiol Life and THCA CRM spectra contain similar functional groups based on IR interpretation, the wavenumber and ratios of peaks in each spectra differ drastically. Most notably, the inclusion of O-H stretching and unsaturated C-H stretching peaks provided key discrepancies between the CBD Shatter crystals and THCA CRM. Moreover, the peaks in the CBD Shatter Crystal spectrum are more defined and sharper compared to the THCA CRM spectrum. The increased sharpness and definition in the CBD Shatter Crystal spectrum may be due to the well-formed crystalline structure of the sample, compared to the dried, oily residue of the THCA CRM.

As presented in the previous sections, the two optically different crystal groups, as represented by clandestine and dispensary BHO samples and the Cannabidiol Life dispensary samples, also differ in chemical characterization. To better showcase the difference in chemical

characteristics as determined by micro-ATR-FTIR, **Figure 3.13** provides stacked spectra of representative samples from each sample set: KDPS 18-9026, WB THCA Crystal, and CBD Shatter Crystal samples.

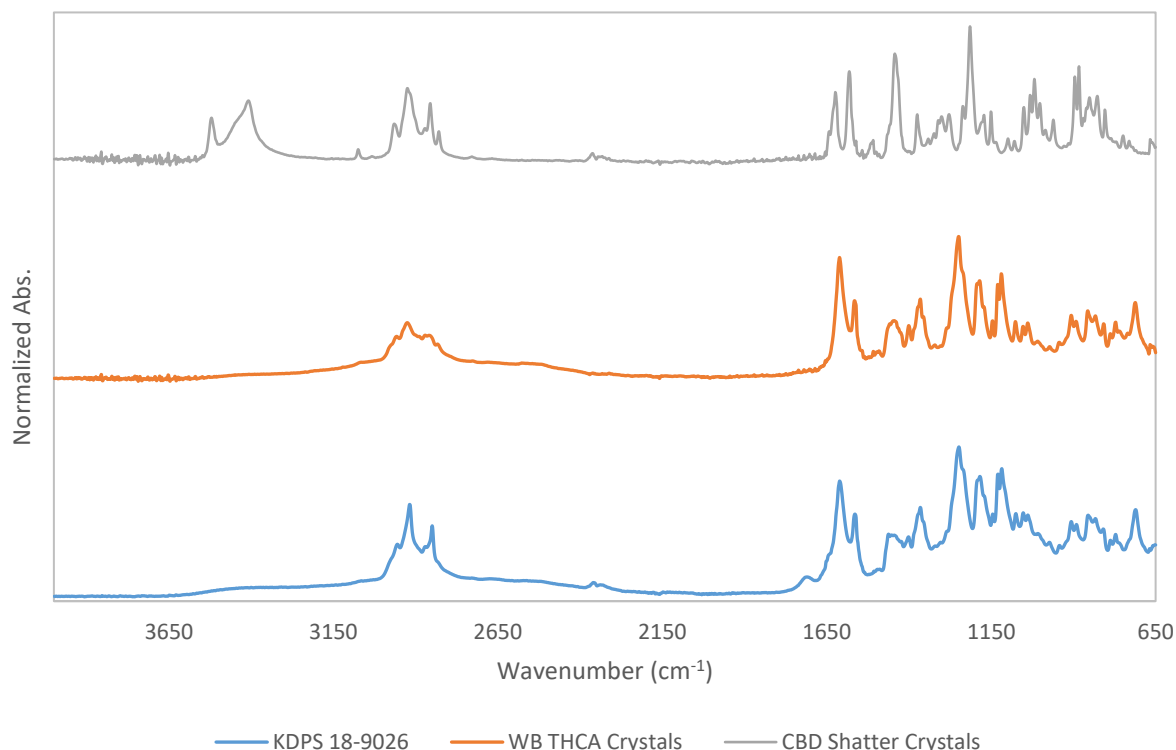


Figure 3.13 Stacked spectra comparing the crystalline components of KDPS 18-9026 (bottom), WB THCA Crystals (middle), and CBD Shatter Crystals (top)

As displayed, the KDPS 18-9026 and WB THCA Crystals samples contain similar functional groups, represented by the similar peak location and ratios present in the stacked spectra. Oppositely, the CBD Shatter Crystal sample does not spectrally correlate to either of the THCA-containing samples, despite sharing structural functional group similarities, such as conjugated alkene groups (aromatic ring structures), hydroxyl groups, and alkane moieties.

Additionally, despite the inclusion of carboxylic acid and hydroxyl functional groups in the KDPS 18-9026 and WB THCA Crystal samples, distinctive O-H stretching is only observed in the CBD Shatter Crystal sample spectrum. This indicated the likely presence of strong hydrogen bonding present in the THCA-containing crystal samples, but lack of such strong bonding in the CBD-containing samples.

3.4 STRUCTURAL ELUCIDATION OF CANNABIS SOLVENT EXTRACT

CRYSTALS

3.4.1 Results of Single-Crystal XRD Analysis for Structural Elucidation

3.4.1.1 Single-Crystal XRD Analysis of Optically Similar Samples - KDPS 18-9026 and WB THCA Crystals

The representative samples from each subset of optically similar crystals were analyzed by single-crystal XRD for structural elucidation and confirmatory identification. Following XRD data collection and structural refinement, the crystal component of the BHO case sample extracts, as represented by KDPS 18-9026, was determined to be the cannabinoid THCA. Similarly, the crystals from the Skymint WB THCA Crystal sample were identified as THCA. The solved crystal structure is displayed in **Figure 3.14**. The crystal structure shows dimer properties due to hydrogen bonding from carboxylic acid groups (**Figure 3.15**). Details of crystal data and refinement for each sample are compiled in **Table 3.5**. Due to the high degree of similarity in structural results between the two crystals, the figures provided here are only a subset of data collected specifically related to the single-crystal XRD analysis of case sample KDPS 18-9026; however, similar figures for the WB THCA Crystal sample are shown in Appendix III, along with supplemental figures from each XRD report.

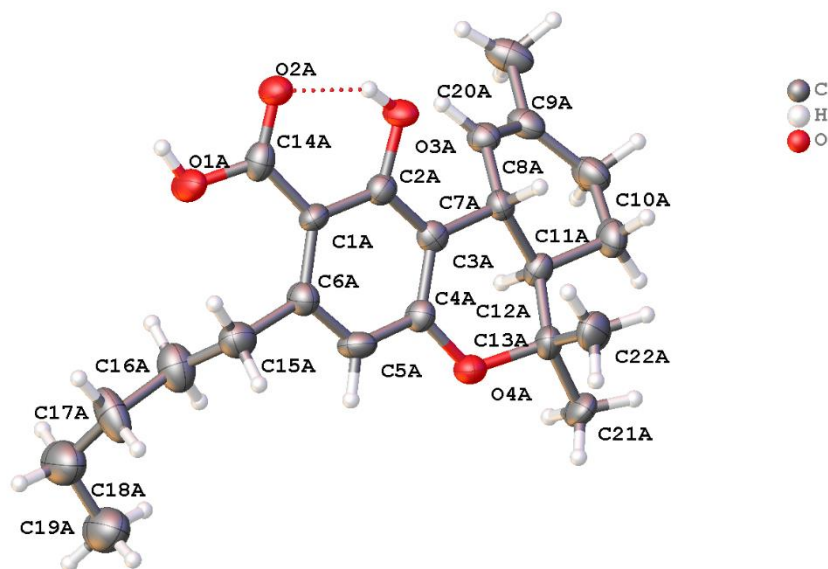


Figure 3.14 Crystal structure from case sample KDPS 18-9026 determined by single-crystal XRD shown with molecular labelling scheme.

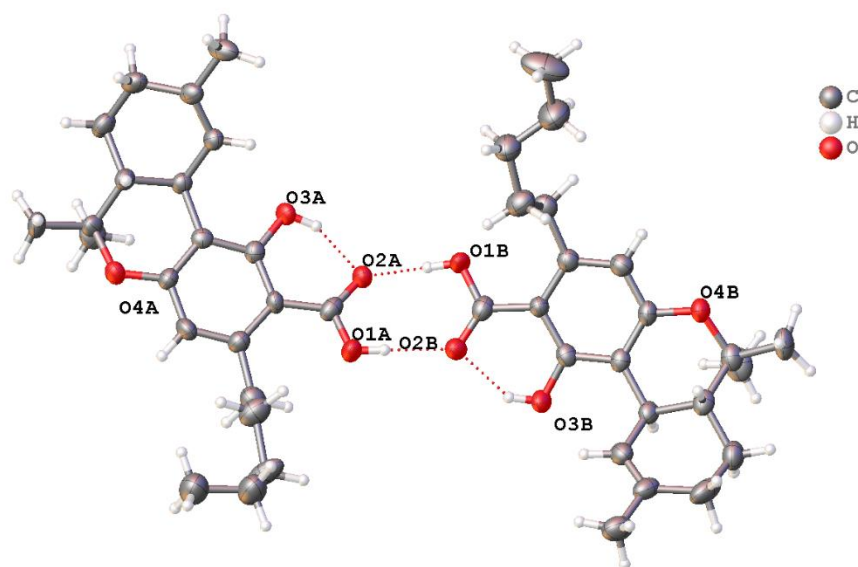


Figure 3.15 Crystal structure from case sample KDPS 18-9026 displaying racemic, dimer crystalline properties

Table 3.5 Crystal data and structure refinement details of KDPS 18-9026 and WB THCA

Crystal samples

	KDPS 18-9026	WB THCA Crystals
Formula	C ₂₂ H ₃₀ O ₄	C ₂₂ H ₃₀ O ₄
<i>D_{calc.}</i> / g cm ⁻³	1.193	1.213
<i>μ</i> /mm ⁻¹	0.644	0.655
Formula Weight	358.46	358.46
Color	colorless	colorless
Shape	chunk	block
Size/mm³	0.18×0.07×0.06	0.12×0.07×0.03
<i>T</i> /K	173(1)	100.00(10)
Crystal System	orthorhombic	orthorhombic
Flack Parameter	0.2(5)	-0.07(7)
Hoof Parameter	0.3(3)	-0.04(6)
Space Group	<i>P</i> 2 ₁ 2 ₁ 2 ₁	<i>P</i> 2 ₁ 2 ₁ 2 ₁
<i>a</i> /Å	11.4189(3)	11.40867(12)
<i>b</i> /Å	18.1043(6)	17.98950(19)
<i>c</i> /Å	19.3024(7)	19.1297(2)
<i>a</i> [°]	90	90
<i>b</i> [°]	90	90
<i>g</i> [°]	90	90
<i>V</i> /Å ³	3990.4(2)	3926.11(8)
Z	8	8
Z'	2	2
Wavelength/Å	1.54178	1.54184
Radiation type	CuK _α	CuK _α
<i>Q_{min}</i> [°]	3.347	3.372
<i>Q_{max}</i> [°]	58.941	77.428
Measured Reflections	14444	27768
Independent Refl's	5555	8018
Refl's with I > 2(I)	3091	7551
<i>R_{int}</i>	0.1207	0.0458
Parameters	482	493
Restraints	0	0
Largest Peak	0.195	0.164
Deepest Hole	-0.218	-0.191
GooF	0.985	1.038
<i>wR₂</i> (all data)	0.1390	0.0834
<i>wR₂</i>	0.1098	0.0819
<i>R₁</i> (all data)	0.1434	0.0371
<i>R₁</i>	0.0638	0.0341

3.4.1.2 Single-Crystal XRD Analysis of CBD Shatter Crystals

Due to the similarity in chemical composition and optical characteristics between the crystalline components of each dispensary sample, a representative crystal from the CBD Shatter Crystal sample was selected for structural elucidation and identification by single-crystal XRD. Following XRD data collection and structural refinement, the crystal component of CBD-containing dispensary samples, as represented by CBD Shatter Crystals, was determined to be the cannabinoid CBD. The solved crystal structure is displayed in **Figure 3.16**. The crystal structure shows a chiral crystal with dimer properties due to hydrogen bonding from hydroxyl groups (**Figure 3.17**). Details of crystal data and refinement for each sample are compiled in **Table 3.6**.

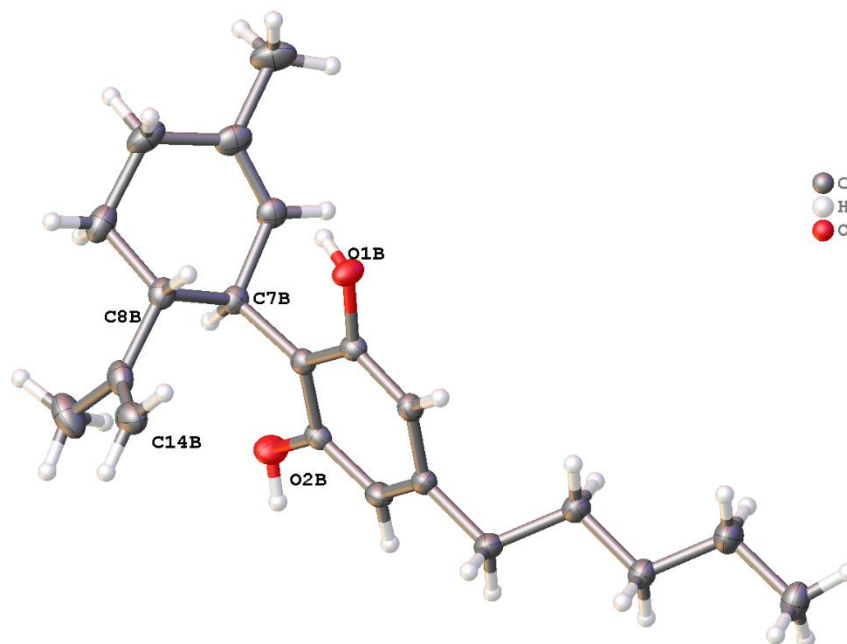


Figure 3.16 Crystal structure from dispensary sample CBD Shatter Crystal determined by single-crystal XRD shown with molecular labelling scheme of chiral atoms.

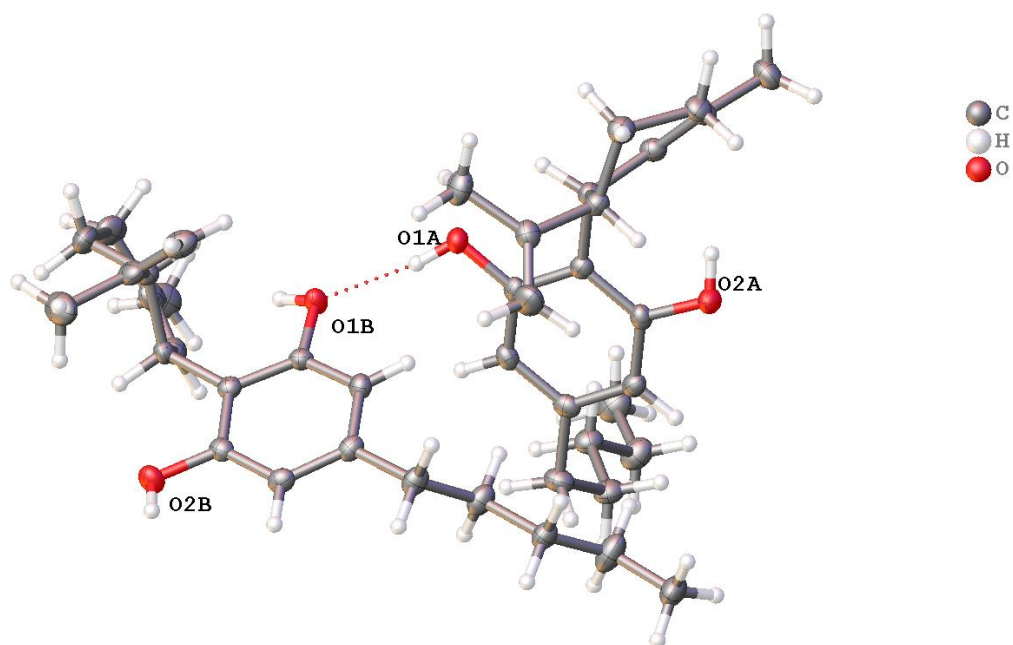


Figure 3.17 Crystal structure from dispensary sample CBD Shatter Crystal displaying hydrogen bonding and dimer crystalline properties

Table 3.6 Crystal data and structure refinement details of CBD Shatter Crystal sample

CBD Shatter Crystal	
Formula	C ₂₁ H ₃₀ O ₂
<i>D</i>_{calc.}/ g cm⁻³	1.110
<i>μ</i>/mm⁻¹	0.535
Formula Weight	314.45
Color	colorless
Shape	block
Size/mm³	0.33×0.22×0.15
<i>T</i>/K	100.01(10)
Crystal System	monoclinic
Flack Parameter	-0.02(10)
Hooft Parameter	0.01(9)
Space Group	<i>P</i> 2 ₁
<i>a</i>/Å	10.40257(14)
<i>b</i>/Å	10.89329(15)
<i>c</i>/Å	16.6836(2)
<i>a</i>'°	90
<i>b</i>'°	95.5081(12)
<i>g</i>'°	90
<i>V</i>/Å³	1881.82(4)
<i>Z</i>	4
<i>Z</i>'	2
Wavelength/Å	1.54184
Radiation type	Cu K _α
<i>Q</i>_{min}'°	2.661
<i>Q</i>_{max}'°	77.347
Measured Refl's.	24375
Ind't Refl's	7633
Refl's with <i>I</i> > 2(<i>I</i>)	7318
<i>R</i>_{int}	0.0487
Parameters	438
Restraints	1
Largest Peak	0.169
Deepest Hole	-0.147
GooF	1.024
<i>wR</i>₂ (all data)	0.0857
<i>wR</i>₂	0.0844
<i>R</i>₁ (all data)	0.0363
<i>R</i>₁	0.0348

3.4.2 Discussion of Single-Crystal XRD Analysis for Structural Elucidation

Case sample KDPS 18-9026 and the Skymint dispensary WB THCA crystal sample were both identified as THCA; with analogous crystal structures identified by single-crystal XRD. As shown in **Table 3.5**, the chemical formula determined for the crystal structures match that of THCA ($C_{22}H_{30}O_4$), and the structures between the solved crystalline component and THCA are analogous. A representative structure of THCA is provided in Appendix III. The crystal system for the structure was determined to be orthorhombic, based on the presence of unequal crystallographic axis lengths (a, b, and c) while all maintaining right angles to one another (α , β , γ). Additionally, the space group for the crystal was found to be $P2_12_12_1$, indicating a primitive Bravais lattice (denoted by P) in the orthorhombic crystal system. The notation $2_12_12_1$ refers to the symmetry related to the screw axes along the x, y, and z coordinate directions. Within the unit cell, eight total THCA molecules are present, denoted by Z in **Table 3.5**. The notation Z' refers to the number of molecules that make up the asymmetrical unit – the smallest portion of the unit cell that can be moved symmetrically (in this case by screw operations) to produce the full unit cell. A packing diagram depicting the molecules in the unit cell is provided in Appendix III. Similarities and small differences between the refined data of the two crystalline samples are present when comparing the results in **Table 3.5**. Most notably, the solved chemical formula, mass, crystal system, space group, and crystallographic axis angles are analogous between the two samples. This corresponds to the similarity in their optical properties.

While the solved structure and identity of the two crystal samples can be considered analogous, there are numerical differences in the exact results provided by **Table 3.5**. During data collection for KDPS 18-9026, 14444 total reflections were measured. Of those measured reflections, 5555 were determined to be independent and not related by symmetry. These data

were collected to a final completeness of 99.50%, which is desirable for structural refinement. The values for total and independent reflections for WB THCA Crystals were larger than that of KDPS 18-9026, and the data were collected to a final completeness of 100%. The difference in total data collected is instrument-dependent and does not reflect an inadequacy or quality issue in regard to the crystal analysis. The parameters that define the fit of the determined structure to the experimental electron density are labeled as “GooF,” “wR₂,” and “R₁.” Goodness of fit (GooF) should approach 1 for well-fit models, while wR₂ and R₁ should approach 0. Ideal structural solutions would have R₁ values equal to 0, but due to random error this cannot occur. For case sample KDPS 18-9026, the confidence value for GooF, wR₂ (all data) and R₁ are in an acceptable, publishable range.²² Similarly, for dispensary sample WB THCA crystals the confidence values for GooF, wR₂, and R₁ indicates that the refined experimental structure has little error relative to the theoretical solved structure.

Comparatively, the WB THCA crystal has less overall error relative to the theoretical solved structure than the KDPS 18-9026 case sample crystal. The Flack and Hooft parameters provide insight in regards to the decrease fit of the KDPS 18-9026 sample to the theoretical structure. The Flack and Hooft parameters provide data related to the absolute structure configuration given by refinement. The Flack parameter is generally found between 0 and 1, with values close to 0 indicating correct structural refinement, while values near 1 suggest that an inverted structure is correct. Additionally, values around 0.5 indicate a racemic or twinned crystal.²³ The Hooft parameter can be thought of as the Flack parameter determined through Bayesian statistics and is used to define the probability of structural accuracy.²⁴ For case sample KDPS18-9026, the Flack and Hooft parameters indicate a racemic crystal with two enantiomers possible in the crystal formation. Conversely, the dispensary WB THCA crystal is chiral, which

only one enantiomer possible in the crystal formation. Given the racemic nature of the KDPS 18-9026 crystal, the fit of the experimental structure to the theoretical structure was lower than the chiral WB THCA crystal, resulting in slightly worse goodness of fit values.

Due to the racemic nature of the crystals from case sample 18-9026 versus the chiral nature of the WB THCA crystal sample, small differences exist between the length of crystallographic axes (a, b, and c), with a maximum difference between sample values of ~2.8%. The two enantiomers present in the racemic crystal would effectively elongate a crystallographic axis, as demonstrated by the numerical data provided in **Table 3.5**. Additionally, the chiral nature of the WB THCA crystal could indicate a purer sample, as WB THCA Crystals were purchased from a dispensary utilizing professional, regulated manufacturing techniques compared to the assumed clandestine production of case sample KDPS 18-9026. Additionally, it would be more common for crystalline impurities to be present in a clandestine manufactured product, such as KDPS 18-9026, which may lead to decreased crystal quality and increased error during structure refinement. Such impurities can be incorporated into the crystal during the growing phase of crystallization, especially when this phase occurs in an uncontrolled environment, or takes place rapidly.

The identification of both the KDPS 18-9026 and Skymint WB THCA Crystal sample's crystalline components as THCA confirms the presumptive identification by micro-ATR-FTIR. When comparing the micro-ATR-FTIR spectra obtained for KDPS 18-9026 to the structure provided by single-crystal XRD, complementary functional groups are present. Additionally, the structural elucidation by single-crystal XRD provided insight related to the hydrogen bonding responsible for the lack of characteristic O-H stretching peaks in the micro-ATR-FTIR spectra. As shown in **Figure 3.15**, the dimer properties and hydrogen bonding between the two THCA

molecules in the unit cell would reduce the strength of the stretching vibration for the hydroxyl groups present on each molecule. Also included in the refined structure is an alkyl aryl ether, which correlates to the strong peak at $\sim 1250\text{ cm}^{-1}$ as characterized by micro-ATR-FTIR.

Furthermore, parallels can be drawn between the optical characterization described in **Chapter 2** and the single-crystal XRD results presented here. Optically, the crystal was characterized as fitting in the orthorhombic crystal system, similar to the XRD determination. While the length of crystallographic axes cannot be measured by optical crystallography methods such as polarized light microscopy (PLM), measuring the principle refractive indices of the crystalline structures within BHO provides insight related to the equality of crystalline axis lengths. Given that each refractive index had a distinct, different value, the length of the crystallographic axes too could be inferred as unequal. This inference can be made due to the fact that the relationship between optical axes (refractive indices) and crystallographic axes is direct, as demonstrated by optical indicatrices. Additionally, the conoscopic characteristics of the case sample crystalline component indicated that the samples were biaxial (containing two optic axes) which relates to the orthorhombic, monoclinic, and triclinic crystal systems. Finally, the extinction characteristics observed for the crystals, with extinction occurring every $\sim 90^\circ$ rotation indicated that the angles between optic axes, and thus the crystallographic axes, were all equal to 90° , paralleling the results obtained by single-crystal XRD for the crystalline component of KDPS 18-9026 and WB THCA Crystals. Finally, given the optical and spectroscopic similarities between each of the case samples and Skymint dispensary samples, the crystalline components of each can be identified as THCA.

The Cannabidiol Life CBD Crystal sample was identified as CBD through single-crystal XRD analysis. As shown in **Table 3.5**, the chemical formula determined for the crystal structures

match that of CBD ($C_{21}H_{30}O_2$), and the structures between the solved crystalline component and CBD are analogous. A representative structure of CBD is provided in Appendix III. The crystal system for the structure was determined to be monoclinic, based on the presence of unequal crystallographic axis lengths (a, b, and c) and the presence of two 90° angles (α , γ) and one inclined crystallographic angle (β). Additionally, the space group for the crystal was found to be $P2_1$, indicating a primitive Bravais lattice (denoted by P) in the monoclinic crystal system. The notation 2_1 refers to the symmetry related to a two-fold screw symmetry along the x coordinate direction. Within the unit cell, a total of four CBD molecules are present, denoted by Z in **Table 3.5**, with two independent molecules symmetrically filling the entire unit cell. A packing diagram depicting the molecules in the unit cell is provided in Appendix III.

The confirmed identification of CBD Shatter Crystal samples as CBD coincides with the presumptive identification by micro-ATR-FTIR. When comparing the micro-ATR-FTIR spectra obtained for the CBD Shatter Crystal dispensary sample to the structure provided by single-crystal XRD, complementary functional groups are present. Furthermore, parallels can be drawn between the optical characterization described in **Chapter 2** and the single-crystal XRD results presented here. Optically, the crystal was characterized as fitting in the monoclinic crystal system, similar to the XRD determination. While the length of crystallographic axes cannot be measured by optical crystallography methods such as PLM, measuring the principle refractive indices of the crystalline structures within the CBD-containing dispensary samples provides insight related to the inequality of crystalline axis lengths. Given that each refractive index had a distinct, difference value, the length of the crystallographic axes too could be inferred to be unequal. Additionally, the conoscopic characteristics of the case sample crystalline component indicated that the samples were biaxial (containing two optic axes) which relates to the biaxial

orthorhombic, monoclinic, and triclinic crystal systems. Finally, the extinction characteristics observed for the crystals, with extinction occurring every $\sim 90^\circ$ rotation, as well as an extinction observed at an inclined angle to the crystal cleavage boundaries, indicated that the angles between optic axes include both a 90° angle and an inclined angle paralleling the results obtained by single-crystal XRD for the CBD-containing dispensary samples.

The structural differences between the THCA-containing samples and CBD-containing sample as determined by single-crystal XRD correlate to discrepancies noted both chemically and optically. **Table 3.7** summarizes key results related to the refined structures and identities of the crystalline samples representing the KCSD case samples, Sky mint dispensary samples, and Cannabidiol Life dispensary samples. Additionally, **Figure 3.18** provides a side-by-side comparison of the refined crystal structures for KDPS 18-9026 (**A**) and the CBD Shatter Crystal samples (**B**). As provided by **Table 3.7** and **Figure 3.18**, the chemical formula and structure for the KDPS 18-9026 and WB THCA Crystal samples was determined to be the cannabinoid THCA, while the CBD Shatter Crystal sample was shown to be the cannabinoid CBD.

Table 3.7 Comparison of refined data for crystals analyzed by single-crystal XRD

	KDPS 18-9026	WB THCA Crystals	CBD Shatter Crystals
Formula	C ₂₂ H ₃₀ O ₄	C ₂₂ H ₃₀ O ₄	C ₂₁ H ₃₀ O ₂
<i>D_{calc.}</i> / g cm ⁻³	1.193	1.213	1.110
<i>μ</i> /mm ⁻¹	0.644	0.655	0.535
Formula Weight	358.46	358.46	314.45
Crystal System	orthorhombic	orthorhombic	monoclinic
Flack Parameter	0.2(5)	-0.07(7)	-0.02(10)
Hooft Parameter	0.3(3)	-0.04(6)	0.01(9)
Space Group	<i>P</i> 2 ₁ 2 ₁ 2 ₁	<i>P</i> 2 ₁ 2 ₁ 2 ₁	<i>P</i> 2 ₁
<i>a</i> /Å	11.4189(3)	11.40867(12)	10.40257(14)
<i>b</i> /Å	18.1043(6)	17.98950(19)	10.89329(15)
<i>c</i> /Å	19.3024(7)	19.1297(2)	16.6836(2)
<i>a</i> °	90	90	90
<i>b</i> °	90	90	95.5081(12)
<i>g</i> °	90	90	90
<i>V</i> /Å ³	3990.4(2)	3926.11(8)	1881.82(4)
<i>Z</i>	8	8	4
<i>Z</i> '	2	2	2
Goof	0.985	1.038	1.024
<i>wR</i> ₂ (all data)	0.1390	0.0834	0.0857
<i>wR</i> ₂	0.1098	0.0819	0.0844
<i>R</i> _I (all data)	0.1434	0.0371	0.0363
<i>R</i> _I	0.0638	0.0341	0.0348

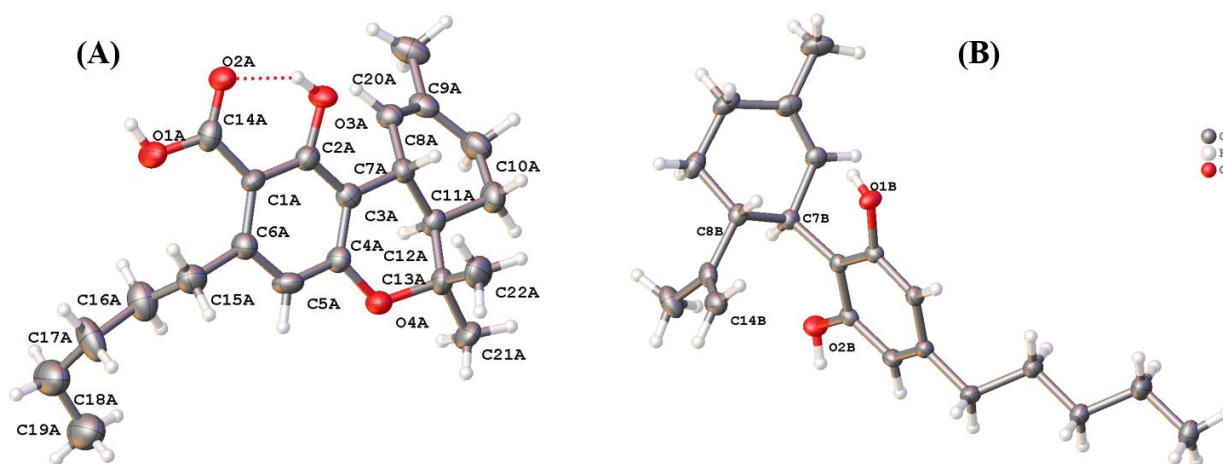


Figure 3.18 Comparison of single-crystal XRD refined structures for KDPS 18-9026 (A) and CBD Shatter Crystals (B)

The confirmatory identification of the crystalline components by single-crystal XRD, in addition to the spectroscopic analysis highlighted by micro-ATR-FTIR analysis, provides a comprehensive chemical characterization of a set of cannabis solvent extracts derived from both marijuana and hemp. Further, the crystals could be optically differentiated, as discussed in **Chapter 2**, due to the crystallographic differences highlighted in **Table 3.7**. Most notably, the difference in crystal systems derived from the crystallographic axes and angles measurements are readily differentiable by optical and X-ray crystallography. The combination of optical and spectroscopic characterization of the crystalline components provides a method through which cannabis solvent extracts derived from both marijuana and hemp can be preliminarily screened. Noting the distinct optical differences between the THCA and CBD crystals in each subset, as identified by spectroscopic analysis, optical characterization of cannabis extracts by PLM can provide discrimination prior to confirmatory identification by either spectroscopic analysis or additional SWGDRUG recommended analytical techniques.

APPENDIX

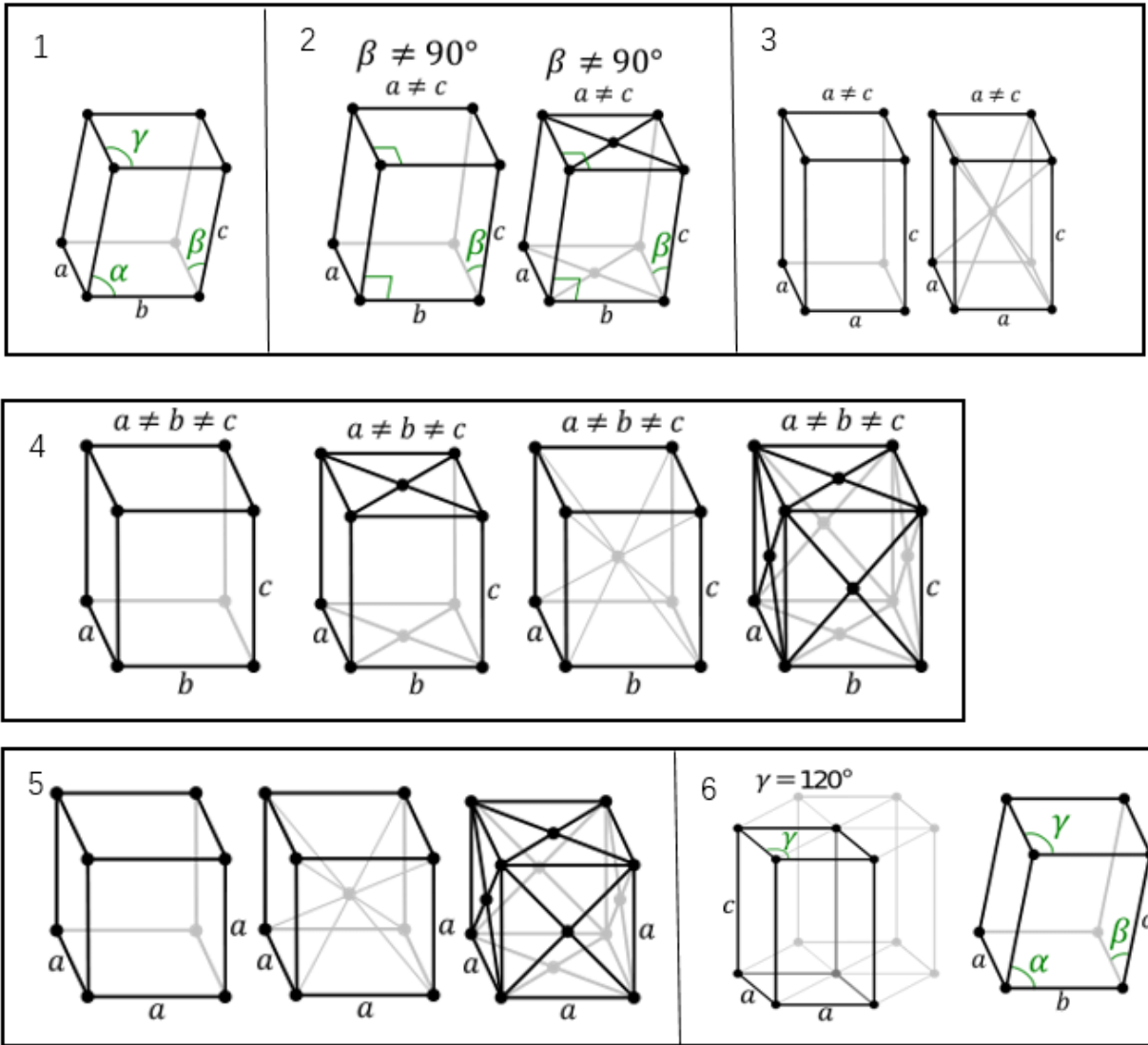


Figure A3.1 Geometric depictions of Bravais lattices²⁵

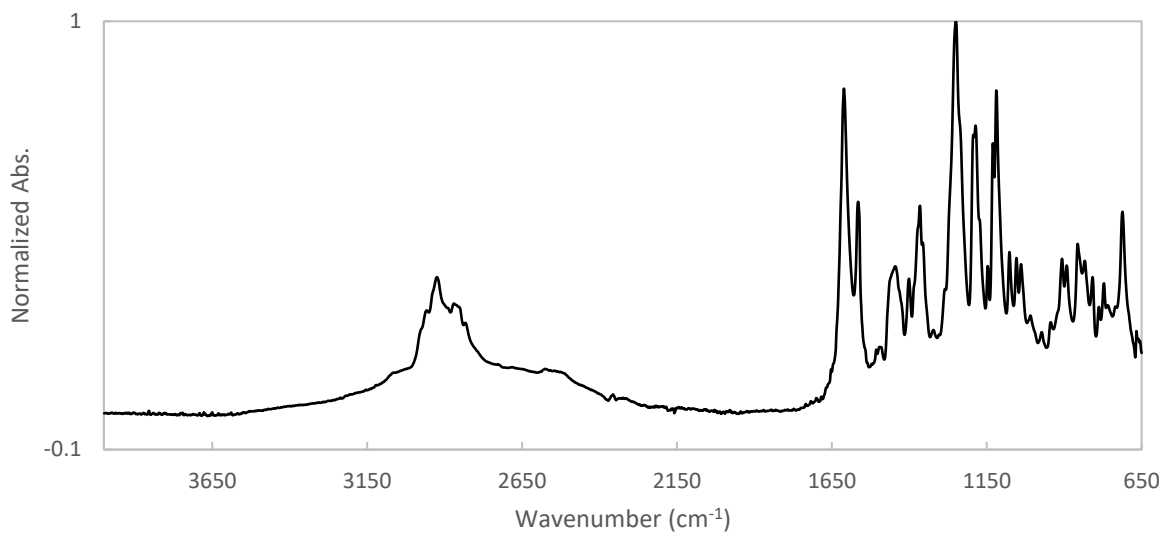


Figure A3.2 PPO 14-20332-10 micro-ATR-FTIR spectrum

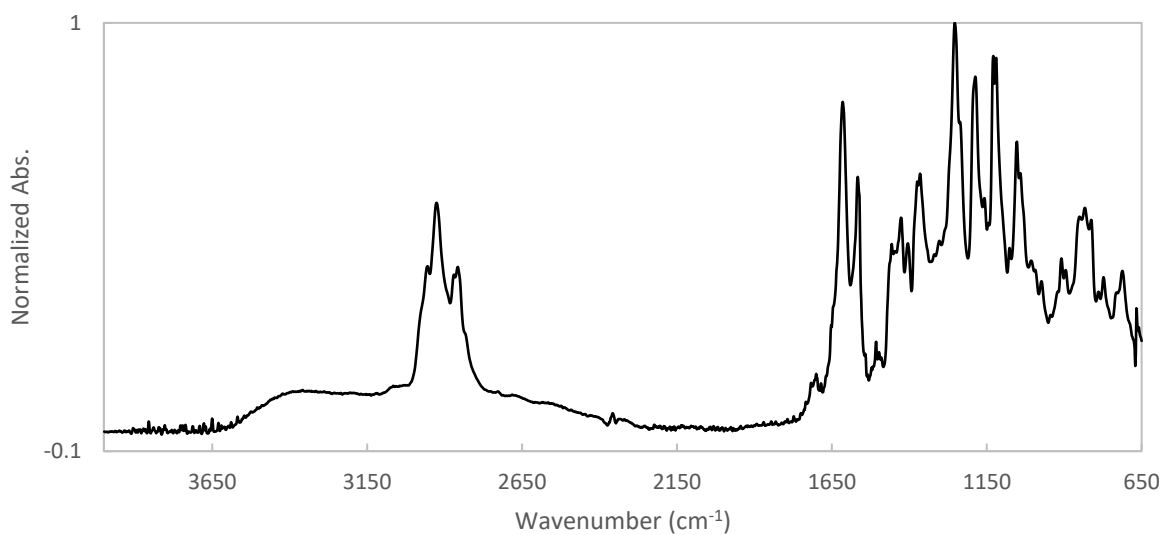


Figure A3.3 KCSD 14-10811 – 28967 micro-ATR-FTIR spectrum

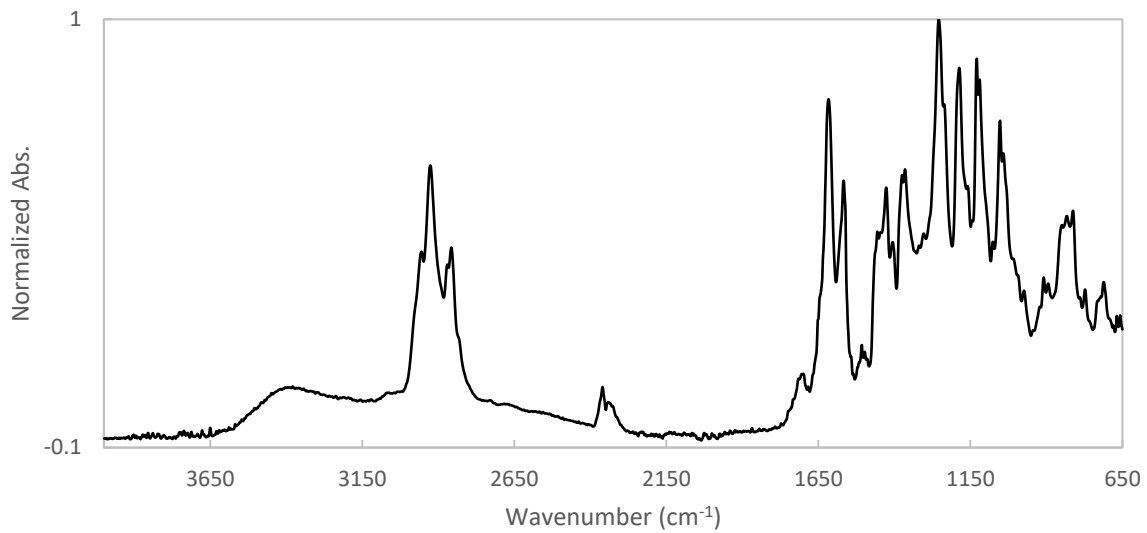


Figure A3.4 KCSD 14-10811 – 28960 micro-ATR-FTIR spectrum

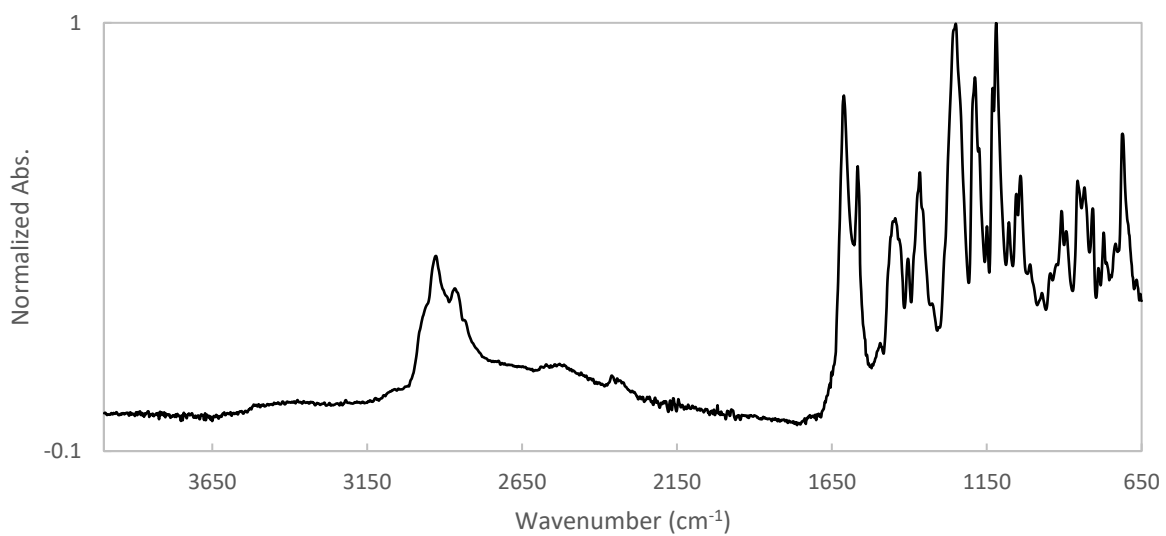


Figure A3.5 KCSD 14-10811 – 28964 micro-ATR-FTIR spectrum

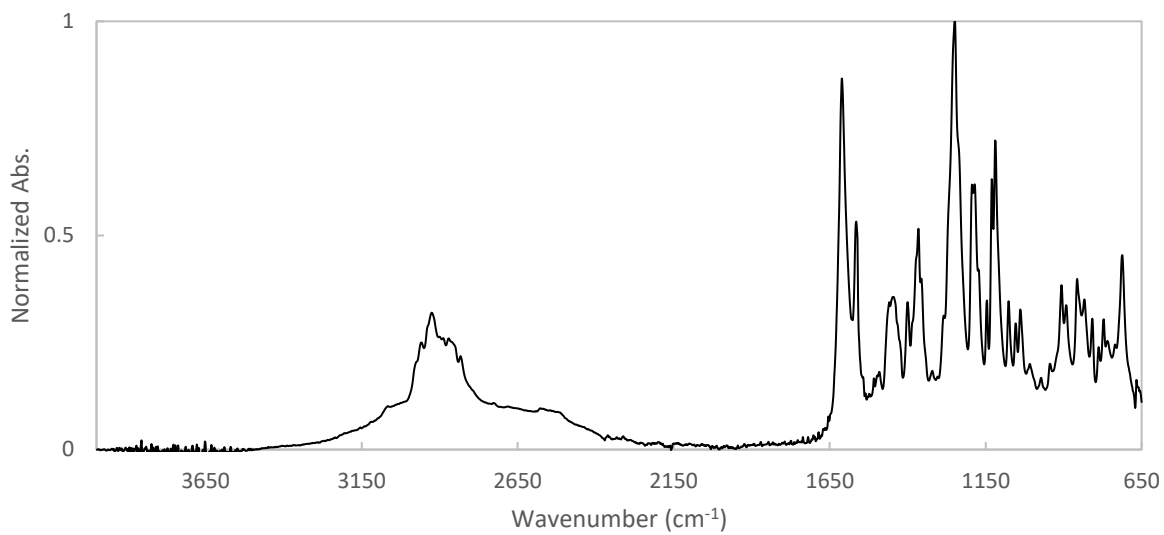


Figure A3.6 Skymint PB THCA Wax crystalline component spectrum

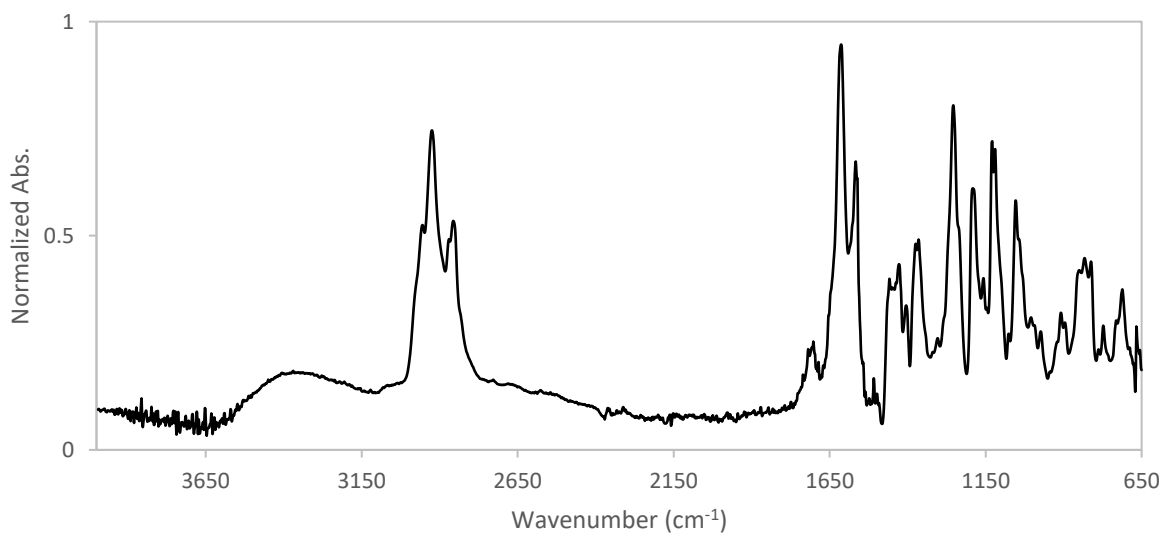


Figure A3.7 PPO 14-20332-10 wax component micro-ATR-FTIR spectrum (baseline corrected)

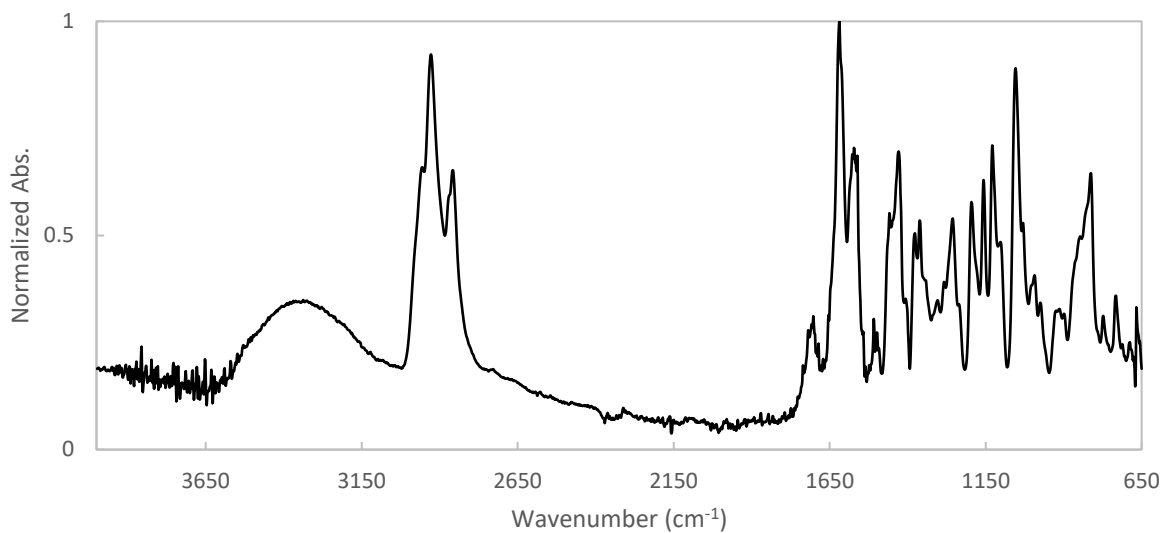


Figure A3.8 KCSD 14-10811 – 28967 wax component micro-ATR-FTIR spectrum (baseline corrected)

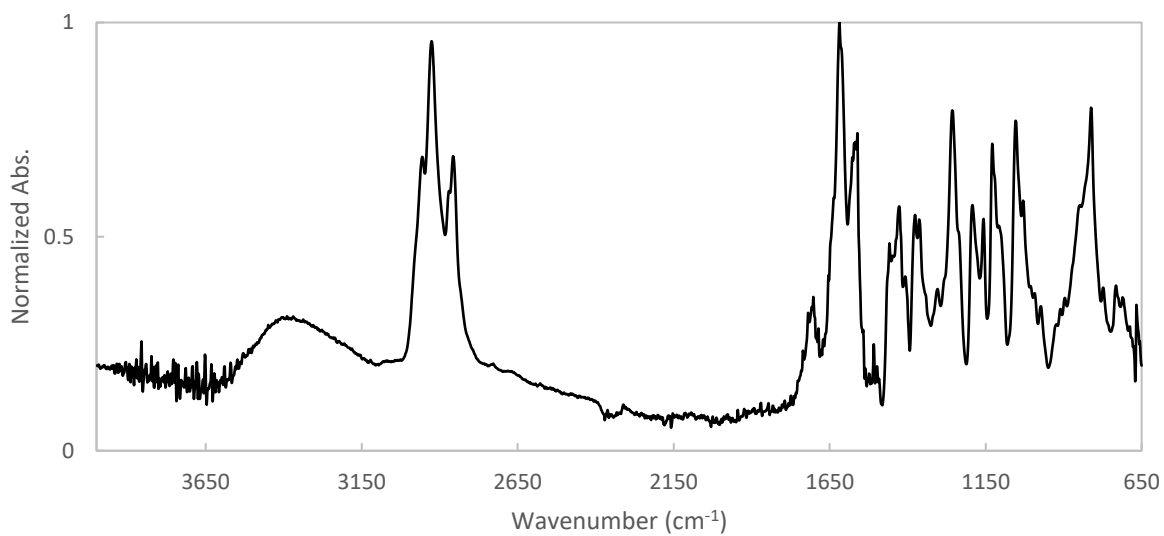


Figure A3.9 KCSD 14-10811 – 28960 wax component micro-ATR-FTIR spectrum (baseline corrected)

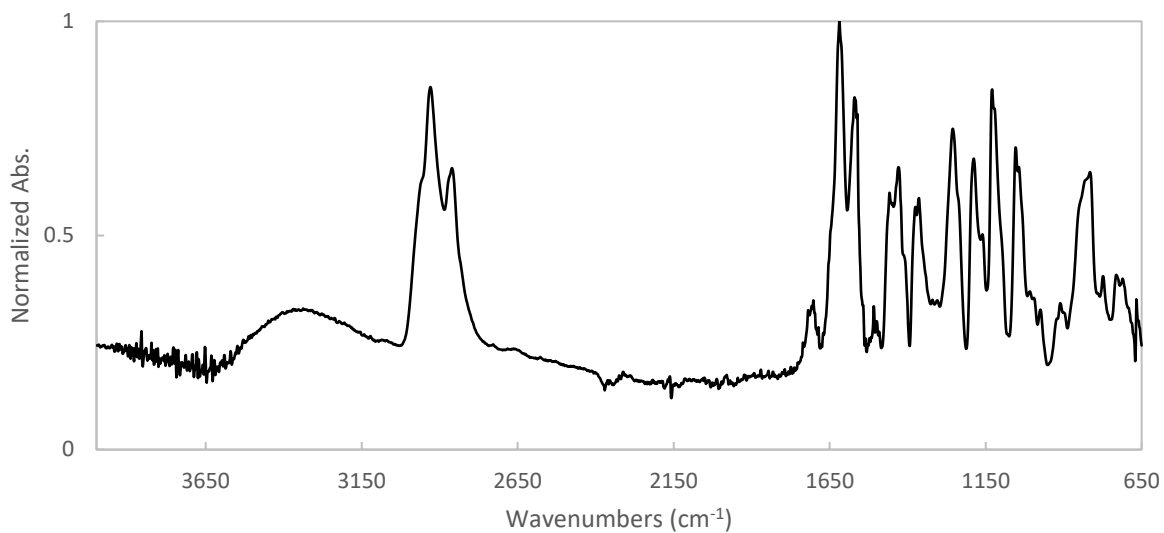


Figure A3.10 KCS D 14-10811 – 28964 wax component micro-ATR-FTIR spectrum (baseline corrected)

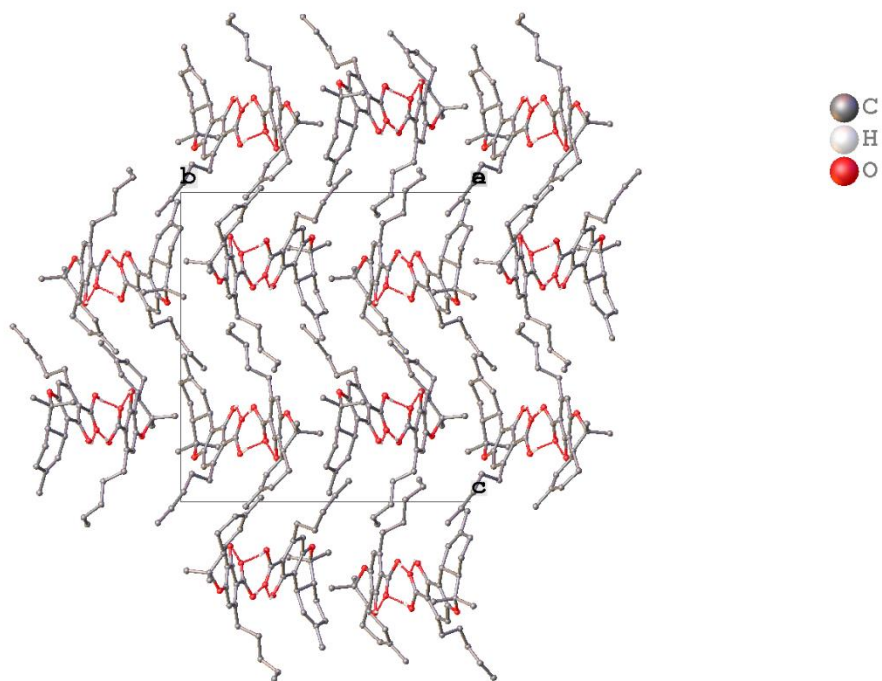


Figure A3.11 KDPS 18-9026 XRD packing diagram

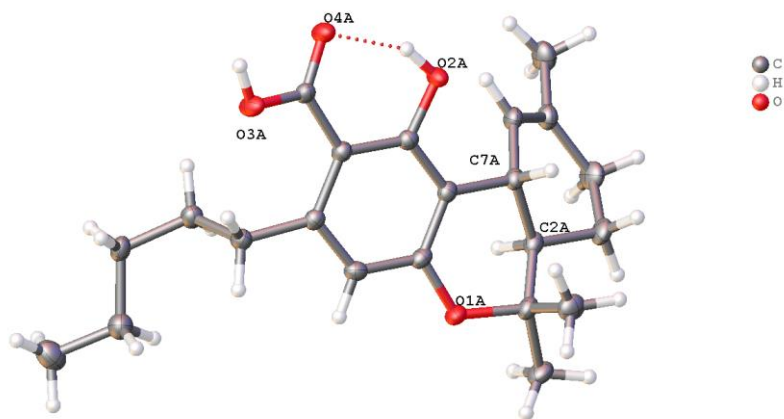


Figure A3.12 WB THCA Crystal XRD structure showing chiral centers

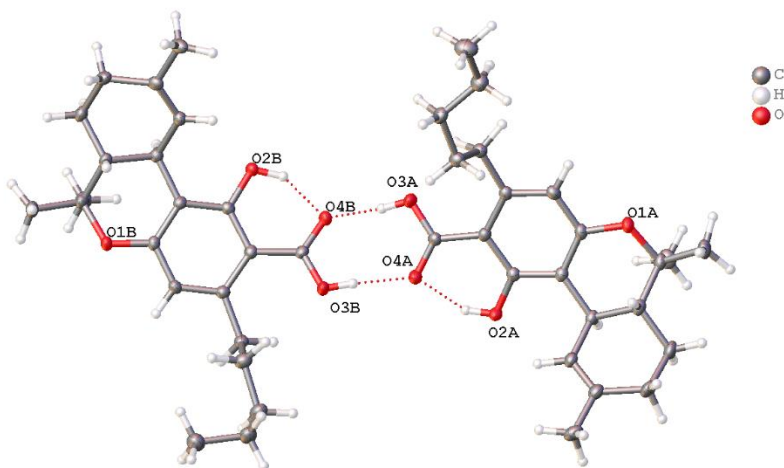


Figure A3.13 WB THCA Crystal XRD structure showing hydrogen bonding

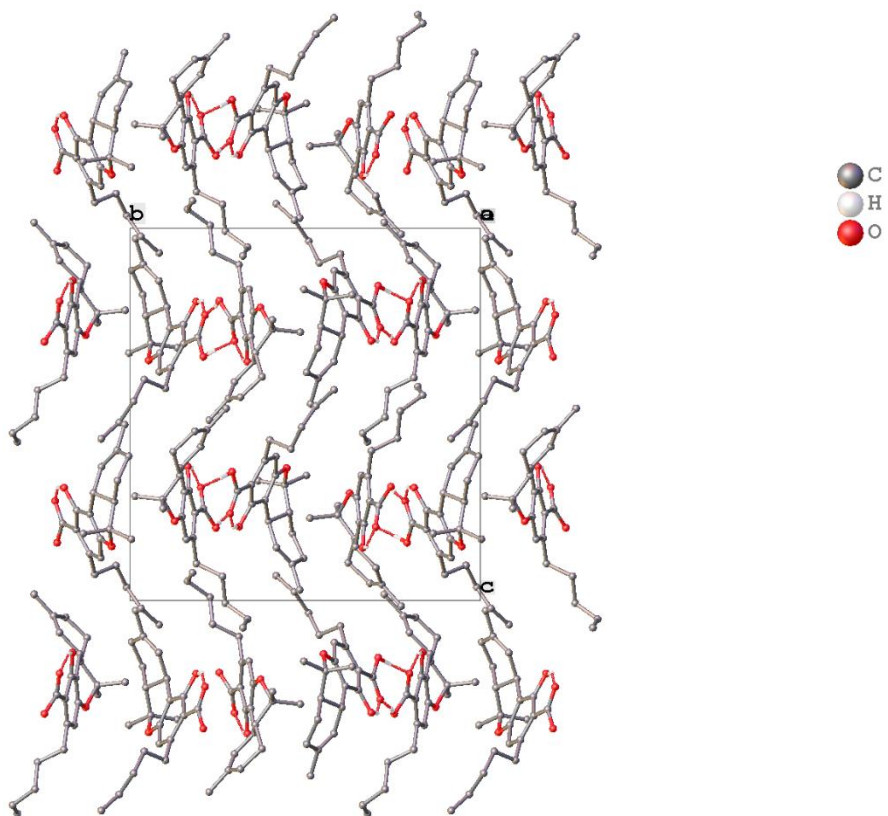


Figure A3.14 WB THCA Crystal XRD packing diagram

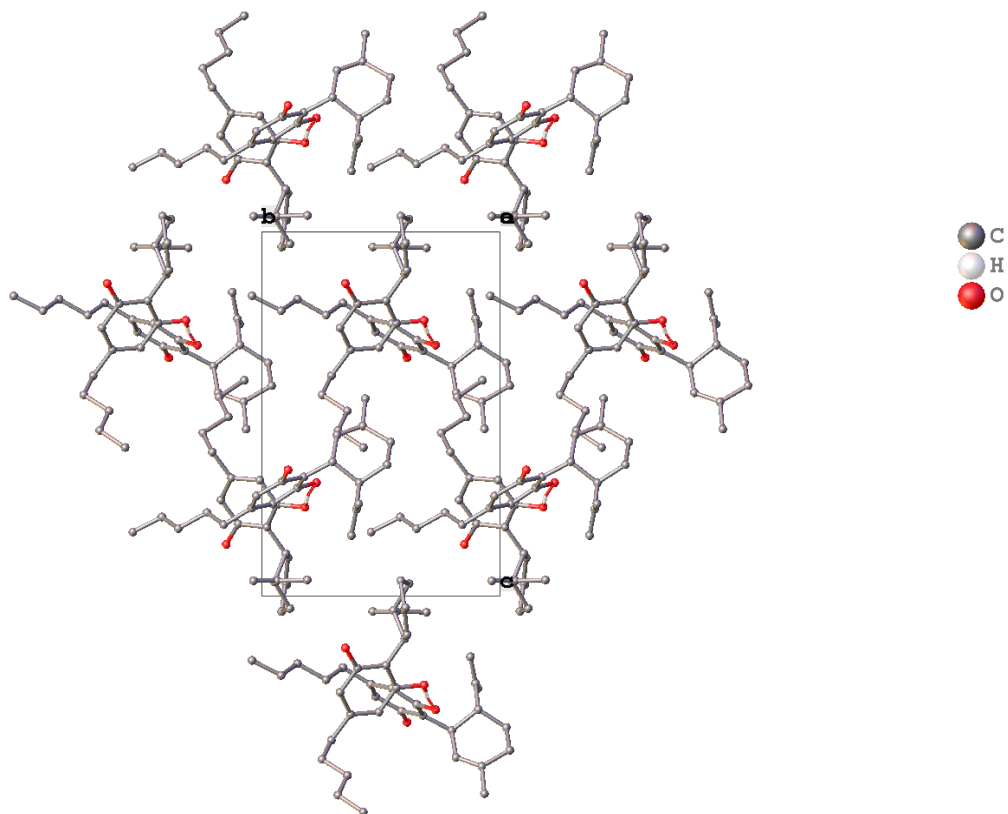


Figure A3.15 CBD Shatter Crystal XRD packing diagram

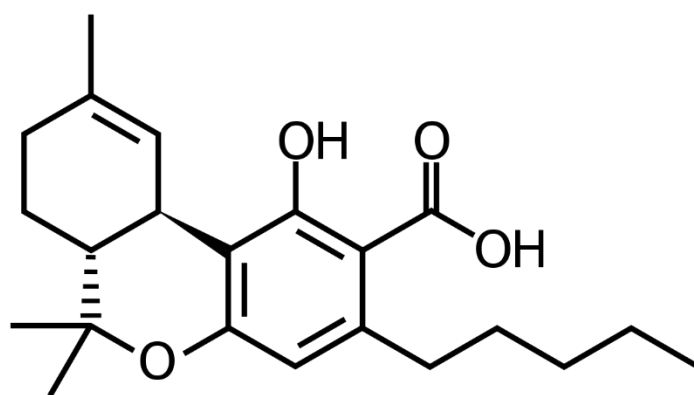


Figure A3.16. THCA chemical structure

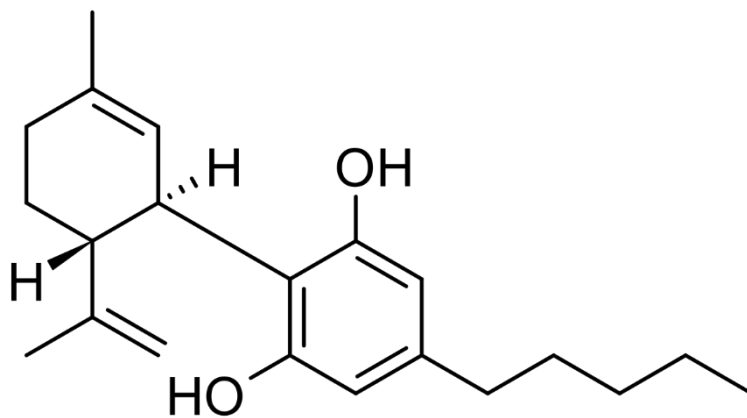


Figure A3.17. CBD chemical structure

REFERENCES

REFERENCES

- (1) Lin, H., Zhang, Y., Wang, Q. et al. (2017). Estimation of the age of human bloodstains under the simulated indoor and outdoor crime scene conditions by ATR-FTIR spectroscopy. *Sci Rep* 7, 13254. <https://doi.org/10.1038>
- (2) Pablo Prego Meleiro & Carmen García-Ruiz (2016) Spectroscopic techniques for the forensic analysis of textile fibers, *Applied Spectroscopy Reviews*, 51:4, 278-301 (3) Maxwell, V.M. (2016). Forensic Examination of Trace Evidence. In *Forensic Science* (eds E. Katz and J. Halánek).
- (3) Daéid, N.N. (2019). Systematic Drug Identification. *Encyclopedia of Analytical Science*, Pages 75-80
- (4) Hughes J, Ayoko G, Collett S, Golding G (2013) Rapid Quantification of Methamphetamine: Using Attenuated Total Reflectance Fourier Transform Infrared Spectroscopy (ATR-FTIR) and Chemometrics. *PLOS ONE* 8(7): e69609.
- (5) Pereira, L. S.A., Lisboa, F. L.C., Neto, J.C., Valladão, F. N., Sena, M. M. (2017). Direct classification of new psychoactive substances in seized blotter papers by ATR-FTIR and multivariate discriminant analysis. *Microchemical Journal*. Volume 133, Pages 96-103.
- (6) González M. Application of Chemometric Tools on Cannabis Samples Analyzed by the FTIR-ATR Method . *Brazilian Journal of Forensic Sciences* 2020;9.
- (7) Bruker Corporation. Differentiation of THC and CBD cannabis using FTIR. Application Note. (Date Accessed 11/23/2020)
- (8) Mainali D. Quick and Real-Time Potency Determination of Cannabinoids Using FTIR Spectroscopy. 2020;
- (9) Trzybiński, D., Niedziałkowski, P., Ossowski, T., Trynda, A., Sikorski, A. Single-crystal X-ray diffraction analysis of designer drugs: Hydrochlorides of metaphedrone and pentedrone. *Forensic Science International*. Volume 232, Issues 1–3. 2013.
- (10) Nycz, J. E., Pazdziorek, T., Malecki, G., Szala, M. Identification and derivatization of selected cathinones by spectroscopic studies. *Forensic Science International*. Volume 266. 2016. Pages 416-426,
- (11) Carlton R.A. *Infrared and Raman Microscopy*. Pharmaceutical Microscopy. 2011.

- (12) Attenuated total reflectance (ATR). Anton Paar Wiki. <https://wiki.anton-paar.com/en/attenuated-total-reflectance-atr/#:~:text=Attenuated total reflectance or ATR,where IR light is reflected.> (accessed Nov 24, 2020).
- (13) Griffiths P.R., de Haseth J. A. (2007). *Fourier Transform Infrared Spectrometry*. New York, USA: John Wiley & Sons.
- (14) Pavan M. V. Barron, R., Barron, A. R., *Physical Methods in Chemistry and Nano Science*. Chapter 8.1., 2019
- (15) Pavan M. V. Barron, R., Barron, A. R., *Physical Methods in Chemistry and Nano Science*. Chapter 8.3.4, 2019
- (16) Putnis, A. (1992). *Introduction to Mineral Sciences*. Cambridge, UK: Cambridge University Press. Chapter 3 (pp. 41-80).
- (17) Cowtan, K. *Phase Problem in X-ray Crystallography, and Its Solution*. Encyclopedia of Life Sciences. 2001.
- (18) Pretsch, E., Bühlmann, P., Affolter, C. *Structure Determination of Organic Compounds*. Springer-Verlag Berlin Heidelberg. Edition 3. 2000.
- (19) Dolomanov, O.V., Bourhis, L.J., Gildea, R.J., Howard, J.A.K. and Puschmann, H. (2009) OLEX2: A Complete Structure Solution, Refinement and Analysis Program. *Journal of Applied Crystallography*, 42, 339-341.
- (20) Sheldrick, G.M. (2015) *Crystal Structure Refinement with SHELXL*. *Acta Crystallographica C*, C71, 3-8.
- (21) The CIF file, refinement details and validation of the structure. CCCW 2011.
- (22) Flack, H.D., On enantiomorph-polarity estimation. *Acta Cryst. A*, 39: 876-881. 1983
- (23) Parsons S, Flack HD, Wagner T. Use of intensity quotients and differences in absolute structure refinement. *Acta Crystallogr B Struct Sci Cryst Eng Mater*. 2013 Jun;69(Pt 3):249-59. doi: 10.1107/S2052519213010014. Epub 2013 May 17. PMID: 23719469; PMCID: PMC3661305.
- (24) Zhang, Tao & Li, Ling & Yang, Haizhao. (2018). 3D\$ Crystal Image Analysis based on Fast Synchrosqueezed Transforms.

4. OPTIMIZATION OF THCA DERIVATIZATION USING AN EXPERIMENTAL DESIGN APPROACH

The necessity for forensic laboratories to not only identify cannabinoids but quantify their potency in marijuana and hemp-based products was prompted by the passing of public law number 115-334 from the Agricultural Improvement Act of 2018 (commonly known as the Farm Bill).¹ Essentially, the passing of the Farm Bill requires differentiation of submitted marijuana samples from hemp based on tetrahydrocannabinol (THC) concentration. This requirement ultimately forced the development of validated methods to quantify THC in samples. Quantification can be performed two ways: through the analysis of both cannabinoid acids and neutrals separately, or through the quantification of “total THC potency.”

Total THC potency analysis combines the concentration of psychoactive THC as well as the non-psychoactive tetrahydrocannabinolic acid (THCA). This method of quantification takes into consideration the fact that THCA is converted to THC through decarboxylation, which occurs naturally over time in marijuana but can also be accelerated by heat. While each cannabinoid acid undergoes decarboxylation to the neutral form over time or upon heating, the focus in this work is the decarboxylation of THCA to THC.

As the requirements for cannabinoid quantification are set by individual states, it may be necessary to identify the entire profile of cannabinoid acids and neutrals. An analytical scheme commonly used for the analysis of marijuana is gas chromatography-mass spectrometry (GC-MS), due to the fact that it satisfies analysis recommendations provided by the Scientific Working Group for the Analysis of Seized Drugs (SWGDRUG). However, the use of GC-MS for the analysis of both cannabinoid acids and neutrals poses a challenge directly related to the aforementioned decarboxylation process. As the injection port of the GC-MS is heated at a

temperature high enough to volatilize samples prior to analysis, this heat readily decarboxylates the sample, resulting in the conversion of all present cannabinoid acids to their neutral counterparts (*e.g.*, THCA to THC). This conversion occurs with a theoretical maximum efficiency of 87.7% conversion, given the ratio of masses between THCA and THC, but literature indicates 65% maximum conversion using the heat of the GC-MS injection port.²

To provide accurate identification and quantification of both the acidic and neutral cannabinoids, recent research has been performed focusing on instrumentation other than GC-MS to avoid the potential for decarboxylation (*e.g.*, liquid chromatography-mass spectrometry).²⁻

⁴ However, due to the prevalence of GC-MS in forensic laboratories, it is advantageous to develop methods through which the structural integrity of the cannabinoid acids can be preserved for identification and quantification. As such, the derivatization of cannabinoid acids prior to GC-MS analysis has been investigated in order to produce a stable product that does not undergo decarboxylation upon injection.⁵⁻⁷

Derivatization is a chemical process through which a thermally unstable, or low volatility compound can be modified with a variety of functional groups to produce a stable structure suitable for analytical analysis by GC-MS. Recent literature has highlighted the use of derivatization for the identification and separation of numerous novel psychoactive substances by GC-MS analysis.⁸ Additionally, derivatization allows for more sensitive detection and accuracy during GC-MS analysis.⁹

While recent literature has focused on the method development and validation of various forms of derivatization specifically for cannabinoid acids, the published methods vary.⁵⁻⁷ Derivatization methods for GC-MS analysis consider multiple factors during their development, including derivatizing agent, support solvents, temperature of reaction, total derivatization time,

and use of a catalyst.¹⁰ Optimization of these parameters, with particular focus on the derivatization of THCA, has not been performed. Due to the unknown interactions between each of the aforementioned derivatization parameters, experimental design procedures can be utilized for method optimization rather than optimizing one parameter at a time. Additionally, recent literature has demonstrated that experimental design methods effectively reduce the overall number of experiments necessary to optimize a set of parameters. Further, these designs provide statistically relevant data regarding the maximum yield of the desired derivatized product relative to the interaction of parameters.¹⁰⁻¹³

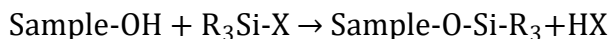
4.1 THEORY

4.1.1 Derivatization Methods

Derivatization of non-volatile or thermally unstable compounds can be performed using a variety of methods. As derivatization relies on the addition of functional groups to the original compound in order to increase volatility and stability, the derivative functional group selected depends on specific functional groups on the compound's structure. Additionally, different reagents can be used depending on the overall goal of derivatization in the specific analysis (*i.e.*, stability, enhanced separation, or chiral separation).⁹ As such, considerations regarding the derivatizing reagent rely both on understanding the structure of the compound of interest as well as the goal for the analysis. Some common functional groups used for addition reactions for derivatization include alkyl or aryl, silyl, acyl, and hetero groups.⁹

Silylation is a commonly used derivatization method for GC-MS analysis. The addition of silyl groups to a compound increases the stability while reducing the polarity, thus improving the volatility and stability of the compound during GC-MS analysis.⁹ Trimethylsilyl (TMS)

reagents produce thermally stable compounds by reacting with active hydrogen atoms. The general chemical reaction for a TMS derivatization is



where X is the silyl compound's leaving group (often containing a halogen), R represents methyl groups, and the Sample-OH can be any variety of active hydrogen functional groups (and can be interchanged with Sample-NH).¹⁴ The rate of silylation for unhindered functional groups regardless of silylating reagent is as follows: alcohol > phenols > carboxylic acids > amines > amides. This can be further refined relative to alcohol and amine location on the structure.

Example structures of select TMS derivatives are provided in **Figure 4.1**.

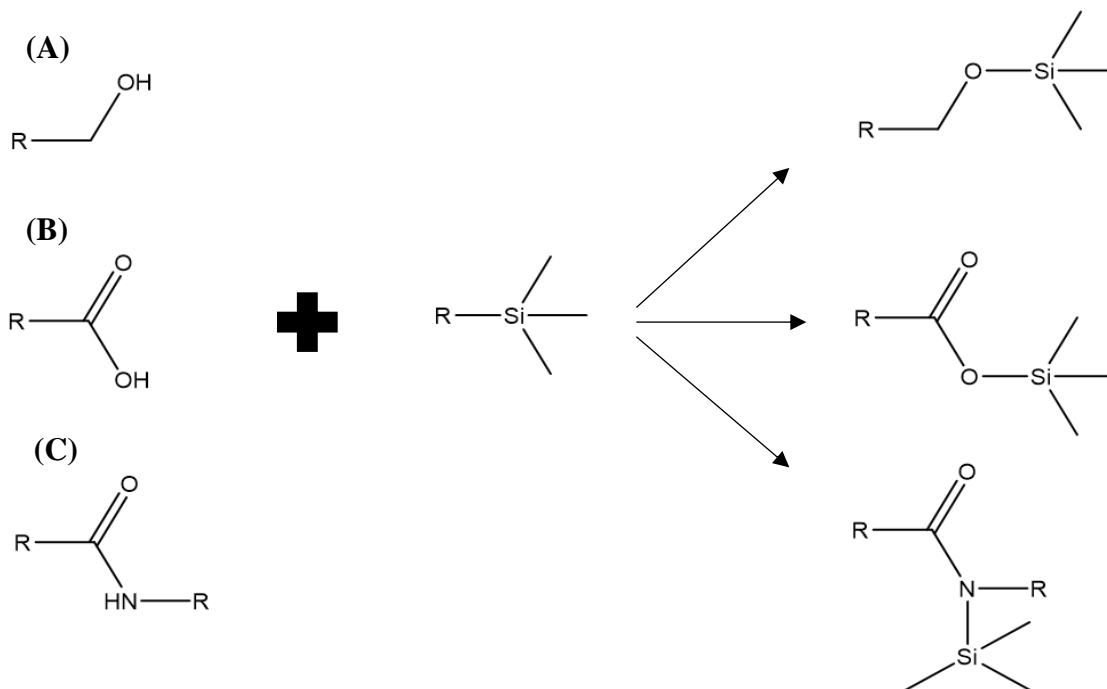


Figure 4.1 Example TMS derivatives: (A) hydroxyl, (B) carboxyl, and (C) amide

N-Methyl-N-(trimethylsilyl)trifluoroacetamide (MSTFA) and N,O-Bis(trimethylsilyl)trifluoroacetamide (BSTFA) are two commonly used silylation reagents. Both

reagents react with most alcohols, phenols, and carboxylic acids; however, BSTFA donates the TMS group more readily to hydroxyl groups than MSTFA does.¹⁴ The addition of low concentration (1%) trimethylchlorosilane (TMCS) to each silylating reagent improves the silylation of hindered functional groups.

Derivatization methods vary related to sample size but are generally simple. Due to the reactivity of silylating reagents with hydroxyl groups, reactions are often performed in anhydrous environments to prevent competitive reactions and the generation of side products.¹³ Additionally, while the silyl reagent may serve as the solvent, a support solvent may also be necessary for complete derivatization. Polar support solvents such as pyridine, dimethylformamide (DMF), and acetonitrile are often used because they can facilitate the silylation reaction. Further, pyridine is commonly used as a support solvent due to the fact that it can act as a catalyst for the reaction as a HCl scavenger, as HCl is a byproduct of the silylation reaction in organosilane reactions.¹⁴

The factors that control the rate and extent of a silylation reaction include silylating reagent, catalyst, use of support solvent, temperature of the reaction, and the time for the reaction. Heating may be necessary for some derivatization reactions if the reaction occurs slowly at room temperature. Determining the optimal parameters necessary for efficient and reproducible derivatization can be performed by varying one variable at a time while maintaining the additional variables at fixed values. While this approach is traditionally used, it can result in a large number of acceptable parameters for the derivatization of one compound, due to a reduced number of overall factors taken into consideration and the inability to study the influence of multiple factor interactions. Experimental design methods, however, allow for the observation of

the effect of multiple changing factors and interactions at the same time, reducing the overall number of experiments necessary for optimization of the derivatization method.

4.1.2 Experimental Design

Experimental design procedures are often employed to determine the statistical significance of factors in a reaction, method, or procedure. Experimental designs are useful in not only identifying significant factors for a procedure, but also can optimize those factors while improving the overall robustness of the method.¹⁰ The optimization of a method with multiple factors can be achieved more efficiently through experimental design approaches when compared to traditional single-factor analyses.

Considerations that are made when performing experimental design experiments include the number of factors studied, the range over which the factors will be adjusted (referred to as levels), and the appropriate response variable. An example of an experimental design would be a three-factor, two-level design, where pre-determined high and low levels of each factor are used during experimentation. For example, a derivatization procedure can be investigated by experimental design by comparing the effect of reaction temperature, derivatization time, and derivatization reagent to solvent ratio at high and low levels on the abundance of the resultant derivatized product (the response variable). The derivatization experiments can be planned and randomized such that experimenter bias is removed. Additionally, if the experiments cannot all be performed on the same day, due to length of analysis or other variables, the design can be “blocked” into smaller segments. Blocked experiments take into account not only the parameters outlined in the experimental design, but also differences between days in the data analysis (allowing for temperature and humidity of the laboratory to be taken into account).

Introducing blocks into the derivatization experimental designs inherently introduces confounding of factor and interaction impact on the response variable (derivatized product abundance). Confounding can also occur in designs that are not blocked, based on the number of total experiments performed and the ability to separate the effects of the factors and interactions on the response variable during data analysis. Confounding prevents complete understanding of the significance of separate factors and interactions.¹⁵ When two variables are confounded, such as the reaction temperature factor and the interaction between reaction temperature and reaction time, the effect they have on the derivatized product abundance cannot be differentiated. In this case of confounding, an increase in derivatized product abundance cannot be attributed to only the reaction temperature nor the interaction between temperature and time, but to both the factor and the interaction, effectively reducing the ability to fully characterize the reaction. As such, confounding limits the overall usefulness of the experimental design data.¹⁶

The extent of confounding in an experimental design can be described by the design resolution. Resolution of an experimental design is generally portrayed by considering the lowest order of interactions (using letters to represent the factors) in the defining relation of the design.¹⁶ Defining relations are created in fractional factorial or blocked full factorial designs to show the combination constant factors capable of defining the experimental design. The defining relation can be used to determine which factors are confounded by multiplying the factor or interaction of interest by the defining relation. In order to separate the main factor effects from each other (necessary for any useful experimental design), the defining relationship must be represented as $I = ABC$. This defining relation indicates a resolution III design, related to the minimum number of factors in the defining relation. This method for determining resolutions for experimental designs gives rise to three general resolutions - III, IV, and V. While resolution II is technically

possible, this would indicate that the main factors effects are confounded with each other (I = AB) and would not be useful in characterizing the procedure. As resolution number increases, the confounding between factors and interactions decreases such that Resolution III provides the least design characterization and Resolution V provides the most. **Table 4.1** summarizes the confounding of a design present at each resolution level.

Table 4.1 Summary of Resolution and Confounding Variables

Confounding	Resolution III	Resolution IV	Resolution V
Main effects with each other	-	-	-
Main effects are with two-factor interaction	X	-	-
Main effects with three-factor interactions	N/A	X	-
Two-factor interactions with each other	N/A	X	-
Two-factor interactions with three-factor interactions	N/A	N/A	X

4.1.2.1 Full Factorial Screening Design

Screening designs are often utilized as the first round of an experimental design procedure and provide the opportunity to determine significant factors in a method or procedure. There are a variety of screening designs available, including full factorial, fractional factorial, and Plackett-Burman designs.¹⁷ Full factorial designs provide the most insight related to parameter and interaction effects on the response variable with no confounding present (unless

blocked experiments are performed), while each of the latter designs confound the parameters and interactions to some degree.

Full factorial screening designs limit the number of experiments being performed based on Equation 4.1:

$$E=K^N \quad (4.1)$$

In Equation 4.1, E represents the total number of experiments, K is the number of level, and N represents the number of factors. For example, the two-level, three-factor experimental design to optimize a derivatization procedure requires eight experiments to complete the full factorial. The design of such a full factorial experiment would follow **Table 4.2**, where +1 represents the high value for a level and -1 represents the low value for a level.

Table 4.2 Example of Experimental Order for Full Factorial Design with Three Factors

Experiment Order	Factor A	Factor B	Factor C
1	+1	+1	+1
2	+1	+1	-1
3	+1	-1	+1
4	-1	+1	+1
5	+1	-1	-1
6	-1	+1	-1
7	-1	-1	+1
8	-1	-1	-1

The positive and negative level values in **Table 4.2** represent pre-determined high and low experimental values based on knowledge of the reaction or method being studied. For

example, in the context of this work, factor A represents the time of a reaction, with +1 equal to 60 minutes, while -1 is equal to 10 minutes. Factor B represents the temperature of a reaction with a high value of 100 °C and a low value of 30 °C. Finally, factor C is the ratio of a solution with a high value of 90:10 and a low value of 50:50. Following the experimental order in **Table 4.2**, experiment four would be performed for 10 minutes at 100°C with a solution ratio of 90:10.

Following the completion of the full factorial screening design experiments, linear regression mathematical models are used to determine the sources of significant variation in the response variable. When analyzing the response of one variable against multiple factors, analysis of variance (ANOVA) can be utilized to determine statistically significant factors and interactions. Statistical analysis by ANOVA determines significance of factors by comparing variation of the response variable due to random error against the variation caused by changing an experimental factor.

In order to determine significant variables by ANOVA first the “sum of squares” (SS) is calculated between each experimental factor mean and the overall mean. Additionally, the SS is calculated for the error and for the design as a whole. Next, the total degrees of freedom are calculated as well as degrees of freedom for each factor and error. Following this, the mean sum of squares (MS) are calculated to measure the variation explained by the factors and model assuming that all other factors are in the model. Finally, an *F*-value is calculated for each test, which is further used to calculate the *p*-value used to determine statistical significance. If the *p*-value for the model is less than the significance level set for analysis, then the model explains the variation in the response variable. Similarly, if the *p*-value for a particular factor studied in the design is less than the significance level it causes significant variability in the response variable. The equations used for ANOVA calculations are provided in Appendix IV.

4.1.3 Gas Chromatography-Mass Spectrometry

GC-MS is a hyphenated, two-part technique which combines chromatographic separation (GC) with spectrometric analysis (MS) for the separation, characterization, and identification of volatile samples. The general components of a GC include a heated injection port, a capillary chromatography column, and an oven which houses the column. Following injection *via* the GC injection port and volatilization of the sample, an inert carrier gas (such as He, H₂, or N₂) moves the samples through the GC column at a pre-determined flow rate (*e.g.*, 1 mL/min). As sample mixture move through the column, the individual analytes are separated by both their boiling points and chemical interaction with the stationary phase, resulting in more volatile analytes travelling more quickly through the column than less volatile analytes. The end of the GC column is connected to a detector (in this case a MS) which distinguishes the components of the mixture from each other. The total time taken for the analyte to travel through the column to the detector is the retention time.¹⁸

A mass spectrometer functions as the detector in GC-MS. The MS and GC are connected by a heated transfer line such that the volatile compounds leaving the GC do not condense prior to MS analysis. Mass spectrometers generally consist of three components: an ion source, a mass analyzer, and an ion detector. Though there are many variations of mass spectrometers on the market, in benchtop instruments that are common in forensic laboratories, an electron ionization source, single-quadrupole mass analyzer, and electron multiplier detector are used. As mass spectrometers identify and separate charged fragments, ionization must occur prior to detection. In EI, a heated filament emits high-energy electrons (commonly 70 eV) that bombard the gas-phase analyte exiting the GC column. The use of 70 eV for bombardment provides sufficient energy to break bonds in organic molecules and ensures reproducible compound fragmentation.

The interaction between the electrons in the EI source and the analyte causes fragmentation while also inducing a net positive charge due to the loss of electrons during fragmentation. From this, positively charged fragments continue through the mass spectrometer, while neutral loss fragments are not detected.

Next, the charged fragments are separated using a quadrupole mass analyzer, which consists of four parallel molybdenum rods with oscillating radio frequency (RF) and DC voltage. The oscillation of voltages between the metal rods provides the ability to separate ions according to their mass over charge (m/z) ratios.¹⁸ The path of a charged fragment through the quadrupole is determined by the sweeping of RF and DC voltages. Specific RF and DC voltages are used to separate the fragment ions because ions have stable oscillations only within particular values of voltages applied. For example, if the voltages currently applied to the quadrupole allow an ion with an m/z equal to 55 to oscillate through to the detector, an ion with an m/z of 155 would not be stable and its oscillating path would cause the ion to be neutralized by the quadrupole and pumped away by the vacuum system.

The ions separated by the mass analyzer are then detected by an electron multiplier. Ions are detected by the electron multiplier through a secondary emission process, in which the detected ion produces a cascade of secondary electrons that are collected by a metal anode and converted to a computable signal. The separation of m/z values and their detection by an electron multiplier allows for the creation of a mass spectrum providing the m/z values and their associated intensities.¹⁸ The resultant mass spectrum can then be analyzed for abundant fragments and compared to commercially available library spectra such as the National Institute of Standards and Technology (NIST) EI mass spectral library. Further, more confident

identification of the analyte is performed by comparing the resultant mass spectrum to that of a certified reference material analyzed under similar conditions as recommended by SWGDRUG.

4.2 MATERIALS AND METHODS

4.2.1 Reference Materials and Sample Preparation

Pre-screening and full factorial screening design experiments were performed using THCA certified reference material (CRM) from Cayman Chemical (Ann Arbor, MI). Solvents used throughout the pre-screening and full factorial screening design experiments included ethyl acetate (99.7% pure, HPLC grade, Millipore Sigma, Burlington, MA), pyridine (>99.9% pure, ACS grade, Sigma-Aldrich, St. Louis, MO), and BSTFA-1% TMCS (Supelco Analytical, Bellefonte, PA). The THCA CRM was prepared at 0.1 mg/mL in methanol (ACS grade, VWR Chemicals BDH®, Radnor, PA). The internal standard utilized was progesterone ($\geq 99\%$, Sigma-Aldrich) which was prepared at 0.9 mg/mL in both ethyl acetate and pyridine solutions and added to the samples following derivatization at a final concentration of 0.3 mg/mL.

All THCA CRM samples were prepared for derivatization by pipetting 150 μL of the 0.1mg/mL THCA into a GC-MS vial fit with a 250 μL glass insert (Agilent Technologies, Santa Clara, CA). The THCA CRM solution was dried down under house nitrogen to constant mass to create an anhydrous environment for the derivatization reaction.

A general derivatization method (provided by Restek)⁵ was utilized and acted as the framework by which the full factorial experiment derivatizations were modified. The dried THCA CRM was reconstituted with 50 μL ethyl acetate (Millipore Sigma) and 50 μL BSTFA-1% TMCS (Supelco Analytical). The sample was heated for 30 min at 70 °C, then allowed to

cool to room temperature prior to GC-MS analysis. Progesterone internal standard (0.9mg/mL) was added to the sample before GC-MS analysis in an additional 50 μ L aliquot of ethyl acetate.

Initial experiments were performed prior to the full factorial screening design using the Restek derivatization method.⁵ These experiments investigated appropriate support solvents for the derivatization as well as derivatized sample hold conditions prior to GC-MS analysis. A summary of the pre-screening experiments is provided in the appendix. From these experiments, pyridine was selected as an additional support solvent based on the abundance of derivatized THCA (THCA-2TMS) and reproducibility between and within derivatizations. Further, refrigeration was selected as a suitable sample hold environment based on reproducibility and feasibility. Moving forward, both ethyl acetate and pyridine were considered as support solvent through the experimental design.

4.2.2 Full Factorial Screening Experiments

Focusing only on the derivatization of a 0.1mg/mL THCA CRM sample, the silylation reaction was characterized for significant factors. Specifically, the factors investigated for optimization included temperature of reaction, total reaction time at temperature, and the ratio between BSTFA-TMCS reagent and the secondary solvent (either pyridine or ethyl acetate). Full factorial analysis was selected as both main factor and interactions between factors could be investigated for their significance on the overall abundance of the THCA-2TMS product.

The high and low levels for the full factorial parameters were selected as the extreme values at which the derivatization would move forward. The levels for the temperature of reaction were chosen considering the necessity of heat for the derivatization of THCA (based on

prior experimentation), as well as the thermal instability of THCA. As such, the lowest temperature of 30 °C was selected to provide the lowest, controllable temperature comparable to room temperature. The highest temperature was selected as 100 °C to minimize sample decarboxylation.² The total derivatization time was selected based on previous experimentation and with regard to the thermal instability of THCA over time. Prior experimentation using the Restek method indicated that immediate derivatization (less than 5 minutes total reaction time prior to sample injection) produced little to no derivatized sample and with low reproducibility. Noting that, 10 minutes was used as the shortest reaction time to provide reproducible reactions using both pyridine and ethyl acetate as support solvents, while 60 minutes ensured little decarboxylation, even in combination with the high temperature level (100 °C). Finally, the levels used for solvent ratio were selected with the knowledge that excess BSTFA-TMCS derivatizing reagent is necessary for full, reproducible derivatizations, as well as the necessity for a support solvent for the formation of the THCA-2TMS product. **Table 4.3** summarizes the high, low, and center values for these factors.

Table 4.3 Full Factorial Levels for Each Factor

Factor	Level 1 (-)	Level 2 (+)	Center Point (0)
Time (min)	10	60	35
Temperature (°C)	30	100	65
BSTFA : Solvent	50 : 50	90 : 10	70 : 30

The experimental order was designed and randomized using Minitab (Minitab, LLC, State College, Pennsylvania). A total of 24 experiments were designed in which the support solvent was pyridine, allowing for the entire full factorial design to be repeated twice. These experiments were broken up into four blocks of six experiments each comprising of four different factorial experiments and two center point experiments per block. Blocks were

analyzed on sequential days. This design resulted in a resolution IV experimental design, capable of providing sufficient characterization information for the experimental protocol. A full table of design order and factor values can be found in **Section 4.4.1**.

An additional full factorial screening design was performed in which ethyl acetate was used as the support solvent. This was completed in 12 total experiments using the same levels and factors as outlined in **Table 4.3**. The experiment was broken into two blocks of 6 experiments each comprising of four different factorial experiments and two center point experiments per block. The experiments performed mimic blocks one and two of the pyridine support solvent full factorial analysis.

Following full factorial analysis, the derivatization method using pyridine as the support solvent was optimized to provide the following method: The dried THCA CRM was reconstituted with 50 μL pyridine (Sigma-Aldrich) and 50 μL BSTFA-1% TMCS (Supelco Analytical). The sample was heated for 10 min at 65 $^{\circ}\text{C}$, then allowed to cool in the refrigerator prior to GC-MS analysis. Progesterone internal standard (0.9mg/mL) was added to the sample before GC-MS analysis in an additional 50 μL aliquot of pyridine.

4.2.2.1 Sample Preparation - THCA Concentration Study

A range of THCA concentrations was derivatized using the optimized method in order to demonstrate method linearity. The concentrations included in this study were: 10 $\mu\text{g}/\text{mL}$, 50 $\mu\text{g}/\text{mL}$, 0.1 mg/mL, 0.25 mg/mL, and 0.5 mg/mL. Samples at each concentration level were derivatized using the optimized method as determined through the full factorial screening

experiments in triplicate vial to assess the reproducibility of the method both between and within sample vials in terms of RSD.

4.2.2.2 Sample Preparation – Cannabis Extract Sample Analysis

A subset of three cannabis solvent extract samples was subjected to derivatization by the optimized method and analysis by GC-MS. These samples included two THCA-containing samples, case sample KDPS 18-9026 and Skymint sample WB THCA crystals. Additionally, the CBD Crystal sample was derivatized using the optimized method to show the suitability of this derivatization method for cannabinoids other than THCA. For each solvent extract sample, a 1mg/mL solution of crystalline material was prepared in methanol and the sample was diluted by one-third for derivatization (50 μ L evaporated to dryness as opposed to 150 μ L). Each sample was derivatized in triplicate to evaluate the reproducibility of the derivatization given any matrix effects present in the samples (additional cannabinoids or wax component).

4.2.3 GC-MS Analysis

All derivatized samples were analyzed by GC-MS using an Agilent Technologies 7890A GC and 5975C MS equipped with an autosampler (all Agilent Technologies). The GC injection port was set at 280 °C and a 1 μ L aliquot of sample was injected with a 25:1 split ratio. Ultra-high purity helium (Air Gas, Radnor, PA) was used as the carrier gas at a nominal flow rate of 1.5 mL/min. The GC was equipped with a 5% diphenyl-95% dimethyl polysiloxane column (30 m x 0.25 mm x 0.25 μ m, Agilent Technologies). The oven temperature was held at 40 °C for 1 min, then ramped to 280 °C at 12 °C/min with a final hold for 3 min. The mass spectrometer

was operated in electron ionization mode (70 eV), with a scan range from 30 – 750 amu, and a scan rate of 2.00 scans/sec. The ion source and quadrupole were heated to 230 °C and 150 °C, respectively. Each sample was analyzed in triplicate.

4.2.4 Data Processing and Analysis

The chromatographic abundances for each derivatized sample were collected and exported from ChemStation (version E.01.00.237, Agilent Technologies) to Microsoft Excel (version 16.0, Microsoft Corporation, Redmond, WA). The chromatographic abundances were normalized to the abundance of the progesterone internal standard. Additionally, averaged chromatograms were produced by averaging the normalized chromatographic abundances to accurately represent chromatographic abundances of derivatized products within one derivatized sample as well as between triplicate derivatizations. The reproducibility of peaks was evaluated based on the relative standard deviation (RSD) of the peak abundance of the derivatized product (THCA-2TMS or THC-TMS) within and between derivatizations.

4.2.4.1 Full Factorial Analysis

All full factorial analysis was performed using Minitab software (Minitab®, version 19.2020.1 (64-bit), State College, PA) The averaged, normalized abundance of the THCA-2TMS chromatographic peak for each experiment was input relative to the experiment number for each screening design. The full factorial analysis function was utilized, with a two-sided confidence level set to 95. The Minitab software provides multiple tables and plots for additional analysis, including the coded coefficients table, ANOVA table, Pareto chart of standardized effects, and

multiple residual plots. Significant factors were determined based on the ANOVA output, while the additional table and plots were used for supporting information.

4.3 FULL FACTORIAL SCREENING EXPERIMENT RESULTS AND DISCUSSION

Using the derivatization method outlined in Section 4.2.1.3, the THCA CRM was derivatized, using both ethyl acetate and pyridine as support solvents, and characterized by GC-MS. **Figure 4.2** provides an overlay of averaged chromatograms from both the ethyl acetate and pyridine derivatizations. Derivatizations were performed in triplicate using ethyl acetate and pyridine as support solvents.

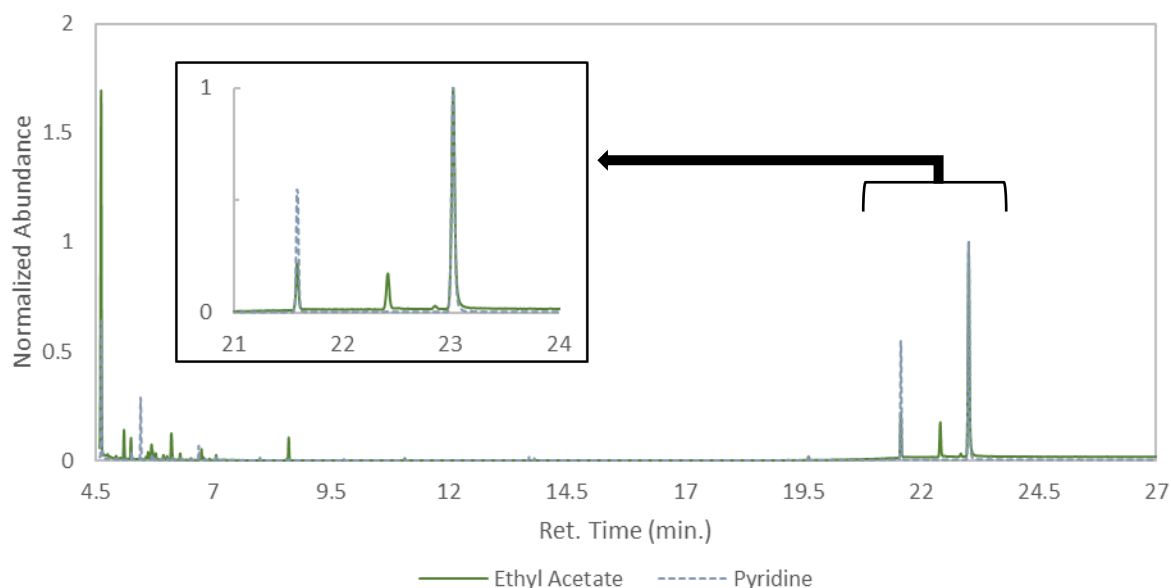


Figure 4.2 Averaged chromatograms of THCA derivatizations using ethyl acetate and pyridine

The peaks of interest regarding the derivatization of THCA are between retention times (t_R) 21 and 24 min. Derivatizations performed using pyridine or ethyl acetate as the support solvent displayed similar chromatographic peaks ($t_R = 21.6$ min and $t_R = 23.0$ min), however

ethyl acetate-supported derivatizations also include a third peak ($t_R = 22.4$ min). The peak present at $t_R = 21.6$ min is the THCA-2TMS product while the peak at $t_R = 22.4$ min is consistent with a THC-TMS product (derivatized THC, not THCA). Finally, the progesterone internal standard was present at $t_R = 23.0$ min. The early eluting peaks in the chromatogram (between t_R 4.5 – 9.5 min) are BSTFA-TMCS solvent fragments, including single TMS groups and those bound to alkyl groups not associated with the THCA-2TMS ($t_R = 21.6$ min), as well as various siloxane peaks from the GC-MS inlet and stationary phase.

Peaks at the listed retention times were identified using their associated mass spectrum. The mass spectra and chemical structure for THCA-2TMS ($t_R = 21.6$ min) is provided in **Figure 4.3**. Though mass spectral library searches are generally used to presumptively identify an unknown analyte, the mass spectrum of THCA-2TMS was not included in the NIST mass spectral library used in this work. As such, identification of the THCA-2TMS product peak was accomplished through structural elucidation based on fragment ions present in the mass spectrum. The molecular ion peak at m/z 502.3 for THCA-2TMS is present at low abundance in the mass spectrum. The accompanying base peak at m/z 487.4 represents the loss of one methyl group from the silylated compound. The THCA-2TMS mass spectrum does not display many high abundance fragment ions, which is expected due to the stability of the compound following derivatization. The next highest abundance ion is m/z 73.1 which is representative of a single TMS group (molecular weight = 73.2). The presence of this peak is indicative of a derivatized sample but cannot be used toward the identification of the cannabinoid structure, as it is not unique to a specific compound's derivatization.

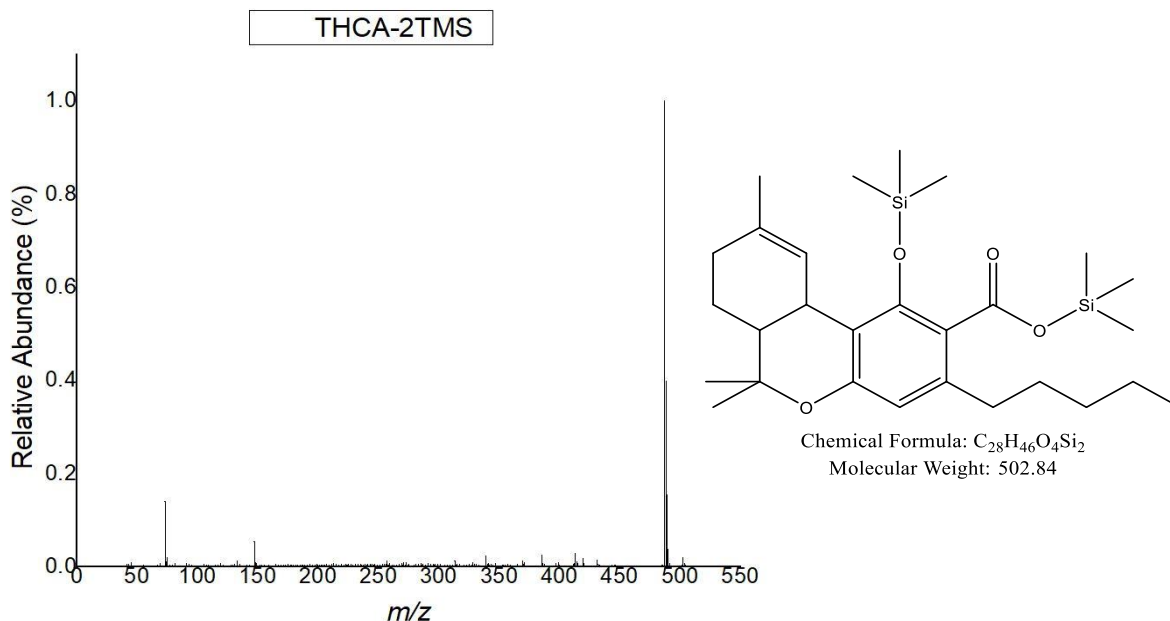


Figure 4.3 Mass spectrum and chemical structure of THCA-2TMS

The mass spectrum of THC-TMS ($t_R = 22.4$ min) and chemical structure are provided by **Figure 4.4**. Presumptive identification was performed using a mass spectral library search. The experimental mass spectrum for THC-TMS includes high abundance background ions in the range m/z 150 - 200, which are not present in the NIST library spectrum (Appendix IV). However, these background ions are instrument- rather than compound-specific and correspond to polysiloxanes commonly found in the column stationary phase or injection port septum. In spite of the high abundance background, identification of the peak as THC-TMS was possible due to ions characteristic of the derivatized product, including the high abundance molecular ion (m/z 386.3). Additionally, the high abundance fragment at m/z 371.3 represents the loss of a methyl group from the derivatized structure. Finally, the characteristic single TMS fragment peak is present at m/z 73.1, indicating a derivatized sample.

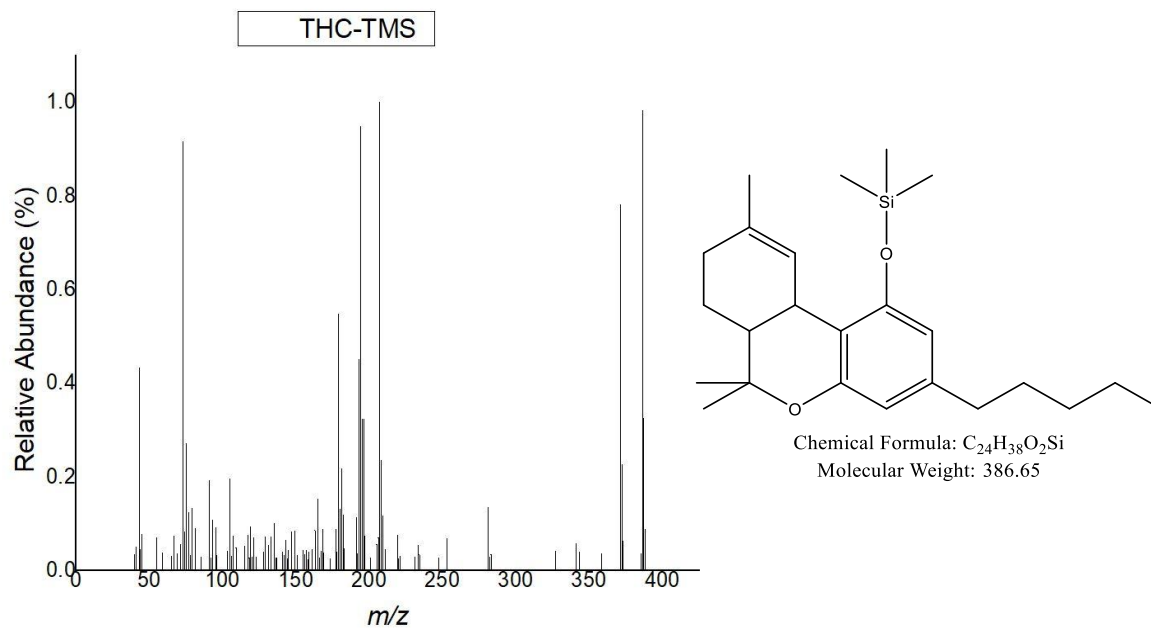


Figure 4.4 Mass spectrum and chemical structure of THC-TMS

Each of these high abundance peaks are present in the library mass spectrum; however, lower abundance peaks from the library mass spectrum are not present in the experimental spectrum. The lack of lower abundance ions as well as the inclusion of high abundance background ions correspond to the low chromatographic abundance of the THC-TMS peak. Despite these features, this peak can be presumptively identified as THC-TMS. A representative mass spectrum for THC (underivatized) is also provided in Appendix IV.

The presence of underivatized THCA in the form of THC-TMS in the ethyl acetate derivatizations indicates an inefficient derivatization method. This product may be produced by the decarboxylation of remaining THCA in the injection port of the GC-MS and immediate derivatization with remaining BSTFA-TMCS, though this was not specifically studied in this work. Additionally, the formation of this derivative may provide insight related to preferred derivatization of the THCA molecule, given that BSTFA-TMCS is known to react with hydroxyl groups more readily than carbonyl groups. This additional peak is not present in any

derivatization using pyridine as the secondary solvent, possibly indicating full derivatization of the THCA during the reaction time in the oven.

4.3.1 Full Factorial Screening Design Experiments and Optimization

A duplicated full factorial screening design was used to characterize the significant parameters of THCA derivatization using pyridine as the support solvent. This resulted in a total of 24 experiments, including center point and factorial experiments. Ethyl acetate supported derivatizations were also characterized using an unduplicated full factorial design, consisting of 12 experiments which followed the order of the first two blocks of the pyridine study. Following each derivatization, the samples were analyzed by GC-MS and the peak abundance for the THCA-2TMS peak was averaged across triplicate instrument injection for each derivatized sample. The full list of experiments and averaged THCA-2TMS normalized peak abundances and RSDs are summarized in **Table 4.6**.

Table 4.6 Summary of experiment order, levels, averaged THCA-2TMS abundance, and RSD

Order	Block	Factors			Pyridine		Ethyl Acetate	
		Time (min.)	Temp. (°C)	BSTFA: Solvent	Abundance (normalized)	% RSD	Abundance (normalized)	% RSD
1	1	60	30	90:10	0.6844	5.3	0.2374	4.4
2	1	10	100	90:10	0.7403	4.8	0.5229	5.6
3*	1	35	65	70:30	0.8219	2.5	0.4428	7.3
4*	1	35	65	70:30	0.6883	2.9	0.4400	5.2
5	1	60	100	50:50	0.7394	1.8	0.7328	2.5
6	1	10	30	50:50	0.2849	2.5	0.1527	4.5
7	4	10	100	50:50	0.6906	2.8	0.6846	1.3
8*	4	35	65	70:30	0.5802	5.7	0.6807	3.2
9	4	10	30	90:10	0.5275	7.1	0.2732	16.1
10	4	60	30	50:50	0.5977	2.6	0.5154	9.4
11*	4	35	65	70:30	0.6698	4.3	0.5758	5.7
12	4	60	100	90:10	0.7986	7.9	0.8035	4.5
13	2	60	30	50:50	0.5993	1.0	-	-
14	2	60	100	90:10	0.8053	2.0	-	-
15*	2	35	65	70:30	0.7568	1.3	-	-
16*	2	35	65	70:30	0.6893	7.0	-	-
17	2	10	30	90:10	0.6296	10.1	-	-
18	2	10	100	50:50	0.8598	6.9	-	-
19	3	10	30	50:50	0.6580	5.9	-	-
20*	3	35	65	70:30	0.7902	5.4	-	-
21	3	10	100	90:10	0.8008	6.1	-	-
22	3	60	100	50:50	0.8114	6.8	-	-
23*	3	35	65	70:30	0.6434	3.6	-	-
24	3	60	30	90:10	0.7138	1.2	-	-

* denotes a center point analysis

Both the pyridine and ethyl acetate supported derivatizations provided reproducible THCA-2TMS production, with nearly all derivatizations resulting in THCA-2TMS peak abundances under 10% RSD. The outliers from this trend included experiment number 17 for the pyridine supported derivatizations and experiment number 9 for ethyl acetate. Both of these experiments were performed under similar conditions, with a 10-minute reaction time, at 30 °C, and with a 90:10 reagent:solvent ratio. Despite the similar reaction conditions, the overall

abundance of THCA-2TMS in the pyridine experiment was significantly higher than the THCA-2TMS abundance in the ethyl acetate experiment ($\alpha = 0.05$, $p = 0.003$). The increased THCA-2TMS abundance for pyridine supported derivatizations as compared to ethyl acetate holds true for a majority of the experiments, with the exception of experiment numbers 8 and 12. Statistical analysis of means ($\alpha = 0.05$), however, concluded that the average THCA-2TMS abundances from either experiment were not statistically different ($p = 0.103$, $p = 0.950$).

Figure 4.5 provides an overlay of the representative chromatograms from derivatizations using the lowest, highest, and center point levels for each of the three factors considered for the pyridine design [*e.g.*, low indicates 10-min reaction time, 30 °C reaction temperature, and a 50:50 (BSTFA : solvent) ratio]. These chromatograms were averaged between the two replicate factorial analyses, while the center point chromatogram is the average of all center point analyses. Similarly, **Figure 4.6** displays an overlay of the chromatograms at low, high, and center point levels from the ethyl acetate supported derivatizations. Refer to **Table 4.3** for the values of each factor at a given level.

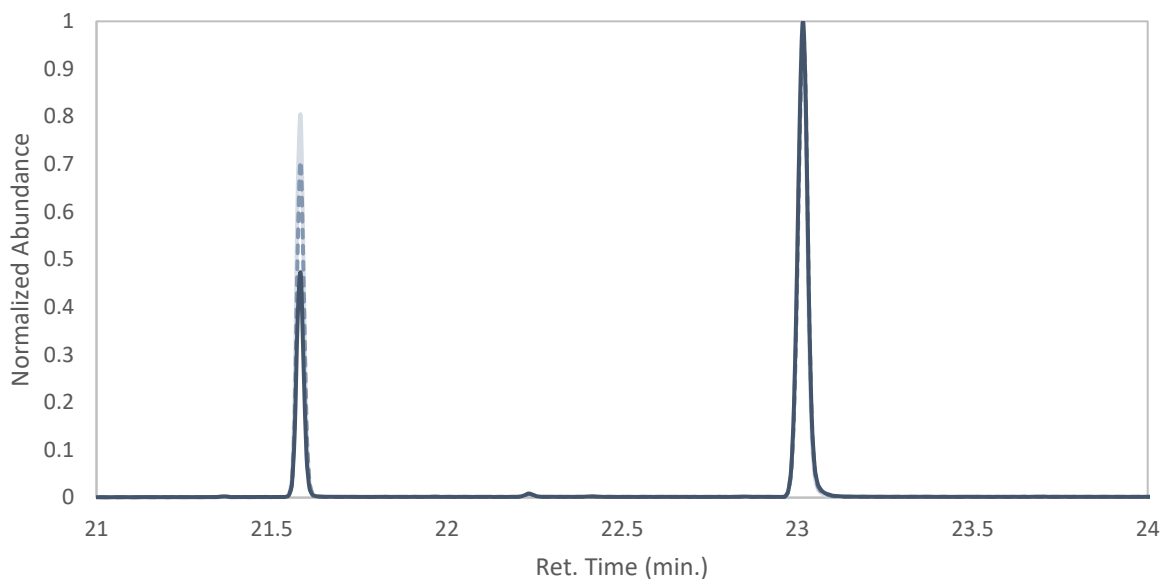


Figure 4.5 Overlay of averaged chromatograms from low (dark blue), high (light blue), and center point (dashed) level pyridine supported derivatizations.

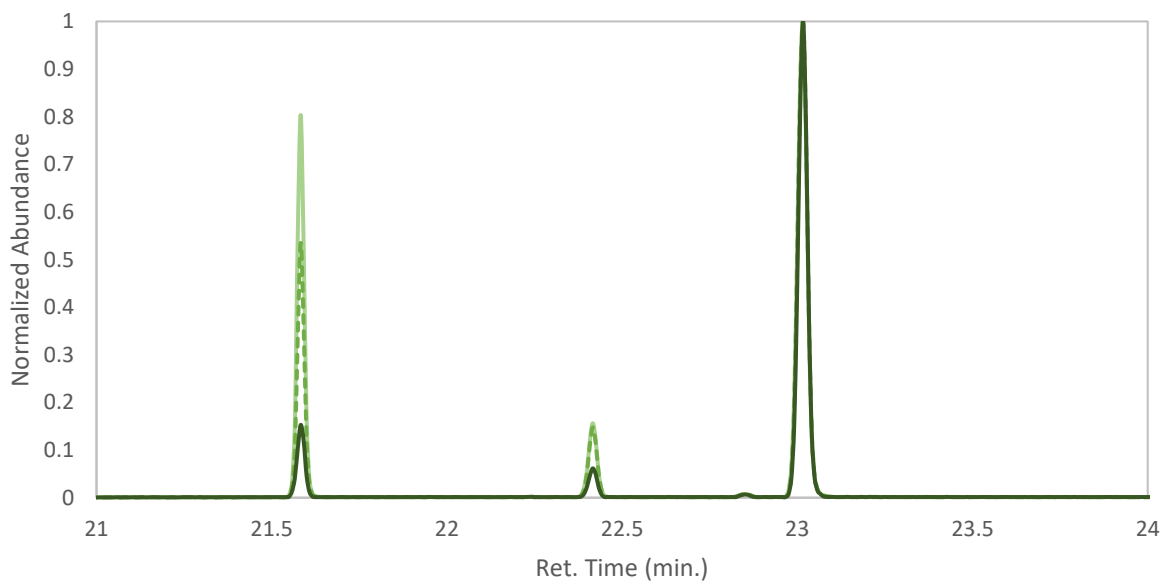


Figure 4.6 Overlay of averaged chromatograms from low (dark green), high (light green), and center point (dashed) level ethyl acetate supported derivatizations

As shown from **Figure 4.5 and 4.6**, the significant peaks present in chromatograms from derivatizations using either support solvent reflect that of the initial chromatograms provided in **Figure 4.2**. Regardless of factor level for each experiment, the derivatization using ethyl acetate continued to include underivatized THCA, represented in the chromatogram as THC-TMS ($t_R = 22.4$ min). Conversely, the derivatizations using pyridine contained only THCA-2TMS.

For each full factorial analysis, ANOVA calculations were performed at the 95% confidence level ($\alpha = 0.05$). For the derivatizations using pyridine as a support solvent, derivatization temperature was the single significant factor ($p = 0.001$) of the three factors studied. Conversely, for the ethyl acetate supported derivatizations both temperature of reaction ($p = 0.000$) and time at temperature ($p = 0.003$) were significant to the variability of the THCA-2TMS product abundance. ANOVA tables for both full factorial experiments, as well as Pareto charts of standardized effects are provided in Appendix IV.

Given the reduced number of significant variables determined for derivatizations using pyridine as the support solvent, as well as the full derivatization of THCA, final derivatization optimization experiments were performed using pyridine rather than ethyl acetate as the support solvent. When performing optimization experiments, time and solvent ratio were held constant, while the temperature of reaction was varied between the low, center point, and high levels used for the full factorial analysis. A reaction time of 10 min was selected, as increasing the total time of reaction was not significant to THCA-2TMS production, nor did a reduced reaction time significantly impact the reproducibility of THCA-2TMS abundance in the screening design experiments. A 50:50 ratio of BSTFA:pyridine was used during optimization, as it provided the most support solvent to act as a derivatization catalyst while maintaining an excess of BSTFA, and offered lower RSD values when compared to the 90:10 ratio experiments at each time and

temperature level. Temperature was varied between 30 °C, 65 °C, and 100 °C to reflect the conditions of the screening design. Additionally, these experiments were completed using both a THCA concentration of 0.1 mg/mL and 0.2 mg/mL to determine the effect of analyte concentration on the overall efficiency of the derivatization. Efficiency was evaluated based on derivatized product abundance as well as any excess underivatized product present following the reaction. **Figure 4.7** summarizes the optimization studies with averaged THCA-2TMS abundances for each concentration at each temperature.

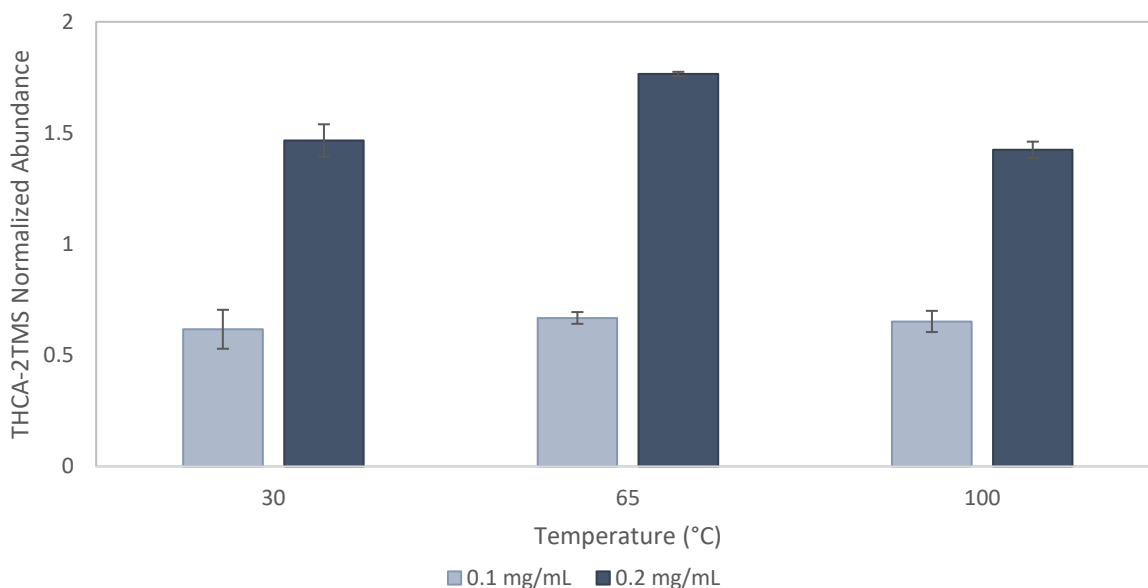


Figure 4.7 THCA-2TMS abundance changes with changes in reaction temperature

Similar to the full factorial screening design results, complete THCA derivatization was observed at each temperature, regardless of concentration. This was indicated by the absence of THC-TMS in the resultant chromatograms from each derivatization. Student's t-tests of the mean THCA-2TMS abundance at each temperature indicated that at 0.1 mg/mL, the average abundances were statistically comparable, and ANOVA analysis confirmed that there was no

statistically significant difference in abundance of THCA-2TMS as a function of temperature ($p = 0.617$). However, at 0.2 mg/mL, the mean abundance of THCA-2TMS at 65 °C was statistically higher than the abundances at 30 °C and 100 °C when compared using a Student's t-test ($p = 0.035$ and $p = 0.004$, respectively) and ANOVA confirmed the significance of temperature for this set of optimization experiments ($p = 0.001$).

The optimum temperature was determined based on the abundance and reproducibility of the THCA-2TMS peak. Derivatization performed at 65 °C provided the highest abundance of THCA-2TMS product most reproducibly (RSD = 0.5%). Accordingly, the optimized method for the derivatization of THCA by BSTFA-1% TMCS using pyridine as a support solvent is summarized by **Table 4.7**.

Table 4.7 Optimum derivatization reaction parameters

Parameter	Optimized Value
Reaction Time	10 min
Reaction Temperature	65 °C
BSTFA : Pyridine	50:50

The optimized method shares some similarity with the published Restek method.⁵ While pyridine was selected as a more suitable support solvent, based on reproducibility and full derivatization of THCA, the reagent:support solvent ratio remains at 50:50 to accommodate the necessity for excess BSTFA-TMCS as well as support solvent volume needed to act as a reaction catalyst. The optimized temperature of 65 °C is comparable to the published temperature of 70 °C, with each providing ample heat to expedite the derivatization without risking THCA decarboxylation. Finally, the reaction time of the optimized method was reduced from that of the

published method. The reduction from 30 min to 10 min reflects the efficiency of the derivatization using pyridine as opposed to ethyl acetate.

4.3.2 Evaluation of Optimized Method Linearity

Using the optimized method as outlined in Section 4.3.1, a concentration study was performed to assess the linearity and upper and lower limits of detection for the derivatization of THCA. These reactions were performed in triplicate using concentrations ranging from 10 $\mu\text{g/mL}$ to 0.5 mg/mL . **Figure 4.8** displays an overlay of the chromatograms for each concentration analyzed. At each concentration, full derivatization of THCA to THCA-2TMS is observed. The inset chromatogram provides a closer look at the THCA-2TMS peak abundances at each concentration.

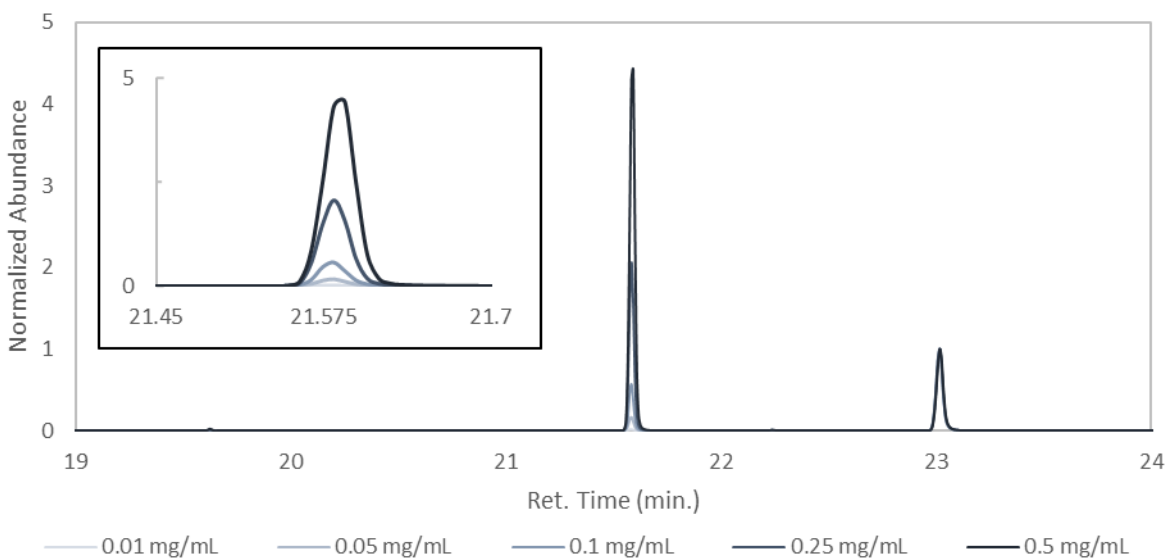


Figure 4.8 Overlay of averaged chromatograms from each concentration study

With the lack of significant peaks at the retention times associated with THC or THC-TMS at the highest concentration (0.5 mg/mL), the optimum derivatization parameters provide

full THCA derivatization that is reliable even at high concentrations. Moreover, the calibration curve demonstrated linearity ($R^2 = 0.995$) over the range of concentrations investigated. **Table 4.8** provides the average normalized THCA-2TMS abundances for each concentration as well as the associated RSD value. A calibration plot is provided in the appendix.

Table 4.8 Summary of concentration study normalized THCA-2TMS abundances and RSDs

THCA Concentration (mg/mL)	THCA-2TMS Norm. Abundance	% RSD
0.01	0.0138	21.1
0.05	0.166	15.1
0.10	0.568	8.4
0.25	2.06	3.2
0.50	4.49	4.3

As summarized by **Table 4.8**, the THCA-2TMS peak is present and discernable from background noise in concentrations as low as 0.01 mg/mL. Derivatizations of low concentrations (0.01 and 0.05 mg/mL) demonstrated high RSD values, which are expected due to the fact that small changes in abundances of that magnitude result in large relative standard deviations. As concentration increases, however, the RSDs for triplicate derivatizations are minimized, with acceptable experimental reproducibility (< 10%) starting at 0.1 mg/mL and higher concentrations. This range of concentrations encompasses most recreational product THCA concentrations, with the highest concentration marijuana solvent extracts available with nearly 99% purity capable of being diluted and characterized.

4.3.3 Analysis of Cannabis Solvent Extracts by GC-MS Using the Optimized Derivatization

Procedure

To further validate the optimized derivatization method, cannabis solvent extract samples were derivatized and analyzed by GC-MS. This provided the ability to observe any matrix effects on the derivatization reaction efficiency given the fact that additional cannabinoids may have been present in the cannabis solvent extract. Further, derivatization and GC-MS analysis of the cannabis solvent extracts served as a method to complete the comprehensive chemical characterization and identification of a subset of extracts for inclusion with the previously discussed optical and spectroscopic characterization.

The first cannabis solvent extract derivatized and analyzed represented the subset of KCSD case samples. A representative chromatogram of derivatized material from case sample KDPS 18-9026 is provided by **Figure 4.9**. Similar to the chromatograms for the derivatized THCA reference material, the peaks of interest in this sample occur between t_R 19 and 24 min, while other peaks present in the chromatogram are due to remaining BSTFA-TMS reagent or siloxanes.

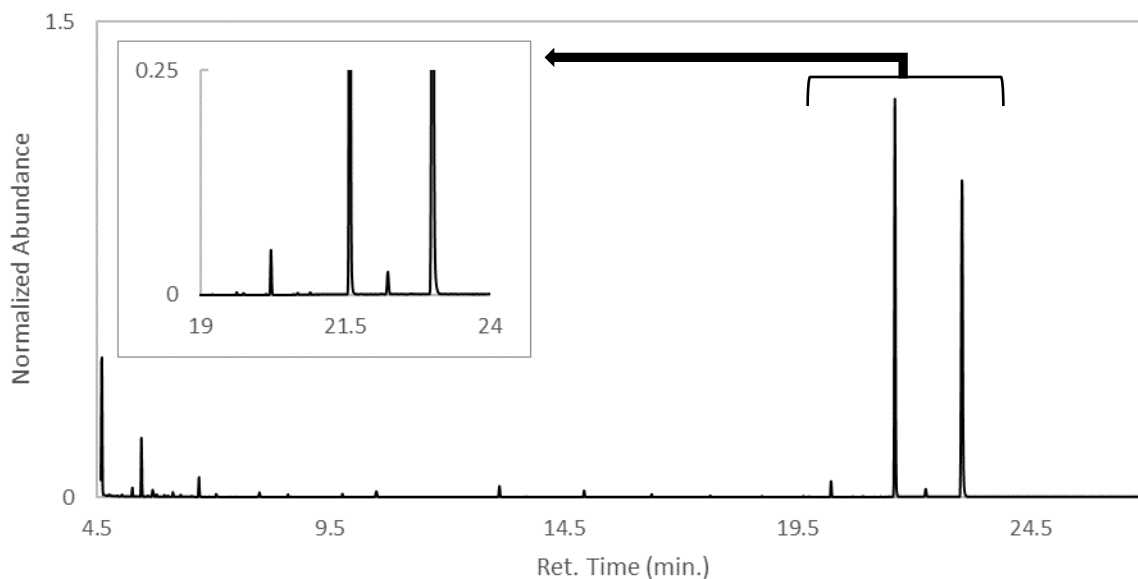


Figure 4.9 Chromatogram of case sample KDPS 18-9026

The inset chromatogram highlights lower abundance peaks eluting at $t_R = 20.2$ min and at $t_R = 22.2$ min. The mass spectrum of the first peak at $t_R = 20.2$ min (**Figure 4.10**) indicates a cannabinol derivative (CBN-TMS). However, the peak at $t_R = 22.2$ min (**Figure 4.11**) was not readily identified due to the low number of ions present in the spectrum. The peaks at $t_R = 21.6$ minutes and $t_R = 23$ minutes are THCA-2TMS (**Figure 4.12**) and progesterone, respectively. A library spectrum for CBN-TMS is provided in the appendix.

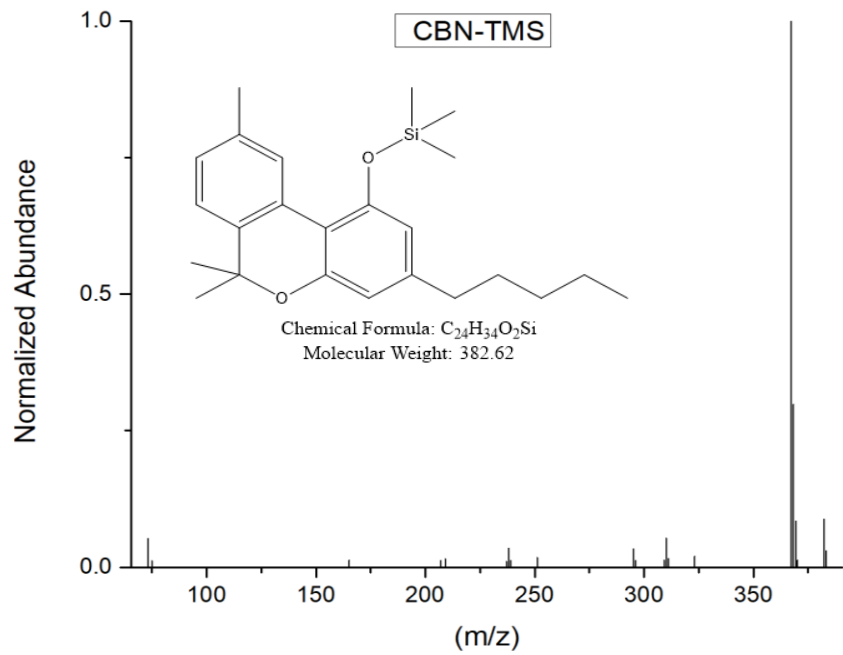


Figure 4.10 Mass spectrum and chemical structure for CBN-TMS

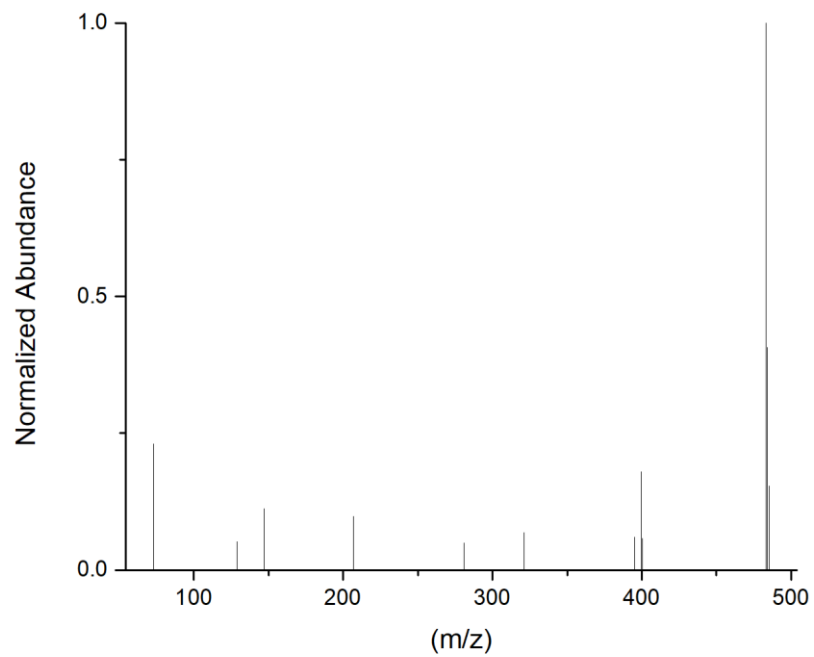


Figure 4.11 Mass spectrum for unidentified peak at 22.2 minutes

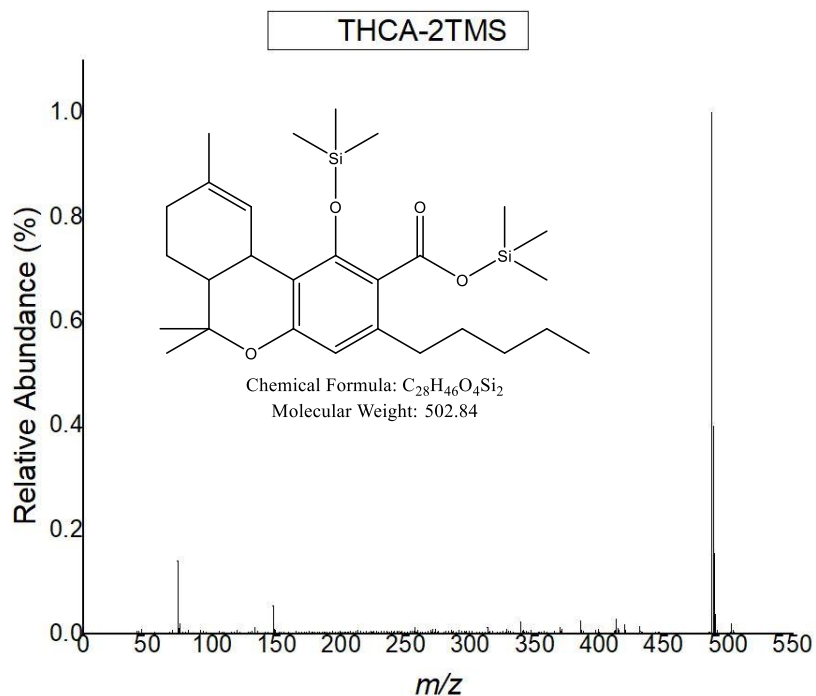


Figure 4.12 Mass spectrum and chemical structure for THCA-2TMS

The mass spectrum for the peak present at $t_R = 22.2$ min is not spectrally similar to THCA-2TMS and has not been observed in previous experiments for this work. Given the lack of total ions in the mass spectrum and no comparable library spectrum, this peak cannot be confidently identified. Some features of the mass spectrum are comparable to the THCA-2TMS mass spectrum, including the base peak at m/z 483.3 and the TMS fragment ion at m/z 73. The expected base peak for THCA-2TMS, however, occurs at m/z 487.4. Noting this, the peak can be assumed to be a derivatized product, but the cannabinoid cannot be distinguished due to the low abundance and low quality of the mass spectrum.

The presence of derivatized CBN indicates that additional cannabinoids other than THCA are present in the KDPS 18-9026 sample. This sample consists of two separate components, crystalline and wax, and was analyzed in bulk, with no separation of the components prior to

GC-MS analysis. The crystalline material has been previously identified through this work as THCA (Chapter 3). Noting that, the presence of CBN in this case sample may indicate the low concentration of CBN and THC present in the wax component of the solvent extract. The small abundance of CBN may be due to the natural decomposition of THC and THCA over time, which would be expected in a sample approximately three years of age (estimated from sample submission). Additionally, the CBN-TMS product could be due to the rapid oxidation of THC to CBN due to the heat of the injection port, followed by immediate derivatization. This process was not studied in the context of this work, and as such the definitive identification of the additional cannabinoid in the wax component is not possible.

The THCA present in KDPS sample was quantified using the calibration curve. Given that this sample was clandestinely manufactured, it was not subjected to quantification prior to sale, nor was it quantified during forensic analysis. Using the regression equation available in the appendix (Figure A4.7), the case sample KDPS 18-90-26 was determined to contain 48.65% THCA by mass.

The WB THCA Crystal sample, representing the Skymint dispensary solvent extracts, was derivatized using the optimum method and analyzed by GC-MS (**Figure 4.13**). Similar to the KDPS 18-9026 sample chromatogram, the main peak attributed to the sample's cannabinoid profile was the THCA-2TMS product peak at $t_R = 21.6$ min. This peak was identified using its mass spectrum (**Figure 4.14**). Additionally, low abundance peaks were present at the retention times associated with the CBN-TMS and THC-TMS peaks but could not be confidently identified by their mass spectra due to the low number of ions present in the spectra and the overlap of background m/z ions in each spectra.

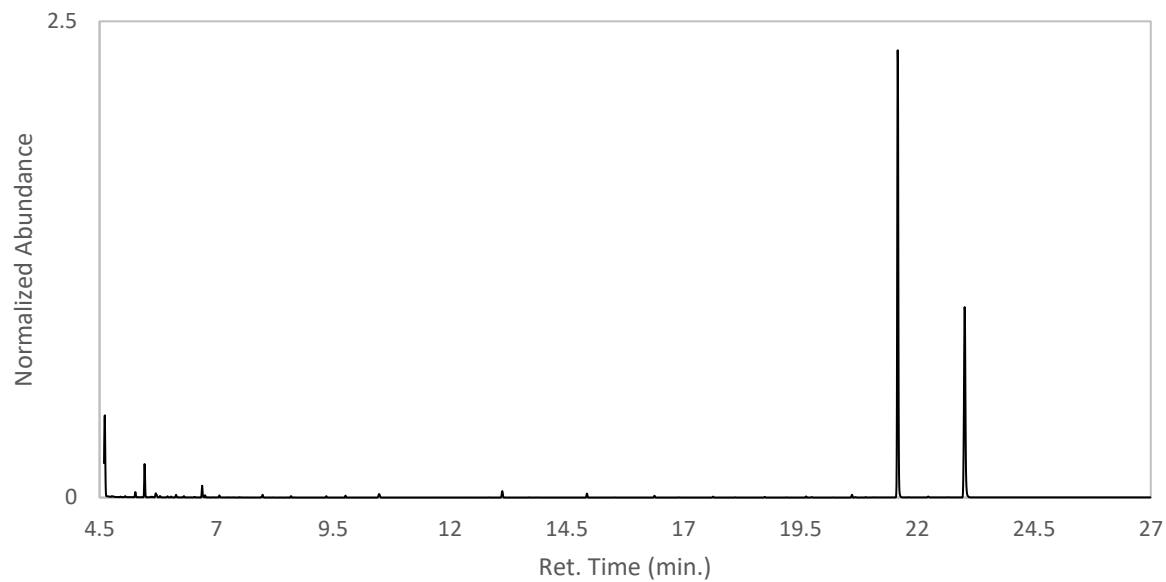


Figure 4.13 Chromatogram of Skymint THCA Crystal sample

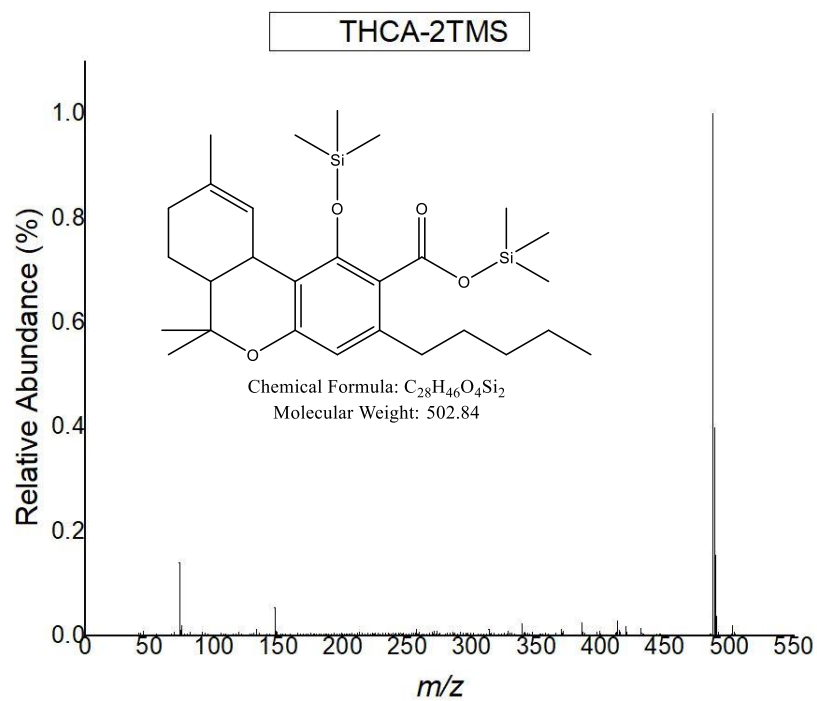


Figure 4.14 Mass spectrum and chemical formula for THCA-2TMS

The lack of additional cannabinoids in this sample is representative of the purity achieved by the regulated production of solvent extractions for recreational use. The overall purity of this sample was independently tested prior to sale and was listed as 76.66% THC ($\pm 10\%$) on the product label (provided in Appendix IV). Comparatively, the concentration of THCA in this sample determined in this work was 83.69%. Given that this determined value falls within the range reported from the independent testing facility, the accuracy of the THCA derivatization method can be displayed, although more samples would need to be quantified to further confirm the functional reliability of the derivatization method for the use of THCA quantification. In order to compare the THCA concentration to the reported THC concentration, the decarboxylation conversion rate (87.7%) was applied. Following this, the total maximum THC potency was found to be 73.4%.

Finally, the Cannabidiol Life CBD crystal sample, representing solvent extracts derived from hemp, was derivatized and analyzed by GC-MS. The CBD Crystal was analyzed with and without derivatization (**Figure 4.15**). The retention time of CBD was 19.9 min, while CBD - 2TMS was $t_R = 18.8$ min. The chromatographic peaks were identified using their mass spectra (**Figure 4.16 and 4.17**), and spectral comparison was employed using the NIST spectra library. The library mass spectra are provided in the appendix. It should be noted that no remaining CBD was present in the derivatized CBD chromatogram, indicating full derivatization of CBD at the given concentration (~ 0.33 mg/mL). As the sample was previously identified as CBD (Chapter 3), as opposed to CBDA, derivatization of the sample prior to GC-MS analysis would not be necessary for differentiation and identification purposes, but does display the robustness of the derivatization method.

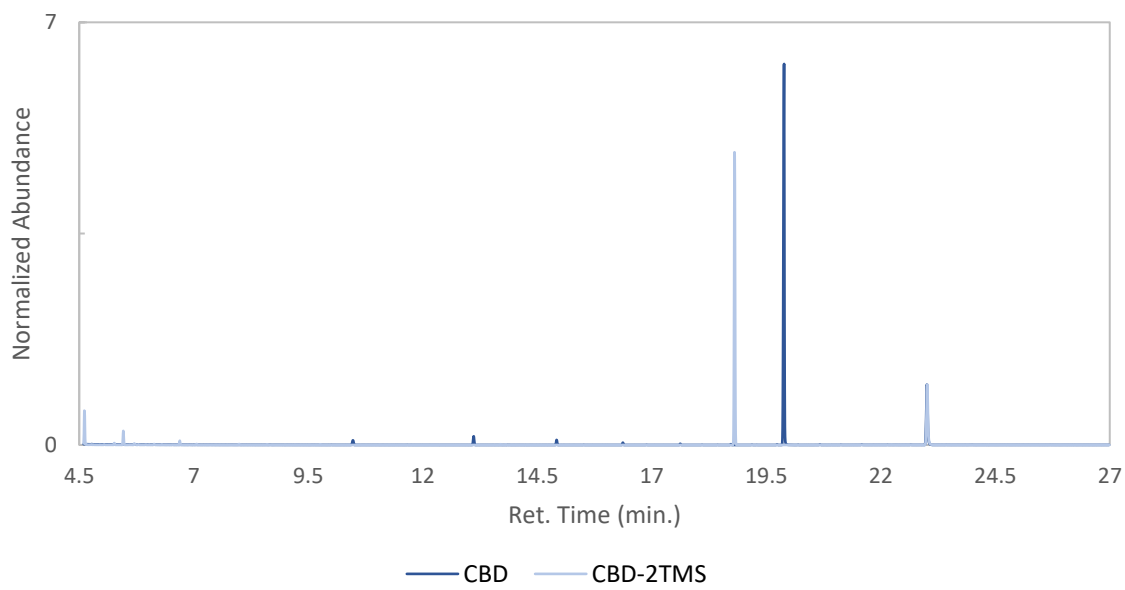


Figure 4.15 Chromatogram of Cannabidiol Life CBD Crystal sample

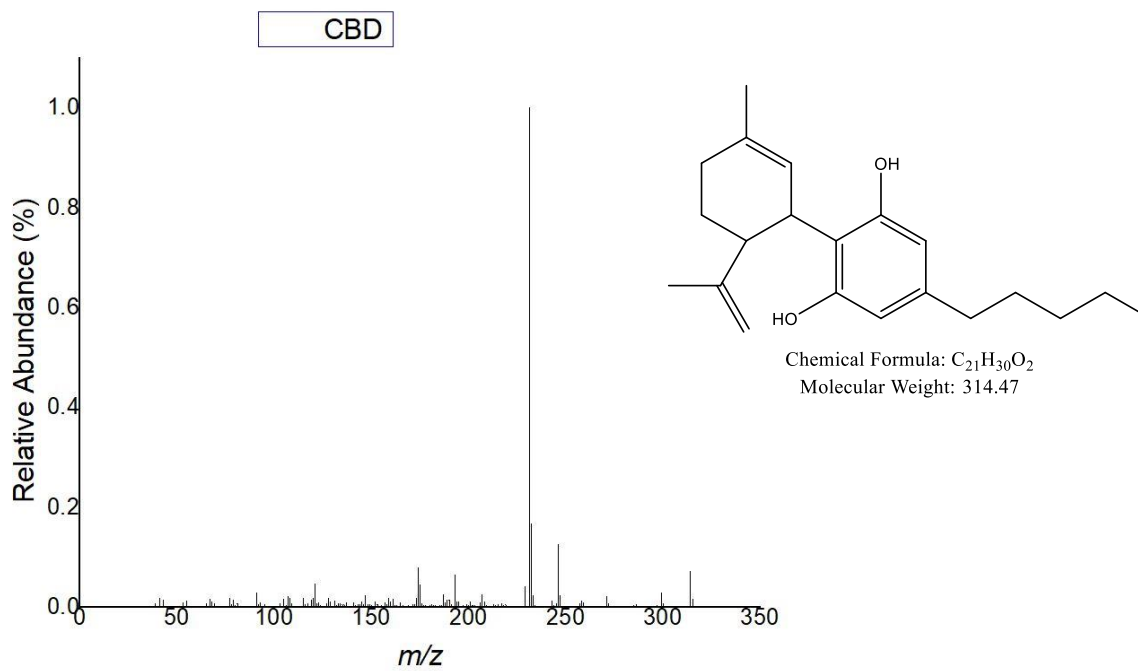


Figure 4.16 Mass spectrum and chemical formula for CBD

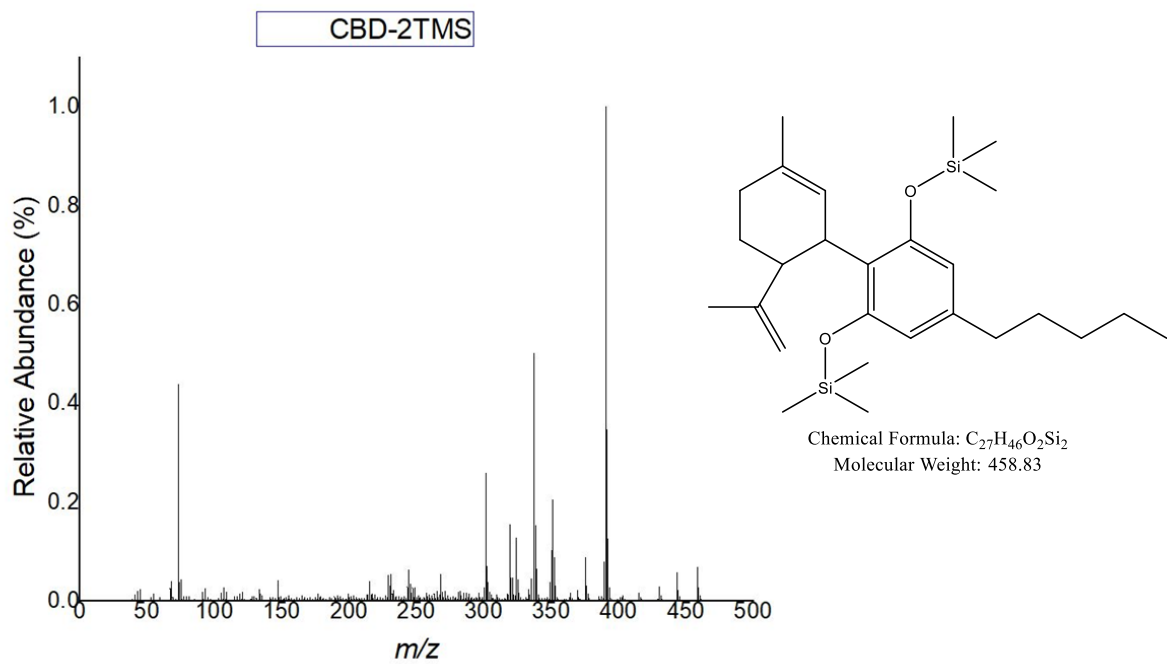


Figure 4.17 Mass spectrum and chemical structure of CBD-2TMS

4.4 CONCLUSIONS

Through this work, a method for the silylation of THCA through a reaction with BSTFA-1%TMCS was optimized using experimental design protocols to increase the overall abundance and reproducibility of the derivatized product, THCA-2TMS. Using an existing, published derivatization method as a starting point, the factors for derivatization evaluated included support solvent, reaction temperature, total time of reaction, and the ratio between the derivatizing reagent (BSTFA-1%TMCS) and the support solvent. Throughout the pre-screening and screening designs, pyridine performed more efficiently and more reproducibly than ethyl acetate as a support solvent. Further, for reactions performed using pyridine only, derivatization temperature was found to be a significant variable for THCA-2TMS abundance. Through ANOVA analysis and optimization experiments a method with optimized time, temperature, and reagent:support solvent ratio was proposed. The optimized method was used to analyze and quantify marijuana-derived solvent extracts, and hemp-derived CBD extracts were additionally analyzed. The optimized method displayed excellent linearity within the concentration range studied, and efficiently derivatized samples with multiple different cannabinoids.

APPENDIX

ANOVA calculations:

Table A4.1 Calculations for the degrees of freedom

Source of Variation	Degrees of Freedom
Factor A	$df_A = a - 1$
Factor B	$df_B = a - 1$
Interaction AB	$df_{AB} = (a - 1)(b - 1)$
Error	$df_E = df_T - (df_A + df_B + df_{AB})$
Total	$df_T = N - 1$

Where:

a and b – levels of Factor A and B

Table A4.2 Calculations for the sum of squares for two-way ANOVA¹⁹

Source of Variation	Sum of Squares
Factor A	$SS_A = nb \sum_i (\bar{y}_i - \bar{y} \dots)^2$
Factor B	$SS_B = na \sum_j (\bar{y}_j - \bar{y} \dots)^2$
Interaction AB	$SS_{AB} = SS_T - SS_E - SS_A - SS_B$
Error	$SS_E = \sum_i \sum_j \sum_k (y_{ijk} - \bar{y}_{ij} \dots)^2$
Total	$SS_T = \sum_i \sum_j \sum_k (y_{ijk} - \bar{y} \dots)^2$

Where:

a and b – number of levels in factor A or B

n – number of trials

$y_{i\dots}$ – mean of the i^{th} factor level of factor A

$y_{j\dots}$ – mean of the j^{th} factor level of factor B

$y \dots$ - overall mean of all observations

y_{ij} – mean of the observations at the i^{th} level of factor A and the j^{th} level of factor B

Table A4.3 Calculations for the mean squares

Source of Variation	Mean Squares
Factor A	$MS_A = \frac{SS_A}{df_A}$
Factor B	$MS_B = \frac{SS_B}{df_B}$
Interaction AB	$MS_{AB} = \frac{SS_{AB}}{df_{AB}}$
Error	$MS_E = \frac{SS_E}{df_E}$

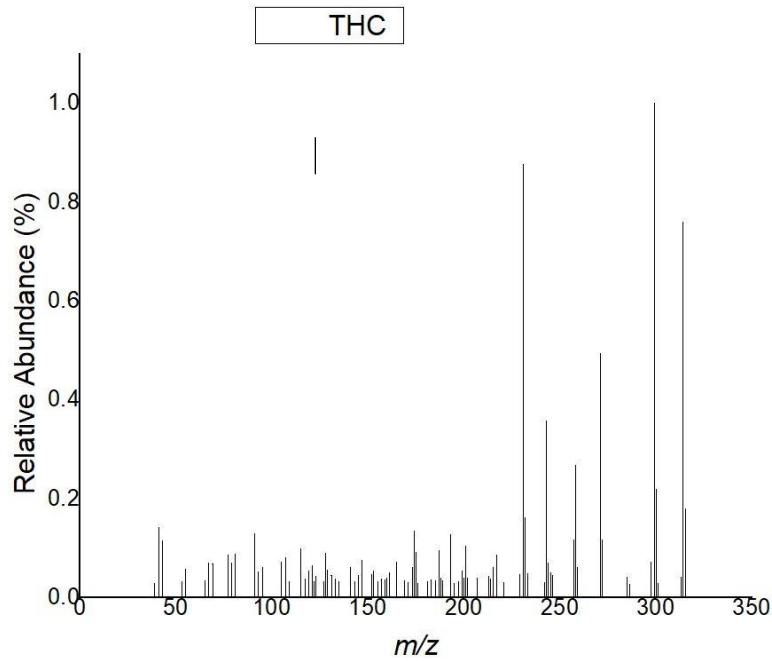


Figure A4.1 THC mass spectrum

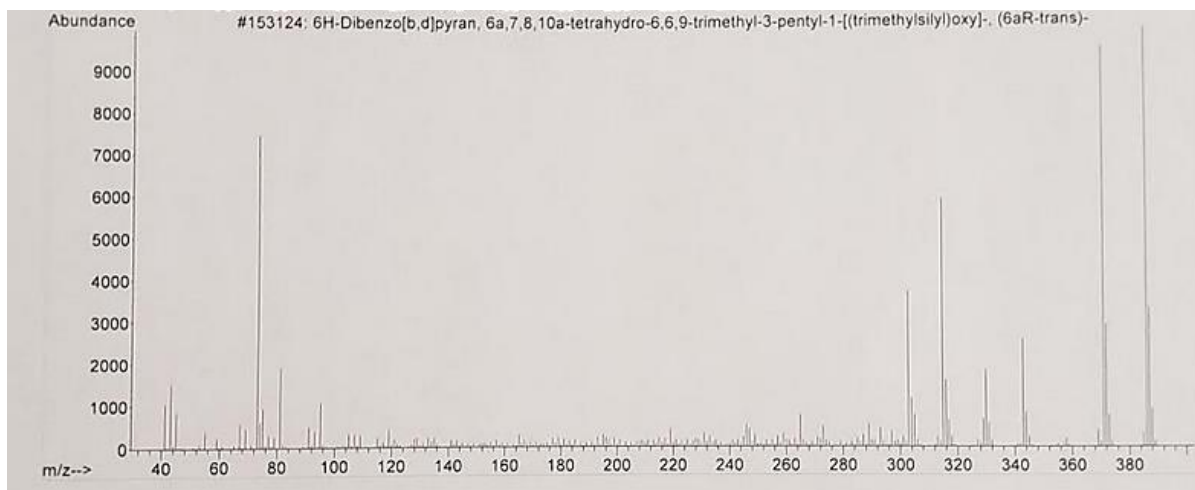


Figure A4.2 NIST library mass spectrum result for THC-TMS

Pre-Screening Experiment Data:

To compare the hold conditions of both solvents, reactions were performed under equivalent conditions, but on separate days given the length of the GC-MS analysis. **Figure A4.3** provides an overlay of averaged chromatograms from the ethyl acetate derivatization with refrigerated and 24 hour hold conditions. Similarly, **Figure A4.4** provides an overlay for the chromatograms from the refrigerated and 24 hour hold experiments using pyridine as a support solvent.

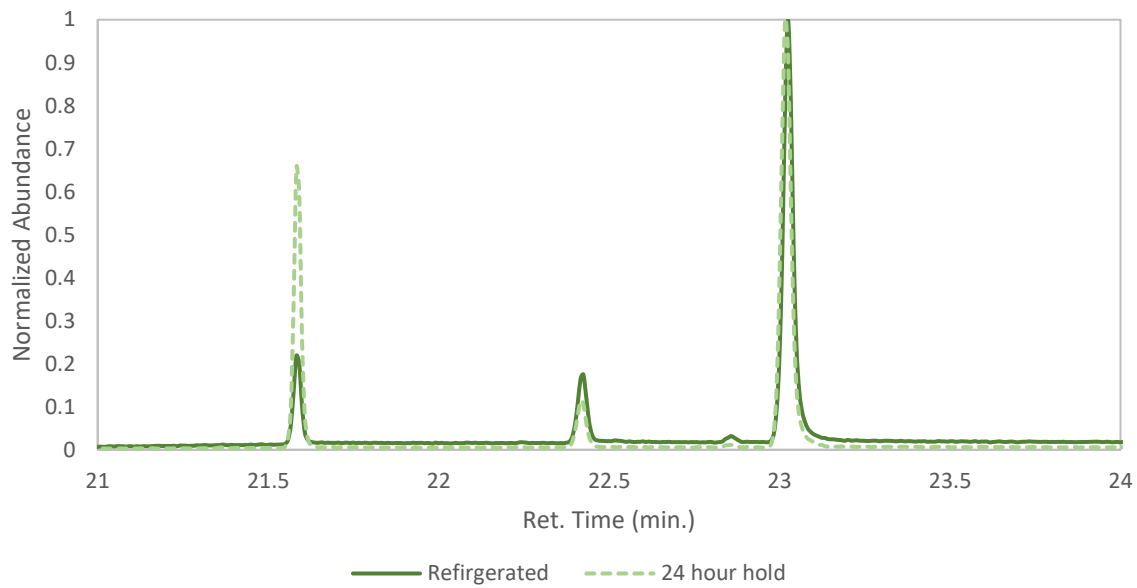


Figure A4.3 Averaged chromatograms comparing refrigerated and 24 hour hold samples of THCA derivatization using ethyl acetate

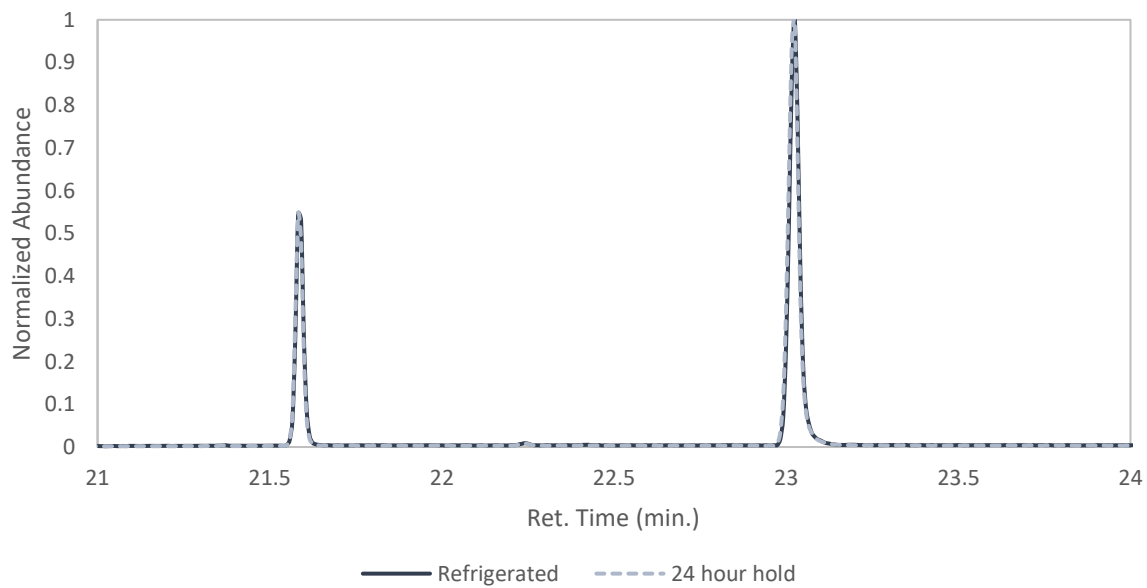


Figure A4.4 Averaged chromatograms comparing refrigerated and 24 hour hold samples of THCA derivatization using pyridine

Table A4.4 Summary of reproducibility for pre-screening hold experiments

	Ethyl Acetate		Pyridine	
	Refrigerated	24 Hr. Hold	Refrigerated	24 Hr. Hold
THCA-2TMS	14.0%	12.5%	7.2%	9.6%
Progesterone	17.5%	11.0%	5.1%	9.1%

Table A4.5 Inter- and intra-vial RSDs for ethyl acetate and pyridine pre-screening experiments

Vial	Ethyl Acetate		Pyridine	
	Refrigerated	24-hour hold	Refrigerated	24-hour hold
1	6.2%	4.5%	1.6%	0.64%
2	7.0%	5.6%	1.0%	6.2%
3	8.4%	3.2%	2.4%	11.1%
Total	14.0%	12.5%	7.2%	9.6%

Table A4.6 Full ANOVA results from derivatizations using pyridine as support solvent

Source	DF	Adj SS	Adj MS	F-Value	P-Value
Model	10	0.243462	0.024346	3.12	0.029
Blocks	3	0.037604	0.012535	1.61	0.236
Linear	3	0.183026	0.061009	7.81	0.003
Time	1	0.019493	0.019493	2.5	0.138
Temperature	1	0.150358	0.150358	19.26	0.001
Ratio	1	0.013175	0.013175	1.69	0.217
2-Way Interactions	3	0.02045	0.006817	0.87	0.48
Time*Temperature	1	0.011664	0.011664	1.49	0.243
Time*Ratio	1	0.000152	0.000152	0.02	0.891
Temperature*Ratio	1	0.008634	0.008634	1.11	0.312
Curvature	1	0.002381	0.002381	0.31	0.59
Error	13	0.101503	0.007808		
Lack-of-Fit	9	0.075507	0.00839	1.29	0.432
Pure Error	4	0.025997	0.006499		
Total	23	0.344965			

Table A4.7 ANOVA results from derivatizations using ethyl acetate as support solvent

Source	DF	Adj SS	Adj MS	F-Value	P-Value
Model	8	0.461012	0.057627	28.47	0.010
Blocks	1	0.084092	0.084092	41.55	0.008
Linear	3	0.367635	0.122545	60.55	0.003
Time	1	0.05373	0.05373	26.55	0.014
Temperature	1	0.306188	0.306188	151.29	0.001
Ratio	1	0.007717	0.007717	3.81	0.146
2-Way Interactions	3	0.004005	0.001335	0.66	0.63
Time*Temperature	1	0	0	0	0.989
Time*Ratio	1	0.003452	0.003452	1.71	0.283
Temperature*Ratio	1	0.000553	0.000553	0.27	0.637
Curvature	1	0.005281	0.005281	2.61	0.205
Error	3	0.006072	0.002024		
Lack-of-Fit	1	0.000566	0.000566	0.21	0.695
Pure Error	2	0.005506	0.002753		
Total	11	0.467084			

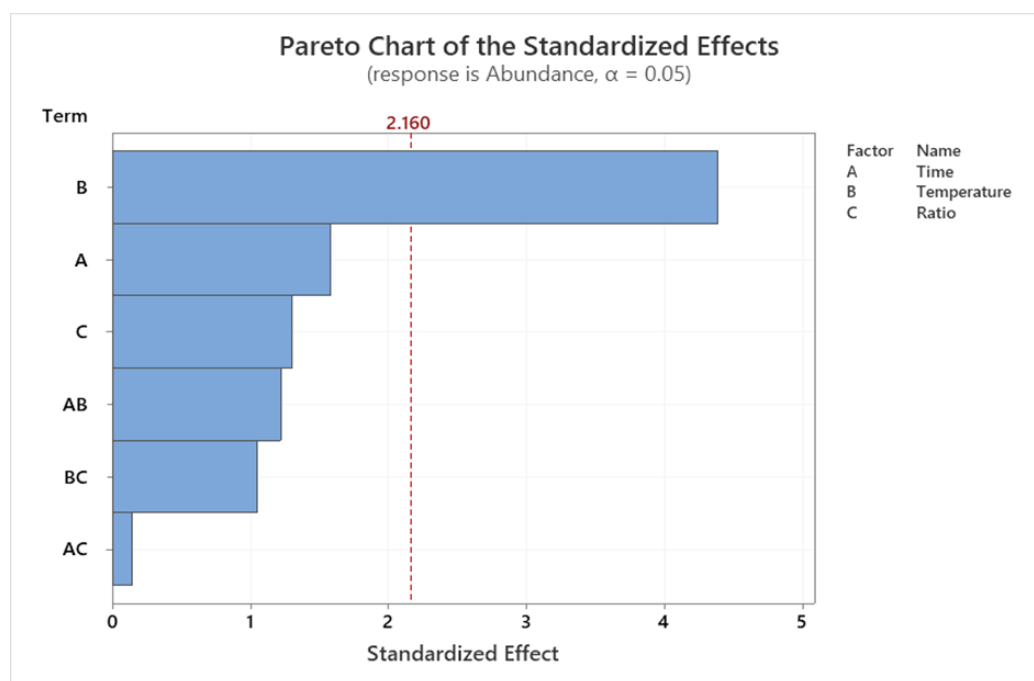


Figure A4.5 Pareto chart for the pyridine full factorial design

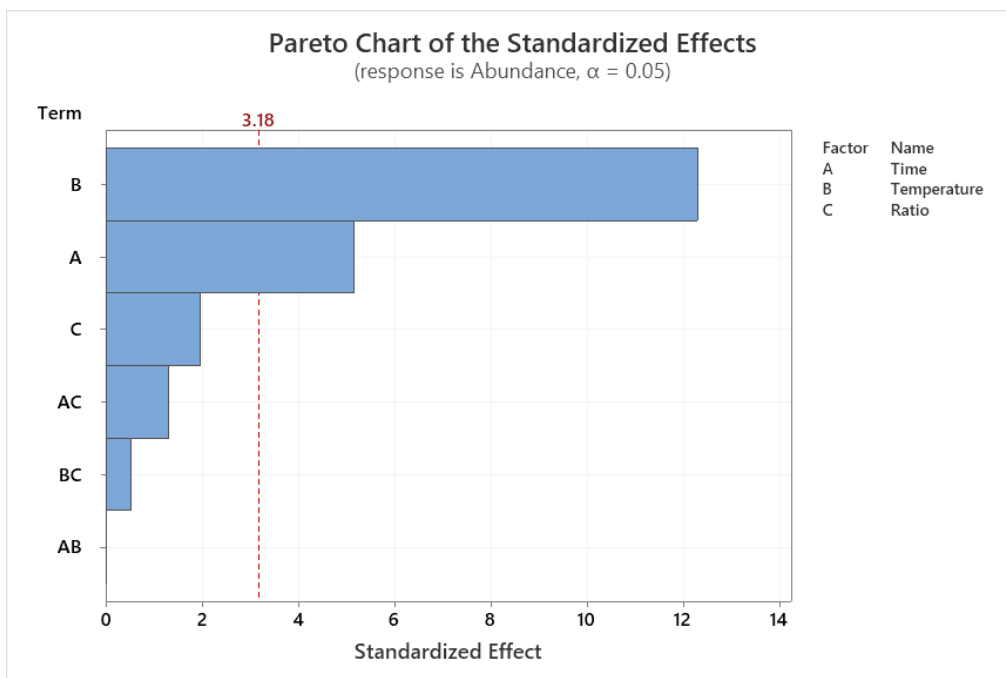


Figure A4.6 Pareto chart for ethyl acetate full factorial design

ANOVA Discussion:

During Minitab full factorial analysis, linear regression models are formed and fit using the provided data. In addition to the ANOVA output, a model fit parameter is provided, including an R^2 value for the model and predicted R^2 for any new data added to the model. In the case of the pyridine full factorial experiments, the R^2 value for the model was low, at 70.58% compared to the ethyl acetate full factorial fit with an R^2 value of 98.70%. Additionally, the predicted R^2 value for the pyridine model could not be estimated, while the predicted R^2 value for the ethyl acetate model was 73.91%. The difference in fits between both models may be due to the fact that for the pyridine experiment, only one factor was found to be significant (temperature), while both temperature and time were significant for the ethyl acetate experiment. Given that only one factor was significant, and the variance between the groups of data for each temperature was not large, the model was not fit as accurately to a regression model. Conversely,

the ethyl acetate experiment provided more significant variation between responses for both the time and temperature factors, allowing for a more well-fit model to be produced. As the ANOVA results were primarily used to determine the significant factors for each experiment, however, the model was found to describe the variation in the pyridine experiment ($p=0.029$) and ethyl acetate experiment ($p=0.010$) regardless of regression model fit as described by the R^2 values.

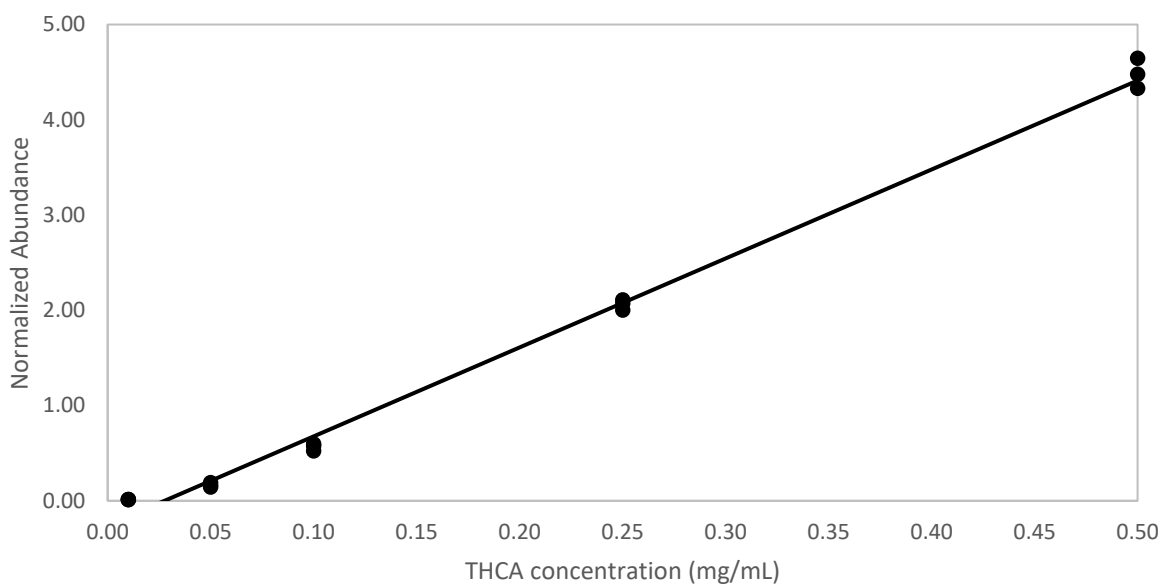


Figure A4.7 Regression plot for THCA concentration study

The regression equation for the fitted line ($R^2 = 0.995$) is:

$$y = 9.34x - 0.257 \quad (\text{Eq. A1})$$

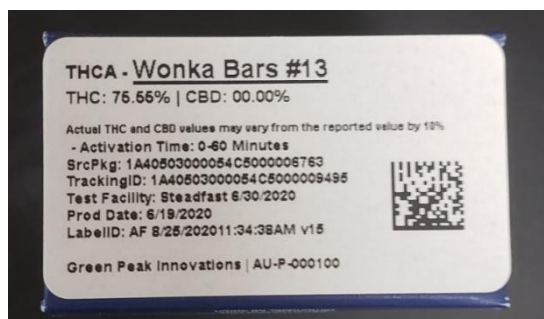


Figure A4.8 Manufacturer information and quantification for Skymint THCA Crystal sample

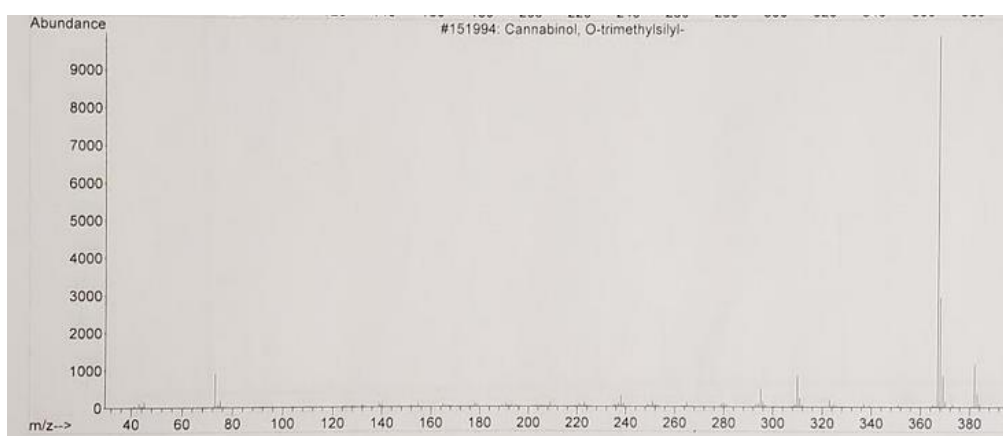


Figure A4.9 NIST library mass spectrum for CBN-TMS

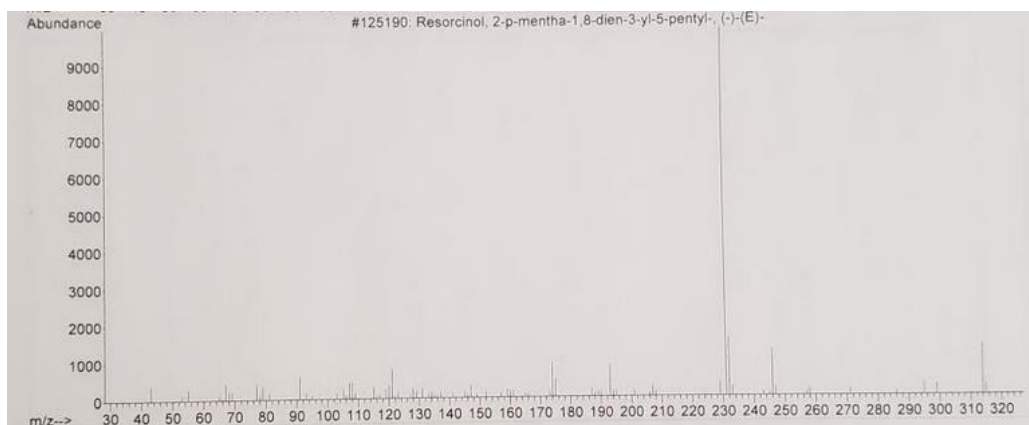


Figure A4.10 NIST library mass spectrum for CBD

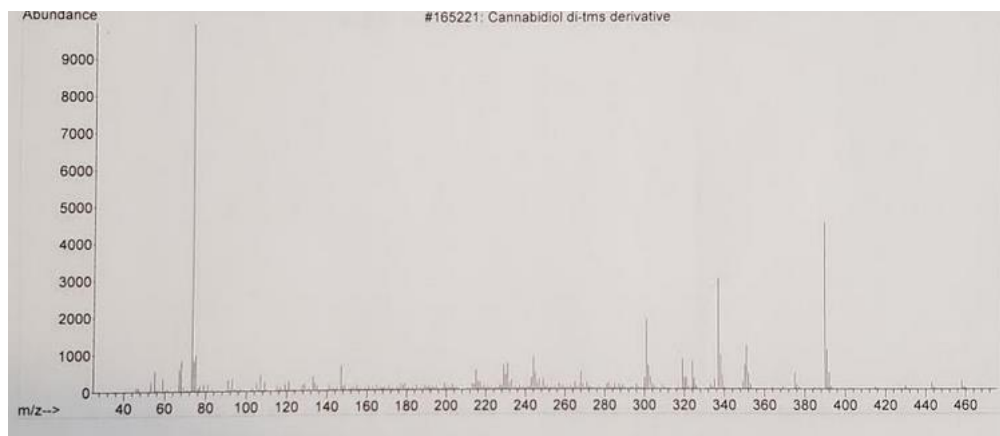


Figure A4.11 NIST library mass spectrum for CBD-2TMS

REFERENCES

REFERENCES

- (1) Agriculture Improvement Act of 2018 (P.L. 115-334), 2018;
<https://www.congress.gov/115/plaws/publ334/PLAW-115publ334.pdf>
- (2) Wang M, Wang YH, Avula B, et al. Decarboxylation Study of Acidic Cannabinoids: A Novel Approach Using Ultra-High-Performance Supercritical Fluid Chromatography/Photodiode Array-Mass Spectrometry. *Cannabis Cannabinoid Res.* 2016 Dec 1;1(1):262-271
- (3) Aizpurua-Olaizola, O., Omar, J., Navarro, P. et al. Identification and quantification of cannabinoids in *Cannabis sativa* L. plants by high performance liquid chromatography-mass spectrometry. *Anal Bioanal Chem* 2014;406, 7549–7560.
- (4) Backer BD, Debrus B, Lebrun P, Theunis L, Dubois N, Decock L, et al. Innovative development and validation of an HPLC/DAD method for the qualitative and quantitative determination of major cannabinoids in cannabis plant material. *Journal of Chromatography B* 2009;877(32):4115–24.
- (5) Politi M, Peschel W, Wilson N, Zloh M, Prieto JM, Heinrich M. Direct NMR analysis of cannabis water extracts and tinctures and semi-quantitative data on delta9-THC and delta9-THC-acid. *Phytochemistry.* 2008 Jan;69(2):562–70.
- (6) Rigdon, A. Accurate Quantification of Cannabinoid Acids and Neutrals by GC. *Restek.com*, 2015.
- (7) Cardenia V, Toschi TG, Scappini S, Rubino RC, Rodriguez-Estrada MT. Development and validation of a Fast gas chromatography/mass spectrometry method for the determination of cannabinoids in *Cannabis sativa* L. *Journal of Food and Drug Analysis* 2018;26(4):1283–92.
- (8) Milman G, Barnes AJ, Lowe RH, Huestis MA. Simultaneous quantification of cannabinoids and metabolites in oral fluid by two-dimensional gas chromatography mass spectrometry. *Journal of Chromatography A* 2010;1217(9):1513–21.
- (9) Kranenburg RF, Verduin J, Stuyver LI, Ridder RD, Beek AV, Colmsee E, et al. Benefits of derivatization in GC–MS-based identification of new psychoactive substances. *Forensic Chemistry* 2020;20:100273.
- (10) S.C. Moldoveanu, V. David, *Derivatization methods in GC and GC/MS Gas Chromatography - Derivatization, Sample Preparation, Application*, IntechOpen 2019;
- (11) Poole CF. Alkylsilyl derivatives for gas chromatography. *Journal of Chromatography A* 2013;1296:2–14.

- (12) Prata VDM, Emídio ES, Dorea HS. New catalytic ultrasound method for derivatization of 11-nor- Δ^9 -tetrahydrocannabinol-9-carboxylic acid in urine, with analysis by GC-MS/MS. *Analytical and Bioanalytical Chemistry* 2012;403(2):625–32.
- (13) Jurado-Sánchez B, Ballesteros E, Gallego M. Determination of carboxylic acids in water by gas chromatography–mass spectrometry after continuous extraction and derivatisation. *Talanta* 2012;93:224–32.
- (14) Sigma-Aldrich Co. BSTFA Product Specification. 1997; <https://www.sigmaaldrich.com/Graphics/Supelco/objects/4800/4746.pdf>
- (15) Sigma-Aldrich Co. Derivatization Reagents for Selective Response and Detection in Complex Matrices. 2011; <https://www.sigmaaldrich.com/content/dam/sigmaaldrich/migrationresource4/Derivatization%20Rgts%20brochure.pdf>
- (16) Araujo PW, Brereton RG. Experimental Design I. Screening. *Trends Anal Chem* 1996; 15:26-31.
- (17) Stufken J, Dean A, Morris M, Bingham D, Dean. *Handbook of Design and Analysis of Experiments*. CRC Press, 2015;
- (18) Brereton RG. *Chemometrics: data driven extraction for science*. Chichester: Wiley Blackwell, 2018;
- (19) Watson, J. T.; Sparkman, O. D. *Introduction to Mass Spectrometry: Instrumentation, Applications and Strategies for Data Interpretation*; Wiley: Chichester, 2011;

5. CONCLUSIONS AND FUTURE WORK

5.1 CONCLUSIONS

Throughout this work, sets of cannabis solvent extracts, derived from either marijuana or hemp, were comprehensively characterized. The characterization of both the crystalline and wax components of the cannabis solvent extracts included optical characterization by polarized light microscopy (PLM), spectroscopic characterization by infra-red (IR) spectroscopy and single crystal X-ray diffraction (XRD), and finally spectrometric identification by gas chromatography-mass spectrometry (GC-MS). These characterizations were performed in order to further research the components of cannabis solvent extracts using a variety of instrumentation available to forensic scientists, as well as provide methods by which solvent extracts derived from marijuana or hemp could be differentiated.

Analysis of the crystalline component of each cannabis solvent extract by polarized light microscopy allowed for subsets of extracts to be compared and grouped based on crystal optics. As demonstrated, the KCSD case samples each contained analogous crystals regardless of sample age or extract texture. Similarly, the crystalline material from the Skymint dispensary samples were optically similar within the Skymint subset and were comparable to the KCSD case sample crystals. As both subsets were derived from marijuana (either clandestinely or through regulated manufacturing), this substantiated that a preferred crystalline material forms in marijuana solvent extracts regardless of manufacturing technique or product texture. Additionally, the samples derived from hemp from the Cannabidiol Life dispensary were optically characterized and were found to contain analogous crystals within their subset but did not share optical characteristics with the marijuana extract subset. The difference in crystal optics between the marijuana and hemp-derived solvent extracts provides the opportunity to distinguish

the two optically based on their crystal presence, allowing for a rapid screening for macroscopically similar samples.

Spectroscopic analysis of the sample subsets provided chemical characterization not offered by PLM analysis. Micro-attenuated total reflectance-Fourier transform infrared spectroscopy (micro-ATR-FTIR) analysis was used to chemically characterize both the crystalline and wax components (when present) of each sample and provided presumptive identification for each component. The marijuana solvent extract subset, comprised of KCSD case samples and Skymint dispensary samples, had comparable IR spectra for both the crystalline and wax components of each sample. Each of the crystalline sample components shared spectral characteristics analogous to tetrahydrocannabinolic acid (THCA), while the wax component shared spectral characteristics with both THCA and tetrahydrocannabinol (THC). Conversely, the Cannabidiol Life dispensary sample crystalline and wax components were spectrally similar to cannabidiol (CBD). Further analysis of two crystalline samples from the marijuana solvent extract subset and one crystalline sample from the hemp extract subset was performed using single crystal XRD, which confirmed the presumptive identification for each sample *via* micro-ATR-FTIR. The spectroscopic characterization and identification of each subset further strengthened the hypothesis that cannabis solvent extracts derived from marijuana and hemp would produce products differentiable by forensic techniques. Not only were the samples grouped successfully based solely on optical characteristics, but their optical similarities (within subsets) and differences (between subsets) can be chemically explained based on the prominent cannabinoid present in the final extracted product.

Given the wide-spread use of GC-MS for seized drug analysis in forensic crime labs, it was necessary to perform spectrometric analysis of samples from each subset in order to provide a comprehensive characterization of cannabis solvent extracts. Due to the identification of the marijuana-derived subset's crystalline material as THCA, derivatization of the sample prior to GC-MS analysis was necessary to avoid decarboxylation to THC. As such, a previously published silylation procedure was optimized for the derivation of THCA.¹

A combination of pre-screening experiments, replicated full factorial screening design experiments, and optimization experiments were performed to establish the significant parameters of derivatizations using N,O-Bis(trimethylsilyl)trifluoroacetamide (BSTFA) - 1% trimethylchlorosilane (TMCS) and either pyridine or ethyl acetate as support solvents. The three factors studied during the full factorial screening design included temperature of reaction, time of reaction, and the ratio between BSTFA and the support solvent. From this design, temperature was found to be the only significant parameter for derivatization using pyridine as the support solvent, while both temperature and time were significant for ethyl acetate-supported derivatizations.

The preferred solvent, as determined by both the pre-screening and full factorial screening design experiments, was pyridine, rather than ethyl acetate due to increased reproducibility and overall abundance of derivatized product THCA – (2) trimethylsilyl (THCA-2TMS). The optimization of the pyridine-supported derivatization was performed by adjusting the temperature of reaction while maintaining the time and solvent ratio. The optimum parameters for the derivatization of THCA were determined to be a 10-minute reaction at 65 °C using a ratio of 50:50. This optimized reaction was validated using a concentration study that

showed excellent linearity and full derivatization of THCA to THCA-2TMS within the concentration range of 10 µg/mL to 0.5 mg/mL ($R^2 = 0.995$).

Following optimization, a selection of cannabis extract samples – two crystalline samples from the marijuana solvent extract subset and one crystalline sample from the hemp extract subset – were derivatized and analyzed by GC-MS. The samples from the marijuana extract subset contained analogous prominent peaks, with THCA-2TMS making up most of the chemical composition of the sample. Additionally, the hemp-derived extract sample was analyzed with and without derivatization, providing spectrometric identification of the main component as CBD and CBD-2TMS respectively. This confirmed the robustness and versatility of the optimized derivatization parameters for the derivatization of additional cannabinoids other than THCA.

This work showcases the possible methods of screening and analysis for cannabis solvent extracts derived from either marijuana or hemp. Given the optical and chemical differences between marijuana and hemp-derived solvent extracts, the research presented provides the opportunity to apply optical and spectroscopic methods in forensic laboratories for the purpose of screening macroscopically similar samples prior to confirmatory analysis. The readily observed optical properties between crystalline components from the marijuana and hemp subsets offers rapid screening, with more chemically specific information than what is generally determined by a Duquenois-Levine color test, while additionally reducing sample destruction. Further, the optimized derivatization protocol can be readily implemented in forensic and independent laboratories where complete cannabinoid potency determination is necessary by GC-MS analysis.

5.2 FUTURE WORK

Portions of this work can be expanded to provide more thorough characterization of cannabis solvent extracts. For example, the marijuana-derived extracts used in this work were hydrocarbon solvent extracts, most commonly extracted using butane, while the hemp-derived extracts were extracted using supercritical CO₂. Moving forward, research in this field could compare the crystal habits between marijuana-derived extracts using extraction solvents other than hydrocarbons. It is expected that the crystalline components would exhibit similar optical and chemical characteristics, given the cannabinoid profile for such samples.

Additionally, during this work it was concluded by single-crystal XRD that the crystalline THCA from a clandestine case sample was a racemic crystal, while the crystalline THCA from the Skymint dispensary sample was chiral. Given the illegal nature of clandestine solvent extract manufacturing using hydrocarbons such as butane, a case study comparing the single-crystal XRD results of clandestine-manufactured solvent extracts versus regulated dispensary solvent extracts may provide the opportunity to differentiate the two based on sample chirality. This may allow for the effective differentiation of legally (regulated) and illegally produced (clandestine) marijuana solvent extracts.

Finally, further research can be performed using the optimized derivatization method for the analysis of multi-cannabinoid samples and samples of different matrices. In this work, a standard THCA certified reference material was used for all of the optimization and linearity validation experiments. As such, this method was optimized for the derivatization of THCA only, and not THCA in combination with other common cannabinoids (including THC). It would be beneficial to further optimize this procedure for each common cannabinoid individually, and in a mixture, in order to provide the most confident and comprehensive derivatization protocol.

REFERENCES

REFERENCES

- (1) Rigdon, A. Accurate Quantification of Cannabinoid Acids and Neutrals by GC. Restek.com, 2015.